

# Direct Simulation Monte Carlo: Surface Chemical Reaction

Vom Fachbereich Produktionstechnik  
der  
University of Bremen

zur Erlangung des Grades  
Doctor-Ingenieur  
genehmigte

Dissertation  
von  
Sangita Swapnasrita, M. Sc.

Gutachter: Prof. Dr.-Ing. habil. Lutz Mädler  
Prof. Dr.-Ing. Lucio Colombi Ciacchi

Tag der mündlichen Prüfung: 30 April 2021



# Abstract

Interest in nanocatalysts is increasing, reflected by the dramatic increase in the number of publications on the synthesis, characterisation and applications of such catalysts. One salient feature concerning the catalysts is the heterogeneous surface reactions. Paradigm-changing research in heterogeneous catalysis was the development of surface science techniques by Gerhard Ertl, eventually winning him the Nobel Prize in 2007.

Recent development in computer performance, multiscale simulation approaches are widely used for continuous and dynamic surface modeling in complex porous catalysts. In the microscale, these models describe the adsorption, desorption and reaction steps and in the macroscale, collision and mass transport steps. The development of heterogeneous catalysis models is a complex, multiscale process in which many mechanisms occur simultaneously. Direct Simulation Monte Carlo (DSMC) method is one such phenomenological modeling tools developed by G. A. Bird to study gas flows in rarefied condition such as those found in outer space or during atmospheric re-entry. This thesis presents a surface reaction model using DSMC solver in OpenFOAM to predict mass transport as well as chemical kinetics in reactor systems.

First, the surface reaction model proposed by Pesch et al. is modified using a variable parcel algorithm to make it computationally faster. With the benefit of faster calculations, the model is used to provide insights into the dynamic CO oxidation reaction occurring on Pd nanoparticles in microfluidic channels. The experimental setup is designed in Chalmers with a microfluidic chip with channels embedded with Pd nanoparticles, deposited by an electron beam and further annealed. The chip is equipped with mass flow controllers and mass spectrophotometer to procure inlet and outlet gas composition. There is huge agreement in literature, that CO oxidation on Pd proceeds via Langmuir-Hinshelwood mechanism to create CO<sub>2</sub>, which is then immediately desorbed into the gas phase. CO and O adsorption on Pd catalyst, is however, a more complex process where CO usually dominates and inhibits O adsorption leading to catalyst poisoning. As expected, such a system has multiple input variables such as reaction and desorption activation energies, surface description, adsorption coefficients, gas composition, pressure and temperature. For simplification, the chip's temperature is maintained with a feedback control Pt heater. Isothermal conditions are maintained in the simulation in accordance and any heat

of reaction is neglected. Surface characteristics such as defects, edges, vacancies etc lead to enhanced reaction rates in the catalysts. Again, to reduce complexities, the surface is assumed to be free of any defects and a single crystal structure is assumed. With this particular system in mind along with the assumptions, the model is subjected to an extensive sensitivity analysis. One input parameter is varied within a decided range to study the effect on the output variable. The parameters are combined in an optimal way to fit the predicted CO<sub>2</sub> output concentration with the experiments. The final set of parameters are well within values provided in literature for similar setups. The final addition of a single parameter to the simulation greatly enhances the agreement between computations and experiments.

Aside from the mass transport prediction, DSMC is well established as a model to study microscopic local reaction kinetics. The model is able to provide both temporal and spatial resolution to the progression of poisoning in the channel. It is possible to show that in this specific system, higher temperatures lead to high reaction and desorption rates for CO, which controls the amount of poisoning and the particles remain active for longer. Evidence is also shown that the inlet gas composition is critical to determine the overall conversion. Low CO concentration in the gas leads to low CO presence on the surface (diffusion-limited) and the conversion stays low. High CO concentration leads to an abundance of CO on the surface which then inhibits O adsorption and the catalyst is poisoned.

A model is presented in this thesis that would be helpful to material scientists who want to look into gas interactions with surface and provide localised information of reaction and surface coverages.

## Zusammenfassung

Das Interesse an Nanokatalysatoren nimmt zu, was sich in der dramatischen Zunahme der Veröffentlichungen zur Synthese, Charakterisierung und Anwendung solcher Katalysatoren widerspiegelt. Ein hervorstechendes Merkmal von heterogenen Katalysatoren sind Oberflächenreaktionen. Eine paradigmwechselnde Entwicklung in der heterogenen Katalyse war die Erforschung von molekularen Prozessen auf der Katalysatoroberfläche mit Hilfe oberflächenwissenschaftlicher Techniken durch Gerhard Ertl, eine Forschung die ihm schließlich 2007 den Nobelpreis einbrachte.

Jüngste Entwicklungen der Computerleistung erlauben multiskalige Simulationsansätze. Diese erlauben kontinuierliche und dynamische Oberflächenmodellierung in

komplexen porösen Katalysatoren. Im Mikromaßstab beschreiben diese Modelle die molekularen Adsorptions-, Desorptions- und Reaktionsschritte, im Makromaßstab hingegen beschreiben sie den Massentransport.

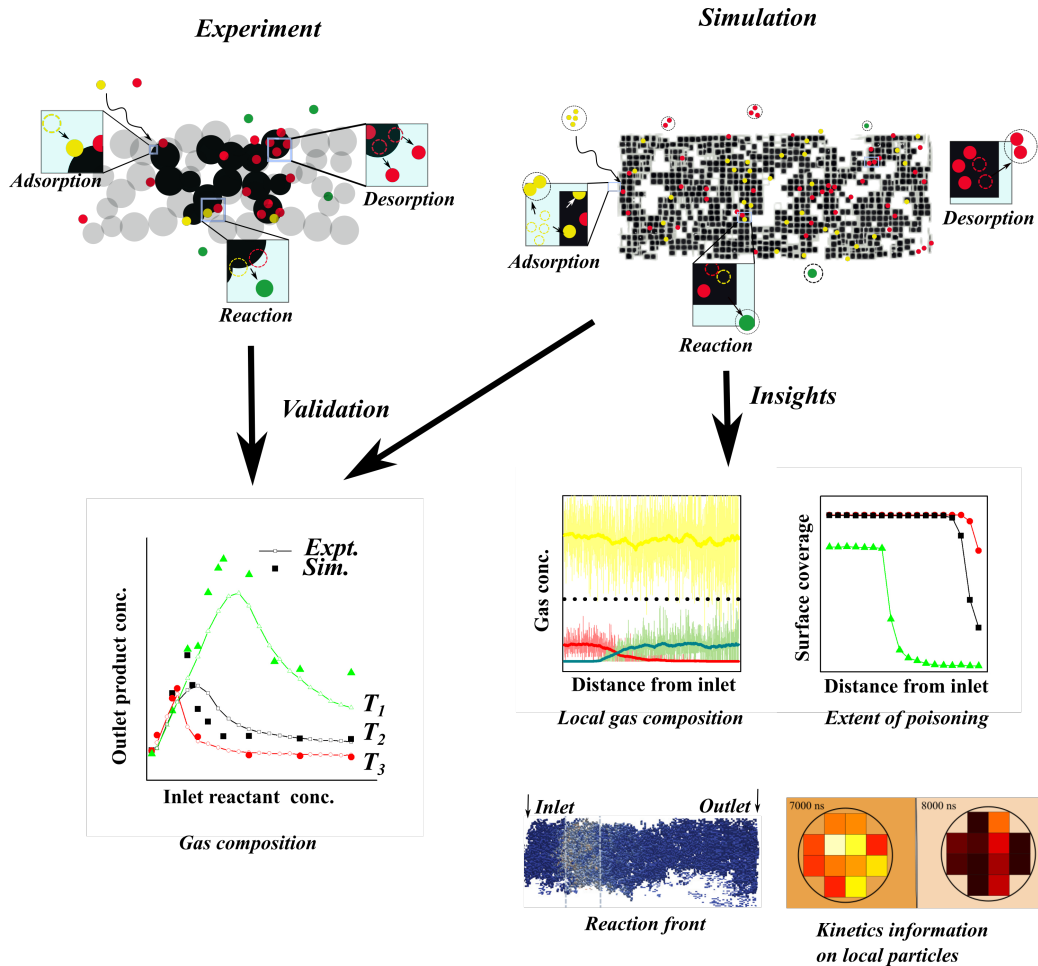
Modelle zur Beschreibung heterogenkatalysierter Reaktionen sind daher meist komplex und mehrskalig, da viele Mechanismen parallel auftreten. Direct Simulation Monte Carlo (DSMC) ist ein solches phänomenologisches Modellierungswerkzeug. Es wurde von G. A. Bird entwickelt, um verdünnte Gasströmungen, wie zum Beispiel im Weltraum oder während des atmosphärischen Wiedereintritts zu finden sind, zu untersuchen. In dieser Arbeit wird ein Oberflächenreaktionsmodell unter Verwendung eines DSMC-Lösers in OpenFOAM vorgestellt, um den Massentransport mit chemischer Kinetik zu verknüpfen und damit Reaktionsprozesse in Reaktorsystemen vorherzusagen.

Zunächst wurde in ein existierendes Modell von Pesch et al. ein „Variable Parcel“ Algorithmus implementiert, um die Berechnung zu beschleunigen. Mit dem Vorteil schnellerer Berechnungen wird das Modell verwendet, um Einblicke in die dynamische CO-Oxidationsreaktion zu erhalten, die an Pd-Nanopartikeln in Mikrofluidikkanälen auftritt. Der Versuchsaufbau und die daran angeschlossenen Experimente wurden in Kooperation mit der Technischen Hochschule Chalmers realisiert. In einem Mikrofluidikchip befinden sich mehrere parallele Kanäle in die Palladium-Nanopartikel eingebettet sind. Die Nanopartikel wurden durch einen Elektronenstrahl abgeschieden und weiter getempert. Der Chip ist an Massendurchflussregler und ein Massenspektrophotometer angeschlossen, um die Zusammensetzung des Einlass- und Auslassgases zu ermitteln. In der Literatur besteht eine große Übereinstimmung darüber, dass die CO-Oxidation an Pd über den Langmuir-Hinshelwood Mechanismus erfolgt, um  $\text{CO}_2$  zu erzeugen, das dann sofort in die Gasphase desorbiert wird. Die CO- und O-Adsorption an den Palladium-Nanopartikeln ist jedoch ein komplexerer Prozess, bei dem CO normalerweise über die O-Adsorption dominiert und diese hemmt, was zu einer Katalysatorvergiftung führt. Ein solches System hat mehrere Eingangsvariablen wie Reaktions- und Desorptionsaktivierungsenergien, Adsorptionsstellendichte, Adsorptionskoeffizienten, Gaszusammensetzung, Druck und Temperatur. Zur Vereinfachung wird die Temperatur des Chips mit einer geregelten Heizung aufrechterhalten. Die isothermen Bedingungen werden in der Simulation entsprechend aufrechterhalten und jede Reaktionswärme wird vernachlässigt. Oberflächeneigenschaften wie Defekte, Kanten, Leerstellen usw. führen zu erhöhten Reaktionsgeschwindigkeiten in den Katalysatoren. Um die Komplexität zu verringern, wird angenommen, dass die Oberfläche frei von Defekten ist und eine Einkristallstruktur vorherrscht. Unter Das Simulationsmodell dieses Systems wird unter Berücksichtigung der Annahme wird das Modell einer umfassenden Sensitivitätsanalyse unterzogen. Ein Eingabeparameter wird innerhalb eines festgelegten Bereichs vari-

iert, um die Auswirkung auf die Ausgabeveriable zu untersuchen. Die Parameter werden optimal kombiniert, um die vorhergesagte  $\text{CO}_2$ -Ausgangskonzentration an die Experimente anzupassen. Der endgültige Parametersatz liegt innerhalb der in der Literatur angegebenen Werte für ähnliche Einstellungen. Die endgültige Hinzufügung eines einzelnen Parameters zur Simulation verbessert die Übereinstimmung zwischen Berechnungen und Experimenten erheblich.

Abgesehen von der Vorhersage des Massentransports ist DSMC als Modell zur Untersuchung der mikroskopischen lokalen Reaktionskinetik gut etabliert. Das Modell ist in der Lage zeitlich wie auch räumlich die CO-Vergiftung im Kanal aufzulösen und vorherzusagen. In diesem spezifischen System führen höhere Temperaturen zu hohen Reaktions- und Desorptionsraten für CO, wodurch das Ausmaß der Vergiftung gesteuert wird und die Partikel länger aktiv bleiben. Es wird auch gezeigt, dass die Zusammensetzung des Einlassgases entscheidend ist, um die Gesamtumwandlung zu bestimmen. Eine niedrige CO-Konzentration im Gas führt zu einer geringen CO-Präsenz auf der Oberfläche (diffusionslimitiert) und die Umwandlung bleibt niedrig. Eine hohe CO-Konzentration führt zu einem Überschuss von CO auf der Oberfläche, die dann die O-Adsorption hemmt und den Katalysator vergiftet.

In dieser Arbeit wird ein Modell vorgestellt, das es sowohl Materialwissenschaftlern wie auch Verfahrenstechnikern ermöglicht, die Wechselwirkung des Gases mit der Oberfläche zu untersuchen und lokalisierte Informationen zu Reaktionen und Oberflächenbedeckungen zu erhalten.



*Insights into an actual chemical nano reactor using Direct Simulation Monte Carlo (DSMC) simulation. The experimental setup consists of a gas reaction on a mesoporous catalyst surface. First, the DSMC solver is validated with the experimental gas concentrations at the outlet. Additionally, DSMC can also predict further insights into the reactor, which makes it a very helpful tool in designing such reactors.*



# Acknowledgement

First and foremost, a huge thanks to Deutsche Forschungsgemeinschaft (DFG) for funding this project through the framework of GRK 1860 "Micro-, Meso- and macroporous nonmetallic Materials: Fundamentals and Application (MIMENIMA)" and all the associated supervisors for their continued encouragement and feedback. It would have been lonely without all my wonderful colleagues at MIMENIMA. I am grateful to them for just being in the same boat as me.

Among all the people who have supported me in this PhD journey, Prof. Lutz Mädler has been always a constant. Throughout these four years, he has groomed me to become a better scientist. I am always grateful to him for taking me as his student, guiding me and engaging in serious discussions or friendly arguments with me.

I am very thankful for my second supervisor, Prof. Lucio Colombi Ciacchi for happily agreeing to review my work.

In the same vein, I would like to thank (Dr.) Georg Pesch for being a friend. What a great sounding board you are! You always listened to my rambles and whines and still thought that I could do it. You are the Hermione to my Harry (sorry!).

I would also like to thank Dr. Thomas Wriedt for recognising me on the street that first day I came here. He has been there from the first and I thank him for always sharing his immense knowledge with me. A big ole' thanks to Dr. Norbert Riefler for always being there whenever I needed help with my software or code. I truly believe he knows everything there is to know about computational modeling.

I would be remiss to not thank my colleagues at IWT department who have one point or other been there for me: Alex, Dandan, Naima, Valentin, Hendrik, Adi and Apo. Not to forget, everyone at IWT is awesome and you made my stay at IWT unforgettable.

I am also grateful to Dr. Jochen Dreyer for imparting his knowledge about DSMC modeling and answering my incessant questions. I acknowledge Prof. Udo Fritsching's trust in the variable parcel method and as a consequence, in me.

I would like to thank Dr. Henrik Ström for having me at Chalmers and David for showing me the cool chip. It was fun working with both of you.

A giant thank you to Dina, Adi and Prem for being there for me personally. You helped me through some of the hard times without even knowing.

Lastly, I am grateful to my parents for believing in their little girl. Nothing would be possible without you.

# List of Publications

S Swapnasrita, GR Pesch, JAH Dreyer, N Riefler, T Wriedt, L Mädler, Implementation of parcel method for surface reactions in DSMC, Computers and fluids, 187, p. 1-11, 2019. <https://doi.org/10.1016/j.compfluid.2019.04.015>

LM, JAH and GR came up with the idea for the project. SS implemented the idea, performed all kinds of analysis with supervision from LM and TW. NR supported SS in the implementation of the concept. The paper is written by SS with input from all other authors.

S Swapnasrita, D Albinsson, GR Pesch, H Ström, C Langhammer, L Mädler, Unraveling CO oxidation reaction kinetics on single Pd nanoparticles in nanoconfinement using a nanofluidic reactor and DSMC simulations, Chemical Engineering Science: X, 9, 2021. <https://doi.org/10.1016/j.cesx.2021.100088>

SS is responsible for the model implementation and manuscript writing. DA is responsible for all experimental results. GR also participated in the model development. HS, CL and LM are responsible for the conceptualisation and securing the funding. All authors participated in manuscript revision.



# Contents

|          |  |           |
|----------|--|-----------|
| <b>1</b> | <b>Introduction</b>  | <b>1</b>  |
| 1.1      | Experimental works on CO oxidation on Pt-group metals . . . . .      | 6         |
| 1.2      | Simulation and Modeling of CO oxidation on Pt-group metals . . . . . | 10        |
| 1.3      | Monte Carlo (MC) and Molecular Dynamics (MD) . . . . .               | 12        |
| 1.4      | Density Functional Theory (DFT) . . . . .                            | 14        |
| 1.5      | Kinetic Monte Carlo (KMC) . . . . .                                  | 20        |
| 1.6      | Direct Simulation Monte Carlo (DSMC) . . . . .                       | 25        |
| 1.7      | Motivation and Problem Statement . . . . .                           | 29        |
| 1.8      | Thesis Structure . . . . .   | 32        |
| <b>2</b> | <b>The DSMC Method</b>   | <b>33</b> |
| 2.1      | Equations of Fluid Dynamics . . . . .                                | 35        |
| 2.2      | Inflow . . . . .   | 37        |
| 2.3      | Elastic Collisions in DSMC . . . . .                                 | 38        |
| 2.3.1    | Collision Sampling . . . . .   | 41        |
| 2.3.2    | Post-collisional Velocities . . . . .                                | 42        |
| 2.4      | Surface Chemical Reactions in DSMC . . . . .                         | 44        |
| 2.4.1    | Adsorption . . . . .   | 45        |
| 2.4.2    | Reaction . . . . .   | 49        |
| 2.4.3    | Desorption . . . . .   | 51        |
| 2.4.4    | Input Parameters . . . . .   | 53        |
| <b>3</b> | <b>Methodology</b>   | <b>55</b> |
| 3.1      | Simulation Domain . . . . .  | 56        |
| 3.2      | Variable Parcel Method . . . . .                                     | 57        |
| 3.2.1    | Inflow . . . . .   | 61        |
| 3.2.2    | Collision Sampling . . . . .   | 61        |
| 3.2.3    | Particle merging . . . . .   | 62        |
| 3.2.4    | Adsorption . . . . .   | 63        |
| 3.2.5    | Desorption-Reaction . . . . .  | 65        |
| 3.2.6    | Re-initialisation . . . . .  | 69        |

|          |  |            |
|----------|--|------------|
| 3.3      | Summary of all modifications from surface reaction model by Pesch et al. [78] in this work . . . . . | 71         |
| 3.4      | Experimental Validation . . . . .  | 71         |
| 3.4.1    | Sensitivity Analysis . . . . .   | 75         |
| <b>4</b> | <b>Results and discussion</b>  | <b>81</b>  |
| 4.1      | Variable Parcel Size Method . . . . .  | 83         |
| 4.1.1    | Diffusion only . . . . .   | 84         |
| 4.1.2    | Diffusion, Adsorption and Reaction . . . . .   | 91         |
| 4.2      | Sensitivity Analysis . . . . .   | 116        |
| 4.2.1    | Sensitivity analysis with varying input parameter $\theta_{\text{sat,CO}}, \theta_{\text{sat,O}}$    | 119        |
| 4.2.2    | Sensitivity analysis with varying input parameter $E_A$ . . . . .                                    | 124        |
| 4.2.3    | Sensitivity analysis with varying input parameter $\text{CO}_{\text{inlet}}$ . . . . .               | 128        |
| 4.2.4    | Pearson coefficient calculation . . . . .  | 132        |
| 4.2.5    | Sensitivity analysis of desorption parameters . . . . .  | 134        |
| 4.2.6    | Sensitivity analysis of adsorption parameters . . . . .  | 135        |
| 4.2.7    | Validation and further insights . . . . .  | 140        |
| 4.3      | Summary . . . . .  | 144        |
| <b>5</b> | <b>Conclusion</b>  | <b>149</b> |
| 5.1      | Future Work . . . . .  | 152        |
|          | <b>Bibliography</b>  | <b>155</b> |
| <b>A</b> | <b>Appendix</b>  | <b>179</b> |
| A.1      | Variable Soft Sphere (VSS) . . . . .   | 179        |
| A.2      | Sensitivity Analysis . . . . .   | 180        |
| A.3      | Input parameters . . . . .   | 181        |
|          | <b>Declaration</b>   | <b>219</b> |

# Introduction

# 1

The science of operations, as derived from mathematics more especially, is a science of itself, and has its own abstract truth and value.

---

*Ada Lovelace*

Heterogeneous catalysis is a process, in which the rate of a reaction is moderated using a catalyst that is in a different phase from the reactants and products. Heterogeneous catalysis came to the attention of researchers following the awarding of the Nobel Prize in Chemistry to Gerhard Ertl in 2007 for his many studies involving surface chemical reactions, in particular the details of the Haber-Bosch process. Ertl developed surface science techniques in high vacuum conditions to study the active participation of catalyst atoms in the reaction process. In such cases, surface chemistry gains vital importance as it encompasses the energetics of the reactants, products and any intermediary products formed along the way, and with that controls the reaction itself. Ertl's approach to understanding the surface kinetics is to understand reactions in a more nuanced manner than before. Since then, industrial production has centered around different heterogeneous catalytic processes such as fuel cells and semiconductors, ozone layer conservation and CO<sub>2</sub> capture, fertiliser and chemical production.

Aside from zeolites and enzymes, metal and metal oxides are the common heterogeneous catalysts used in chemical industry. Noble metals such as Pd, Pt and Au have shown to be excellent choices for emission control catalysis, water oxidation electrocatalysis, hydrogenation of alkenes, etc. The most common usage of catalysed reactions is in catalytic converters used in our vehicles. The converters often contain transition metal on porous substrates to control and eliminate exhaust of poisonous gases such as carbon monoxide into the atmosphere. CO makes its way into the atmosphere from numerous sources, be it man-made or natural. It is introduced to the atmosphere mainly through incomplete combustion of fuels as in wood stoves, vehicles, factories, tobacco burning. Natural causes such as volcanic eruptions or forest fires also emit a lot of CO directly into the air. Inside the human body, the main source of CO is from the heme-oxygenase of heme in blood cells. Other minor

quantities may come from lasers used in laproscopic procedures, or anaesthetic equipments that utilise drying materials such as soda lime or barium hydroxide [1]. This gas is one of the prominent reagents employed in industries. It is used in the hydrogenation of alkenes, formation of phosgene (used to make plastics) and acetic acid. It is also a participant in water-gas shift reaction which is utilised to produce pure hydrogen which is then used in Fischer-Tropsch synthesis and Haber-Bosch process. It is most commonly used in production of synthesis gas (syngas) to be employed in manufacturing of ammonia and methanol. CO is used to make high-powered infrared lasers and in reduction of metal ores. CO oxidation is the common reaction in fuel cells and semiconductor sensors. It reacts easily with haemoglobin in the blood, which leads to poisoning in humans. But more studies are coming to find application for this property for pharmaceutical purposes to achieve targeted drug delivery and use it as a medium for anti-inflammatory and cardiovascular therapy. As it is such a prevalent gas, CO oxidation has been studied for years to develop model catalysts.

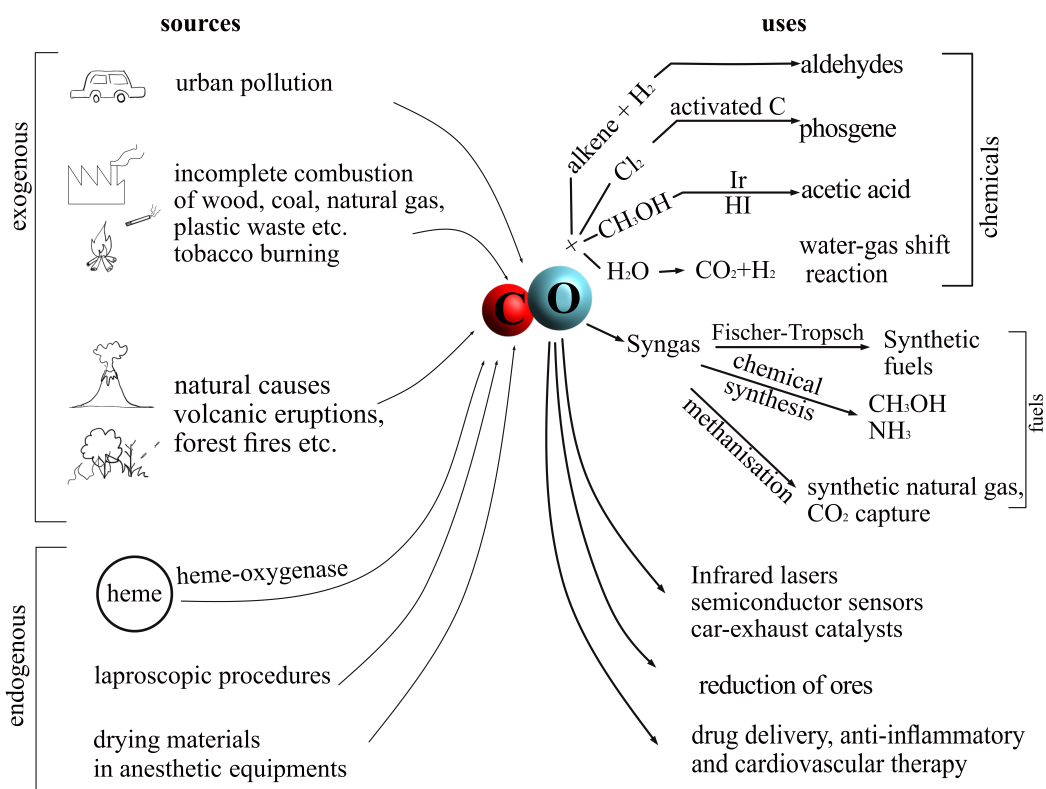


**Fig. 1.1.:** CO oxidation is one of the many reactions that is the focus of understanding heterogeneous catalysis. It has been and still is relevant to modern society and industry. CO sources from human beings, nature and man-made objects and finds uses in industry in varying capacity.

With good reason, this is one of the most intensively studied reaction system in the history of heterogeneous catalysis (over 100,000 papers over the last fifty years; 50,000 related to catalysts; > 9000 involving noble metals specifically, according to Scopus search results analysis). Some of the most notable works in the research area of CO oxidation on noble metal catalysts are those of molecular beam experiments by Engel and Ertl [2–16]. All research is mostly done in specific structures at model conditions and it is inherently difficult to link all the model studies to a real catalyst. To complement that, numerical modelling has also been performed with this reaction in focus [17–31]. One of the core difficulties in optimising a heterogeneous catalyst system is the inherent interdependence of the mass transfer and kinetics. It involves generations of testing different additives, structures, experimental conditions and supports to improve a reaction system. With the advent of newer technologies, newer avenues open up to approach the old technical systems once more. With increasing computational power and leading research in numerical modelling, it has emerged as a useful tool in understanding heterogeneous catalysis. It is non-invasive and often cheaper compared to experimental trial-and-error methods. The modelling can be done at a very detailed level or engineering level. At mesoscale, the simulation follows quantum approaches or Newtonian approaches to follow trajectory of molecules. At macroscale, it requires solving heat and mass transfer equations that can be applied to reactors. Focus can be directed to systematically optimise the structures of reactor systems to have the catalyst always in an active state despite the dynamic behaviour of the gas flows. However, numerical modelling is still developing and CO oxidation with its huge experimental database serves often as a benchmark test for validation.

## 1.1 Experimental works on CO oxidation on Pt-group metals

A variety of experimental techniques have been used to probe the chemical reaction on Pd catalyst and study the interaction of adsorbed CO and O<sub>2</sub> and effect on the overall reactivity, such as Auger Electron Spectroscopy (AES) [9, 10], Infrared Spectroscopy techniques such as polarization modulation Infrared reflection absorption spectroscopy (PM-IRAS) [5, 11], Planar laser-induced Fluorescence (PLIF) [12], mass spectroscopy [13–15, 32], Electron Energy loss spectroscopy (EELS) [33] with low-energy Electron Diffraction (LEED) [4, 32–34] and X-ray Photoelectron Spectroscopy (XPS)[5, 12]. This reaction has been studied in high [5, 9–11] and low pressure conditions [2–5, 11, 13–15, 32, 34]. There are three potential mechanisms

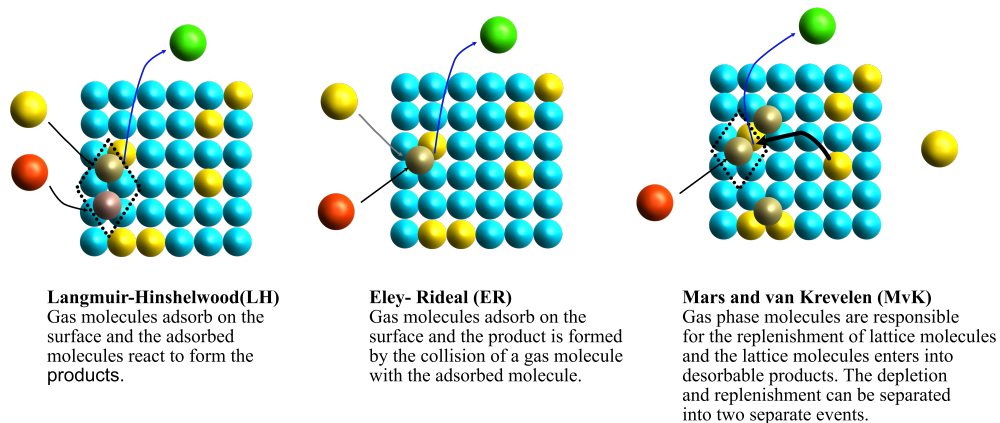


**Fig. 1.2.:** Different reaction mechanisms proposed for CO oxidation on metal oxides. Red and Yellow: Reactant gas molecules, Green: Product, Blue: Catalyst atoms.

that explain CO oxidation on Pd, mainly Langmuir Hinshelwood (LH), Eley-Rideal (ER) and Mars and van Krevelen (MvK) (figure 1.2). However, there is a majority agreement that CO oxidation proceeds via a LH mechanism on Pd or Pd-supported catalysts. This is further validated by the works of Engel and Ertl that show that the surface residence times of both CO and O on Pd(111) is large enough to suggest that the LH mechanism is the most fitting theory. There is a complex relationship between the co-adsorption of CO and O<sub>2</sub>. While many agree that CO adsorbs non-dissociatively and O<sub>2</sub> adsorbs dissociatively, there is no consensus regarding the dominance of one species. To further complicate things, CO compresses adsorbed oxygen into islands often forming much more intimate contact and increasing the local coverage of oxygen [2, 4, 33]. There are also differing opinion on the relationship of the overall reaction rate and temperature. Below is a summary of the observations of some of the highly-cited papers on this topic.

- Some studies show that the steady state kinetics of this reaction are independent of the structure orientation while some argue otherwise [11]. So the results of Pd(111) can be translated to any Pd surface. [2, 4]. Others show that the particle size had an effect on the reactivity of the catalyst [9].
- Some researchers argue that CO oxidation on Pd is purely via the Langmuir-Hinshelwood [2–4, 10] while some studies show the existence of Eley-Rideal mechanism along with LH [13, 14].
- Similarly, researchers have yet to find an agreement for the order of the reaction in terms of partial pressures of CO and O<sub>2</sub>. Many studies found that the rate of reaction depends on the O<sub>2</sub>/CO ratio [10, 14]. Engel and Ertl report

a zero order dependence on  $p(\text{O}_2)$  at lower coverage than 0.8 and first order dependence on  $p(\text{CO})$  and  $p(\text{O}_2)$  for higher coverage on the determination of the reaction rate [2, 3].

- It has been also discussed that there is no strongly bound oxide at higher temperatures as it gets reduced by CO [10] while others have shown that oxygen-covered surfaces show higher catalytic activity [9, 27]. Gao et al. report an initial increase in reaction rate and a decrease later for highly oxidizing mixtures ( $\text{O}_2/\text{CO} \gg 5$ ) [5]
- One well-agreed upon theory is adsorbed CO hinders O absorption thus lowers the reaction rate at higher temperatures [2–4, 11, 13, 33]. Similar level of agreement is also seen for the low surface lifetime of  $\text{CO}_2$  [2–4, 20]. Most of the papers also seem to agree that  $\text{O}_2$  desorption occurs at temperature above 800 K [15] while CO desorption already takes place above 200 K [5, 13–15].
- The activation energy for the reaction varies across literature from the numerical studies of Creighton et al. at 83 kJ/mol [35] to the AES supported experimental values of 138 kJ/mol [10]. Many also note that there is a lowered energy barrier at higher CO coverage [2].
- The initial sticking coefficient of CO is close to unity and decreases with increasing coverage. It is independent of temperature and the angle of incidence of the molecule. The initial sticking coefficient of  $\text{O}_2$  is close to unity and decreases with increasing coverage and temperature. It is independent of the angle of incidence of the molecule [2, 3].

Clearly, there is an existing gap in the understanding of the specifics of the reaction at a local microscopic level. The whole spectrum of conclusions is arrived at due to the absence of one specific catalyst system simultaneously, therein lies the beauty of experimentation: All conditions that can be tested have been tested using different kinds of techniques. All that is required, is to use the varying pieces of information and present a unified theory that satisfies most of the existing literature and disproves some of them along the way. Attempts are being made to combine different mechanisms and provide comparative results at a glance to choose the best mechanism for the user. A fine example is the CaRMEN (Catalytic Reaction Mechanism Network) software developed by Gossler et al. to compare proposed kinetic models and find suitable reaction mechanism for matching conditions [36].

## 1.2 Simulation and Modeling of CO oxidation on Pt-group metals

Catalysed reactions occur over different scales and at different rates at different sites of the catalyst surface. Diffusion occurs within nanoseconds or microseconds but over several micrometers; Adsorption occurs within femtoseconds or picoseconds but within nanometers and reactions occur in nanoseconds and within several nanometers. The goal of molecular simulations is to provide a deeper insight into the elementary processes occurring on a catalyst surface bridging micro- (0.2–2 nm), meso- (2–50 nm) or macroscopic (50–1000 nm) level.

The starting point of any molecular simulation would be to solve the Schrödinger equation for all the electrons at all time steps. But, that is an impractical solution, to say the least. To simplify this approach, one could construct approximate potentials for all involved nuclei and solve Newton's equations of motion. This approach is referred to as Molecular Dynamics method but it is still relatively slow to other available methods. Integrating a huge set of equations, even if it is for a small number of molecules, at the time scale of atomic vibrations ( $10^{-13}$  s) is still quite a time-consuming effort. There are other simulation tools available to investigate the heterogeneous reactions in the porous catalysts. As discussed above, modelling catalysis is a multiscale problem. At the microscopic scales, density functional theory (DFT) is the most popular tool for estimation of vibration energies of electrons and thus atomic parameters. Kinetic Monte Carlo (KMC) is a statistical method employed at mesoscopic level to predict the average reaction rate [37]. Computational Fluid Dynamics (CFD) is a macroscopic scale tool used for reactor designing. So, there is a need to bridge the gap via the applicability of different bottom-up multiscale models to understand the fundamental behind catalyst activity [38–40]. Efforts are made to create hybrid models for this purpose, such as, DFT/MM models, CaRMEN, OpenFOAM-DSMC, DFT-KMC or ab-initio KMC.

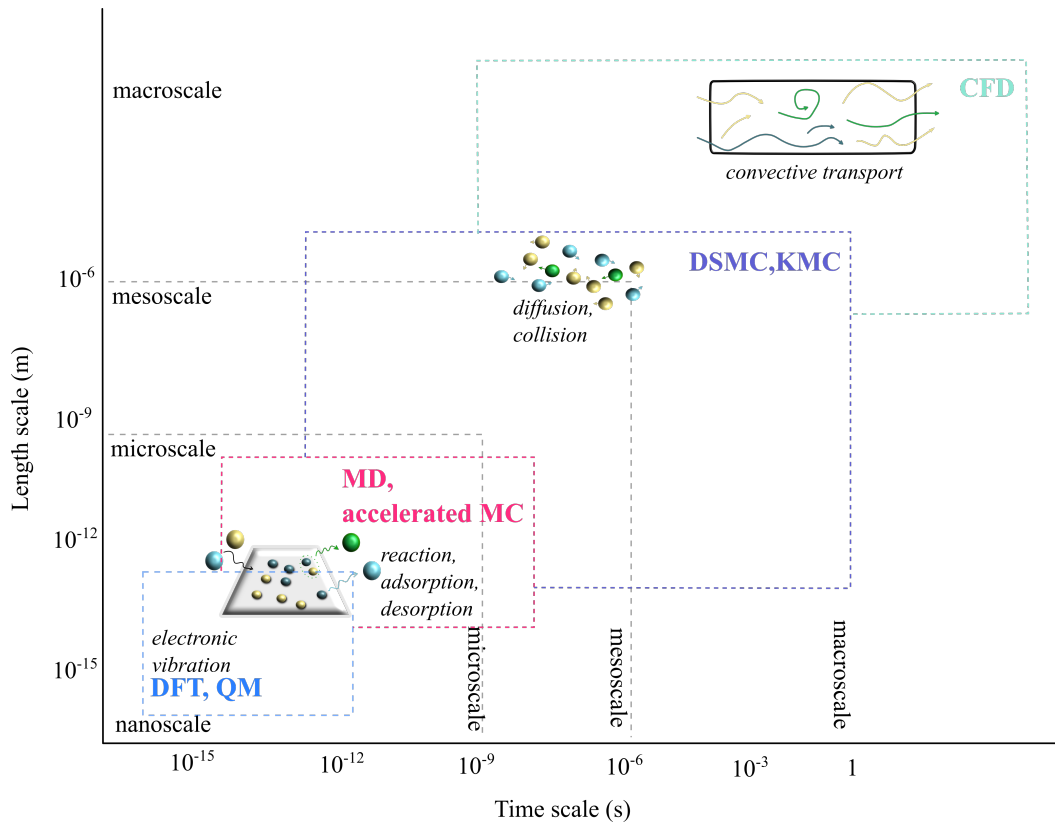


Fig. 1.3.: Hierarchy of available multiscale models.

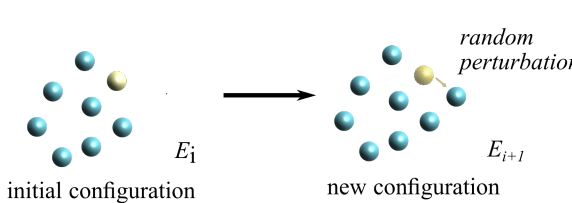
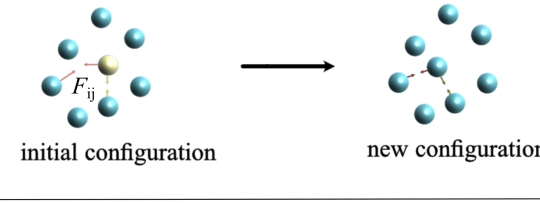
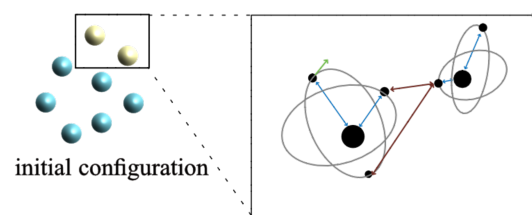
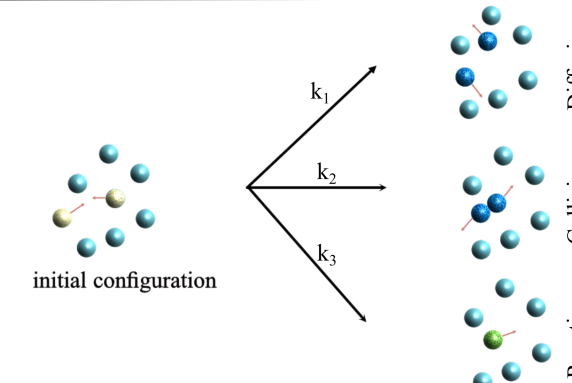
### 1.3 Monte Carlo (MC) and Molecular Dynamics (MD)

The earliest numerical methods proposed to study molecular motion are the Monte Carlo and Molecular Dynamics method. While the former is stochastic in nature, the latter is deterministic. MC refers to any simulation that uses random numbers in simulation. The Metropolis MC sampling approach, given by Metropolis et al. [41], samples all stable atomic configurations of the system by randomised movement of individual particles. The molecules (one or multiple) could undergo any random movement starting from any random position. The final position was determined by evaluating a transition probability, depending on the energy of the initial and final state. This method was fast and it made the calculation of properties of interacting molecules more accessible. MD is a numerical method based on molecular mechanics where the movement of each individual molecule is tracked assuming a given potential energy function [42]. This provides an insight into the microscopical behaviour of fluid flows. Each atom is moved according to Newton's laws of motion and simple partial differential equations need to be solved. Both methods compared well with analytical theories and were able to provide in-depth

understanding unavailable by experimental methods at the time. Sometimes, it went beyond the theories and helped in understanding obscure phenomena [43, 44]. As the system size became larger, molecular modelling became crucial as statistical methods are inadequate to address even three-body problem. The original problems considered in MD started with hundreds of atoms. Since then, numerous modifications have followed such as quantum MD, kinetic MC, direct simulation MC etc. and these methods have dominated molecular modelling. The MD time steps are in the order of few femtoseconds to resolve atomic vibrations, so, it may take millions or trillions of time steps for a microsecond event. However, molecules are in a constant state of motion and one needs to simulate for longer times to reach all the favourable arrangements of the energy surface. Furthermore, the molecular mechanics energy fields are continuously being developed but they are inherently approximations and needs user's experience to decide the best choice of force fields to use. Ahmed et al. used the Quantum Chemical MD study to investigate the mechanism of CO oxidation on MgO supported Pd particles [45]. They found the binding energies of CO adsorption on different sites, the top site being the preferred site. They also observed that CO<sub>2</sub> desorption is instantaneous. Considering that the method is resolved in femtoseconds, it is a good tool to analyse bond breaking, stretching or formation. But they only considered 200 atoms. MD requires extremely large computational resources to scale-up. Thus, MD is now more commonly used for biochemistry and biophysics. MC only gives accurate averages for the positions of molecules and only equilibrium properties can be evaluated. Regardless, these methods are ground-breaking approaches to molecular modelling and modern methods are still based on them.

## 1.4 Density Functional Theory (DFT)

Density Functional Theory (DFT) is a one-determinate exact solution of the Schrödinger equation used to explain the ground states of systems using exchange-correlation functionals [46]. All the complexities associated with the many dimensional wave functions for systems with many electrons are hidden by the one determinable variable, the exchange-correlation functionals. However, it is observed frequently, this functional is unclear and approximations such as generalised gradient approximation [47, 48] and local (spin-) density approximation [49] are necessary but inevitably make the solution empirical [50]. Hinuma et al. did a comparative study on seven generalised approximations and observed that the stability of phases of different metal oxides are better predicted with some approximations only [51]. They also

|            |  |  |
|------------|--|--|
| (a)<br>MC  |  <p>initial configuration <math>E_i</math> → new configuration <math>E_{i+1}</math> (random perturbation)</p> | $\text{if } \exp\left(\frac{-(E_{i+1} - E_i)}{k_B T}\right) > R$ <p>accept new configuration<br/>else reject<br/>Repeat for total number of steps</p>  |
| (b)<br>MD  |  <p>initial configuration → new configuration</p>   | $F_{ij} = F_{\text{coul}} + F_{\text{vdW}} + F_{\text{el}}$ $a_i = \frac{F_{ij}}{m_i}$ $i(x_i, v_i) \xrightarrow{a_i dt} i+1(x_{i+1}, v_{i+1})$ <p>Repeat for all time steps</p>   |
| (c)<br>DFT |  <p>initial configuration</p>   | $E_{\text{tot}} = E_{\text{kinetic}} + E_{\text{ne}} + E_{\text{el}} + E_{\text{xc}}$ <p>Find configuration with lowest <math>E_{\text{tot}}</math></p>  |
| (d)<br>KMC |  <p>initial configuration</p> <p>Diffusion<br/>Collision<br/>Reaction</p>                                    | <p>Calculate rate constants</p> $k_i = \sum_{j=1}^i k_j \quad k_W = \sum_{j=1}^W k_j$ <p>where W is the total number of transitions</p> <p>Find event <math>i</math> such that,<br/><math>k_{i-1} &lt; Rk_W &lt; k_i</math></p> <p>Forward the time step</p> $\Delta t = -\frac{\log R}{k_W}$ <p>Calculate new rate constants after making transition <math>i</math></p> |

**Fig. 1.4.:** Steps involved in available molecular simulation models. (a) Molecular MC depends on finding molecular configurations with lowest internal energy through random displacements of one molecule at a time. For this, the difference between initial and final state energy is compared to a random number. Several states are then sampled to find average molecular properties. (b) In MD, atoms/molecules are moved according to the cumulative force experienced by them (coulombic force  $F_{\text{coul}}$ , van der Waals force  $F_{\text{vdW}}$  and electron-electron repulsion  $F_{\text{el}}$ ). With an exact description of forces, the trajectory of the system is established via Newton's laws of motion. (c) The main goal of DFT is to find the ground state for atoms/molecules/systems. Since a multi body problem still remain an unsolvable problem, DFT approximates that the ground state can be established by knowing the energy density functional constructed from kinetic energy  $E_{\text{kinetic}}$  (green), nucleus-electron attraction  $E_{\text{ne}}$  (blue), electron-electron repulsion  $E_{\text{el}}$  (red) and Pauli-Exclusion Exchange Correlation energy  $E_{\text{xc}}$ . (d) The first step of KMC involves making a list of all transitions( $W$ ) and its corresponding rate constants. A random transition step is chosen and the time step is forwarded by a random time step.  $R$  is a random number between 0 and 1.

showed that some phases of a particular metal oxides are unclear from certain approximations. This coupled with the enormous computational load involved in DFT makes it impossible to use for complex surface chemical reactions. Nevertheless, DFT has been used to study oxidation of CO on Pd lattices albeit for a small group of atoms only.

Zhang et al. suggest that the adsorbed O becomes activated and moves towards a bridge site on the crystal lattice and if a CO molecule moves towards the adsorbed O, then CO<sub>2</sub> may be formed. The activation energy is a sum of activation energy of CO and O, surface relaxation energy and the bond formation between O and CO including the energy required for the bonding competition between CO-O<sub>ads</sub> and O<sub>ads</sub>-Pd [26].

Li et al. studied the oxidation of highly dispersed Pd-NPs on graphene substrate. They propose that CO oxidation in such a configuration takes place via LH mechanism. Chemisorbed O and CO react exothermally to form CO<sub>2</sub> [22].

Rogal et al. suggested that O<sub>2</sub> is adsorbed into two neighbouring sites and CO undergoes unimolecular adsorption without any adsorption barrier. Adsorbed O and CO separate into domains, reason being the higher repulsion between O<sub>ads</sub> and CO<sub>ads</sub> compared to O<sub>ads</sub>-O<sub>ads</sub> and CO<sub>ads</sub>-CO<sub>ads</sub>. They instead argue for the reaction occurring on a thin sub-nanometer oxide film, where the two species are differently arranged on the oxide overlayer. The activation barrier in this case is half of the activation energy on the pristine Pd lattice, according to their calculations. The surface oxide disrupts at higher CO partial pressure at lower temperatures and is quite stable at higher temperatures even for very high partial pressures. The produced CO<sub>2</sub> is readily desorbed from the surface and the sticking coefficient is so low that readsorption is generally omitted [17–19].

Salo et al. suggest that the bonding between adsorbed CO and O atom may occur via different mechanisms, through the rotation of the C atom of CO towards the adsorbed O or the total displacement of the CO molecule towards the adsorbed O. Depending on the lattice site, both proceed to the transition state and the adsorbate bond is broken [20].

Esfafili et al. have studied CO oxidation over single Pd atom attached to a nitrogen doped graphene and they concluded that this occurs through tertiary ER mechanism. Even at this atomic level, they have calculated that CO adsorption is favourable compared to O adsorption. The O atom is then physisorbed on the presorbed CO molecules. The intermediate transition state is formed when the bond separation between the adsorbed O<sub>2</sub> and CO reduces. CO<sub>2</sub> is then formed at the cost of a small activation energy [21].

Duan et al. also performed DFT simulations of CO oxidation on Pd(111) surface and observed that the surface reaction proceeds through ER mechanism. Compared to

LH mechanism, the energy barrier is almost 20 times lower. However, the surface oxide phase Pd<sub>5</sub>O<sub>4</sub> is a more stable phase and is the preferred reaction pathway according to their simulations [30].

Vogel et al. have presented that bistable high-reactivity and low-reactivity conditions exist for temperatures below 513 K. They have attributed the bistability to the poisoning and recuperation of the surface from CO poisoning [52].

All these studies provide activation energies which are mainly dependent on the position of CO and O atom on the lattice surface before moving to the transition state. The activation energies are summarised in table 1.1. All the DFT simulations are performed on a small number of atoms and are still computationally exhaustive. DFT can be combined with the speed of the Molecular Mechanics method, also known as QM/MM methods, to achieve real reaction ensembles at reasonable computational cost [51, 54–57]. The participating atoms of interest are analysed using DFT while the larger regions are economically handled with MM. The regions are coupled by devising an inter-related potential between electrostatic and van der Waals force [55]. However, resolving at such small time scales makes it impossible to reach even few microseconds of a real system evolution. Heavy parallelisation and larger computational capacity has helped the method to reach nanoseconds of simulation time.

**Tab. 1.1.:** Activation energies calculated from DFT and KMC calculations of CO oxidation on different Pd structures.

| Reference                | Activation Energy (kJ/mol) | Remarks  |
|--------------------------|----------------------------|--|
| Zhang et al. [26]        | 144<br>101                 | Pd(111);<br>Pd(100)<br>$\theta_{\text{satCO}} = \theta_{\text{satO}} = 0.25$ |
| Rogal et al. [17–19]     | 96<br>48-86.4              | Pd(100)<br>Pd-oxide  |
| Salo et al. [20]         | 102.3-238.3                | depends on the position of CO and O and final orientation of CO <sub>2</sub> |
| Li et al. [22]           | 61.3-81.2                  | depends on size of Pd atoms  |
| Esfarili et al. [21]     | 24.1                       | single Pd atom   |
| Kunz et al. [28]         | 94<br>70.4                 | Pd(111)<br>Pd(100)   |
| Piccinin et al. [29, 53] | 5.75-22                    | decreases with temperature   |

## 1.5 Kinetic Monte Carlo (KMC)

Monte Carlo simulations have developed over the years to approach equilibrium properties as well as non-equilibrium or dynamical properties. Kinetic Monte Carlo falls in the latter category. A typical Kinetic Monte Carlo (KMC) procedure would start with preferred lattice specifications, reaction mechanism involved, the associated energies. The simulation progresses through random times at the end of which all the reaction step and the lattice configurations are updated before starting the next step. In the short dynamics of states between the occurrences of such events, all intermediate events are independent of the previous states [19]. The final data obtained from each time step can then be post-processed to get minute details about the ongoing reaction process. If the rate constants are properly catalogued, the results from a KMC simulation will be similar to MD, at cheaper expense. However, a lot of computational power is dedicated to the selection of the simulated events and updating the data after each time step. It is assumed that our knowledge of the reaction dynamics of a system's dynamical evolution is full-fledged, which in reality, may have surprising mechanisms involved leading to large deviations from real systems. KMC has been extended to be able to model surface defects, adlayer structure and spatial inhomogeneity in general associated with catalysts [39].

Piccinin et al. conducted a first-principles based KMC study of CO oxidation to detail out the processes involved in Pd lattice reorganisation and its consequences on the reaction rate. They observed an increase in catalytic activity at 320 K when the structure reordered from  $(2 \times 2)$  to a  $(\sqrt{3} \times \sqrt{3})$  structure. They calculated an activation energy of 22 kJ/mol at lower temperatures and 5.75 kJ/mol at 320 K. They attributed this reduction to the repulsions between the neighbouring atoms leading to a reduced reaction barrier. The  $\text{CO}_2$  gas molar fraction is considered to be zero and  $\text{CO}_2$  dissociation is neglected in the simulation.  $\text{O}_2$  associative desorption from the surface has an energy barrier of  $\sim 180$  kJ more than other processes and can be neglected. They have observed CO poisoning. Also, they observed that the reaction rate is similar to the rate of CO adsorption. [29, 53]

Liu et al. also conducted a DFT-supported KMC study of CO oxidation on Pd. They found a region of bistability of CO and O coverage below a certain critical temperature. There are two variants of phase separation of CO and O that have the same energy and thus, the fluctuations are seen. They proposed that the oxidation follows LH mechanism [23].

Matveev et al. studied the presence of surface concentration waves that were a result of changing the partial pressure of  $\text{O}_2$ . They attributed the presence of this characteristic wave to the inclining and declining concentration of the sub-surface

oxygen. The CO adsorbed on the surface reacts with sub-surface O<sub>2</sub> and opens up active vacancies. The O<sub>2</sub> then adsorbs on this free sites and travels on the surface and recedes into the surface. The concentration of O<sub>ads</sub> reaches a maximum and then decreases as the sub-surface O<sub>2</sub> rises again slowly and the cycle repeats. They have noticed different patterns on the adsorbates concentration, namely spiral, turbulent, ring like, striped all depending on the kinetic prehistory of the system [31].

A similar Monte Carlo study was done by Latkin et al. to understand the CO oxidation kinetics. They confirmed the presence of sub-surface oxygen along with the LH mechanism [24]. These simulations are based on the experimental findings and hypotheses of Ladas et al. They observed that such an oscillation behavior was present only at low temperature and high  $p_{\text{O}}$  (pressure in the range of  $10^{-6}$  atm) [25].

Kunz et al. have performed the CO oxidation simulation in their own KMC solver MoCKa (Monte Carlo Karlsruhe). They observed that O<sub>2</sub> adsorption is generally inhibited by CO. In the absence of CO, O<sub>ads</sub> reaches a coverage of 0.3-0.4. With the addition of CO, O<sub>2</sub> is consumed in the process of CO oxidation and there is a decrease in O<sub>ads</sub>. This conveys that the adsorption probability of CO is higher than O. The system then shows signs of CO poisoning as the reaction rate reduces. They have calculated an activation barrier of 94 kJ/mol on Pd(111) and 70.4 kJ/mol on Pd(100) [28].

Reuter et al. have conducted multiple first-principles based KMC studies on various Pt-group metal. In a study of CO oxidation on Pd(111), they have shown that a surface oxide layer is stable at temperature of 300 K for a pressure ratio less than  $p_{\text{CO}} : p_{\text{O}} = 1 : 10$ . The oxide layer is destabilised upon increasing the pressure of CO. With increasing temperatures, the ratio of  $p_{\text{CO}} : p_{\text{O}}$  can reach 1 : 1 without any destabilisation [19].

KMC is often coupled with first-principles DFT and TST (transition state theory) to study gas and mass transfer limitations to reduce computational expense [19, 58–60]. Surface kinetics are modeled with coupled KMC and first principles simulation [19, 58–63]. Hansen et al. simulated unimolecular and bimolecular reactions with binding energies obtained from DFT calculations [61–63]. Henkelman et al. developed on-the-fly kinetic Monte Carlo for performing longer time scale simulations. They argued that specific state based rate catalogs could be developed to predict possible future atom configurations with lower computational load and this method also scaled up [64]. Later, Domain et al. proposed “object” kinetic Monte Carlo (OKMC) to study radiation defects in Fe alloys [65]. According to their model, point defect and point defect cluster (which were commonly vacancies, dislocation loops) could be seen as an object with a certain center-of-mass position in space. Then these objects were migrated according to lattice distances rather than atomic

distances as in case of usual KMC. They described this approach as a good trade-off between reliability and computing time. With time, OKMC has been improved but is still largely used in this specific field of radiation study.

However, there are certain limitations inherent to all kinds of KMC simulations, although it is now possible to simulated up to 50 ms with an accuracy equal to traditional MD simulation [66]. The randomness in the time selection can give rise to sampling error but this can be avoided by running longer simulations. KMC simulations are hard to debug as any programming error could provide misinformation about kinetics that often go unnoticed or interpreted as a unique result. An approximate  $10^2$  rate constants have to be predetermined, often through DFT simulations, for a simple lattice. If one of the rate constants (often determined from DFT which has a lot of potential approximations) is wrong, the whole process could be invalid as the randomization is heavily dependent on the rate constants [28]. The other limitation of the process is the assumption of knowing escape paths in advance. The source of all the guessed mechanisms is often from a scientist's intuition and is prone to have certain lackings.

## 1.6 Direct Simulation Monte Carlo (DSMC)

Direct Simulation Monte Carlo (DSMC) was developed in 1976 as a microscopic molecular modelling tool for the aerospace community. It can be used for modelling mass transport at rarefied conditions, for example, for the design of high vacuum instruments or any reactor that warrants the use of high vacuum. The DSMC method uses the statistical nature of multiple collisions occurring in microscopic and mesoscopic systems when a gas is considered rarefied. A gas can be characterised as rarefied when the mean free path is much larger than the characteristic length scale, often the ratio is also called Knudsen number ( $Kn$ ). Gas flow under rarefaction can be divided into four accepted regimes: continuum, slip-flow, transition and free molecular. Of the four regimes, DSMC is best applicable in the rarefied regime, also known as the transition regime, when  $0.1 < Kn < 10$ . DSMC decouples the collision and transport processes by considering the time step less than the mean collision time.

Four major processes are at the core of any DSMC algorithm. In the computational domain, simulated molecules in the system represent  $n$  number of real molecules. The first primary process is to move the molecules and apply boundary conditions. Mass conservation laws are observed at this stage by preserving the number density of molecules in each cell. The second vital step is to index all the molecules

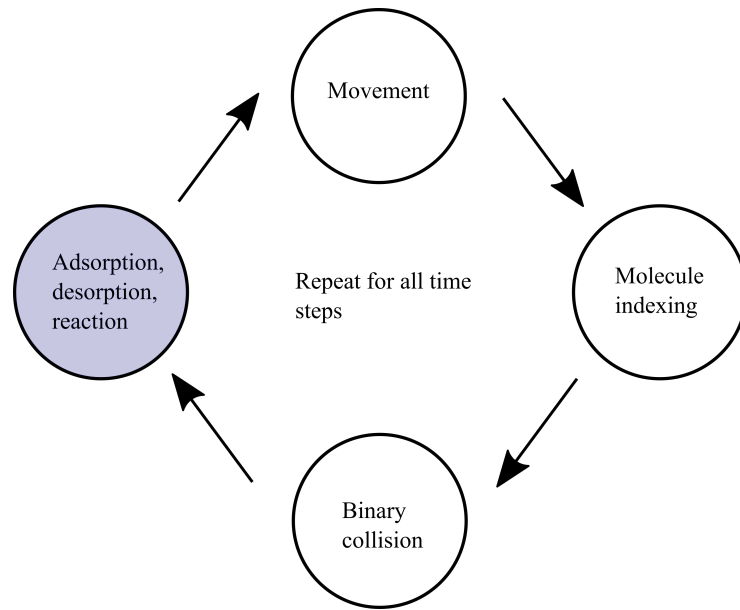


**Fig. 1.5.:** Basic schematic of the Direct Simulation Monte Carlo (DSMC) method.

according to their position and cell location. Indexing in DSMC is based on dividing the computational domain into cells and then further into subcells. This is a prerequisite for the next two steps. This cell network should be large enough to evaluate macroscopic flow properties for the gas flow. The third step is the collision process. Typically, the no-time-counter method is used within subcells [67]. Collisions are only considered between neighbours in a sub-cell. Collisions are calculated statistically based on collision probabilities which can be evaluated from molecular models described later. The final step is to sample the macroscopic properties that are calculated from the geometric center of each cell considering the position and velocity vectors of each simulated molecule in the cell. The basic schematic of a simple DSMC scheme is shown in figure 1.5. DSMC is mostly used for simulating non-equilibrium flows near reentry vehicle. At high altitudes, any chemical reaction can increase the heat on the vehicle and that can result in disasters. DSMC particles, which is termed *parcels*, can represent  $n$  real gas molecules. Due to this property, a large number of gas molecules can be handled simultaneously. The resulting flow parameters can then be averaged. This DSMC feature is used in the present thesis to improve computational efficiency.

The model used to simulate homogeneous reactions is the total collision energy (TCE) model. TCE model is based on the unphysical assumption that continuum rate equations can be comparably changed to reactive collision cross-section [67]. Bird used a ratio of reaction cross-section to total cross-section to determine the reaction probability [68]. A reaction only takes place if the total translational energy

along with the internal energy exceeds the activation energy. This is known as the total collision energy (TCE) method. An improved model was given by Lilley and Macrossan to decouple the collision and reaction steps [69]. A required number of “reaction steps” are performed based on the state of the concerned cell in the simulation volume. The reaction rate may be resulting from any experimental or theoretical source such as the Arrhenius rate equation. TCE has been employed to study reactions occurring in hypersonic atmospheric reentry vehicles [68, 70]. Gimelshein et al. used a weighing method called Majorant Frequency Scheme (MFS), developed by Ivanov and Rogasinsky, to compute weights of surface recombination and chemically reactive collisions derived from TCE. They modelled visible glow radiation of NO<sub>2</sub> on the surface of spacecraft due to recombination of NO and O<sub>2</sub> at high altitudes [71, 72]. In later years, as heterogeneous reactions started gaining attention, surface reactions had to be introduced in to DSMC.

In 1999, Choquet used Monte Carlo numerical method to study the recombination of oxygen on reaction-cured glass surfaces using probability distribution functions for adsorption, desorption and recombination. Only adsorption of atoms was considered as the dissociation process was negligible compared to recombination process. The probability distributed atoms into two groups, one allowed to recombine, to replace other atoms upon collision with surface and the other group reflected back into the gas [73]. Molchanova et al. used the catalytic recombination probability as a measure to calculate surface heterogeneous chemical reaction [74]. This probability was influenced by the gas and solid species involved and the temperature of the surface involved. The lifetime of each molecule,  $t_p$  on the surface was calculated based on the frequency of the process,  $v_p$ : desorption, adsorption or recombination.

$$t_p = -\ln R/v_p \quad (1.1)$$

where  $R$  is any random number between 0 and 1. The involved processes are then implemented assuming a Poisson distribution. The collision events are implemented each time step and surface events occur only if sufficient time has passed [75, 76]. It was later modified to the Quantum-Kinetic (QK) model, where the reaction probability is based on fraction of molecules with sufficient vibrational energy to recombine or dissociate [68]. Dreyer et al. simulated gas diffusion in porous Pd structures using DSMC [77]. Based on this, surface-based chemistry models to study oxidation of CO in mesoporous Pd have been designed by Pesch et al. [78]. Pesch et al. calculate adsorption probabilities from Kisluik’s precursor model. The reaction and desorption model are based on Arrhenius type equation.

## 1.7 Motivation and Problem Statement

Surface chemical reactions involve many elementary processes of varying time and length scales. A number of nanoreactors are being synthesised to study the influence of morphology, size and surface atoms on the overall reactivity and selectivity in the porous networks. The Physics group in Chalmers have designed such a microfluidic device that consists of nanochannels with embedded catalyst particles in a series. They have explored plasmonic sensing to study fluid flow and chemical kinetics in the mesoscale [86]. However, such a device embedded with Pd would have less response to plasmonic sensing compared to other metals, Ag or Au [87]. The thesis focuses on the mass transport and chemical kinetics occurring at such scales. Numerical modelling provides an alternative to look into such systems but it requires bridging of multiple scales simultaneously. Direct Simulation Monte Carlo (DSMC) provides a way to simulate chemical flows in rarefied regime and retain data at both meso and macroscale. The data available from such simulation can help extract system behaviour, generally inaccessible to experimental methods.

The thesis features the implementation of a variable parcel method (described in Chapter 3) to make the computation of surface chemical reaction easier. The chemistry method developed earlier followed the collision, adsorption, desorption and reaction trajectories of individual molecules [78]. This impeded the speed of computation and despite heavy parallelisation, the application has been scarce.

The main aim of the thesis is to adapt the developed surface algorithm of Pesch et al. to parcels and reduce the computational effort in the process without compromising the accuracy. The DSMC algorithm is designed to represent a flow with equivalent simulated molecules rather than single molecules to optimise computational time. Simulating chemical reactions with equivalent parcels of equal size is however complicated. A flow with chemical reaction has spots of different concentration of reactants and products dependent on the reaction front. Using parcels of equal sizes would introduce discrepancy in concentration profiles predicted by the simulation. The variable parcel method has been used earlier to model different droplet sizes in spray atomisation [88]. They proposed a new collision partner selection algorithm for parcels of different sizes. Nanbu proposed collision algorithm for reaction systems consisting of electrons, radicals and ions of different weights [89].

The aim of the work is to **(I)** extend the surface algorithm with a variable parcel method to make the computation efficient, **(II)** perform sensitivity studies to have a better understanding of different parameters in this simulation and **(III)** validate the simulation with experimental results.

## 1.8 Thesis Structure

The essential steps of the thesis has been divided into 3 chapters.

In **Chapter 2**, the DSMC method developed by Pesch et al. is discussed [78]. In this chapter, the separate adsorption, reaction and desorption model used in the algorithm is discussed. It also includes the definition of all the parameters needed in the simulation of CO oxidation on mesoporous Pd catalyst. The results from Pesch et al. serves as a benchmark for the accuracy of the developed algorithm. In **Chapter 3**, the modification of the earlier discussed algorithm with a new collision-pair selection and a post-collision velocity assignment method is discussed. The adsorption, reaction and desorption models are also adjusted in the implementation of this variable parcel method. In **Chapter 4**, the concentration profiles obtained after the implementation of the proposed algorithm are compared. Sensitivity studies are performed on the various adsorption, desorption and reaction parameters. The results of the sensitivity study are used to validate the simulation against experimental results. In **Chapter 5**, conclusions are drawn from the work done for this thesis and explore further work possible in this area.

# The DSMC Method

A theory that enables us to do new things constitute knowledge.

---

*N. K. Jemisin*

DSMC is a Lagrangian method of tracking evolution of position and properties of individual molecules with time. The time step is chosen such that motion can be decoupled from collision keeping the time step lower than the mean collision time. A computational domain is divided into mesh cells and collisions are restricted to these cells. The collisions within a cell are obtained from a probabilistic selection of molecules to participate in such occurrences. A simulated molecule, i.e., an equivalent parcel is representative of  $n$  real molecules. The error accumulated from using such parcels is inversely proportional to the number of simulated molecules, i.e., the higher the number of parcels, the lower the error. The computational time is proportional to the number of simulated molecules. This approach further led to the development of collision models such as Variable Hard Sphere (VHS) model for molecules in 1981 which overcame the problems of its predecessor elastic models. This gave way to developing even more complex molecular models such as Generalised Hard Sphere (GHS) or Variable Soft Sphere (VSS). Based on these models, the parcels are further assigned a post-collision velocity. The macroscopic properties of the gas are calculated in different ways: either individually calculated macroscopic properties for each gas species or an ensemble average. The properties are collected from the position, velocity and energy information retained in the parcels. The Navier Stokes equations become invalid when the density of the dilute gas gets reduced and the statistical fluctuations in the gas become more significant. The degree of rarefaction of a gas can be defined in terms of Knudsen number, which is the gas' mean free path  $\lambda$  divided by the geometries characteristic length.

$$\text{Kn} = \lambda/l, \quad (2.1)$$

where  $\lambda = 1/(\pi d^2 \rho)$  is given by the volume of interaction  $\pi d^2$  and the number density of molecules  $\rho$ . The value of  $l$  is chosen to be in the same scale of local microscopic gradients. When  $\text{Kn} \ll 0.1$ , the gas is in a continuous flow and the

macroscopic properties can be obtained from average molecular properties. Navier-Stokes equations are valid in this region. Conversely,  $Kn \gg 10$  defines free molecular regime where inter-molecular properties can be neglected as the distance between molecules increases. The intermediate range of Knudsen numbers from 0.1 to 10 is known as the transitional regime or rarefied gas regime. The molecular collisions with the wall along with the intermolecular collisions contribute to the determination of gas flow properties. The conservation equations do not form a closed set of equations and are replaced by the Boltzmann equation.

## 2.1 Equations of Fluid Dynamics

Fluid is a continuous medium. Fluid dynamics is to describe a fluid at any instant. The universal way of handling the description is to apply Newton's law to each finite volume element. Fluid dynamics is based on the continuity equation, the motion equation and the energy balance equation. This provides a macroscopic model of fluid mechanics, giving velocity and temperature fields in the fluid domain. When the fluid is ideal (the viscosity and heat effects can be ignored), Euler's equations of state are used. When viscosity and thermal conductivity are included, Navier-Stokes equation of motion fit better. This is the most popular system of equations applied to real fluids. One major drawback of this model is that it is purely phenomenological and unrelated to microscopic data. However, this model is irrelevant to gases and plasma where the molecular interactions become more influential. The transport coefficients and temperatures are defined in terms of collisions between the gas molecules. The kinetic theory, instead, defines the fluid with number density or distribution function. The Boltzmann equation is a representation of the statistical behaviour of a dynamic system. It describes how the velocity distribution changes upon external forces and collisions. In the simplest of terms, the Boltzmann equation can be written as

$$\frac{\partial f}{\partial t} + \frac{p}{m} \cdot \nabla f + F \cdot \frac{\partial f}{\partial p} = \left( \frac{\partial f}{\partial t} \right)_{\text{coll}}, \quad (2.2)$$

where  $f$  is the probability density function;  $f(r, p, t)$ , a function of the position, momentum and time,  $F$  is the external force field acting on the gas particles,  $m$  is the mass of the particles and  $p$  is the momentum [67]. The collision term is the hardest to determine as it is statistical in nature. The Boltzmann equation has coupled transport and collision making it a difficult equation to achieve a closed-form solution for. DSMC decouples these two processes by making the time step less than the mean collision time. To simplify things, only binary collisions are considered in DSMC. However, the collision theory behind the DSMC theorem considers the

contribution of all the molecules in the neighbourhood to calculate the number of collision pairs.

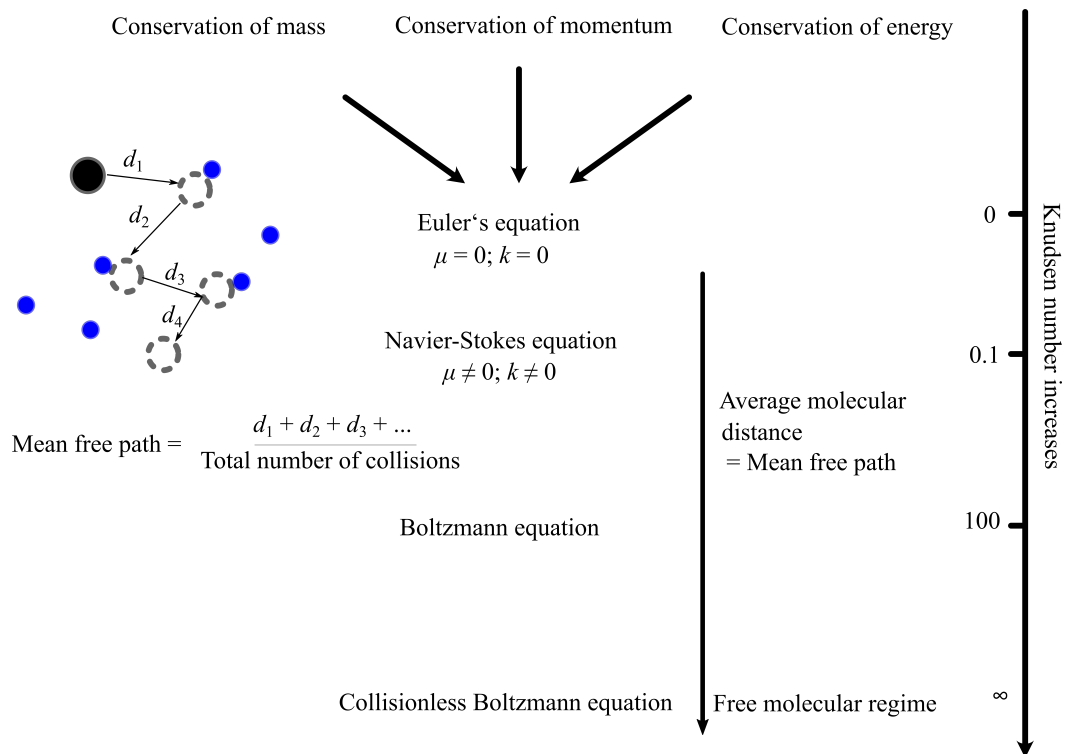


**Fig. 2.1.:** Equations of fluid mechanics. The Euler equation and Navier-Stokes equation are derived from the three conservation laws where viscosity is denoted by  $\mu$  and thermal conductivity by  $k$ . Mean free path is calculated by averaging the maximum distance travelled between collisions.

## 2.2 Inflow

A constant concentration ratio of the two reactant gases is maintained in the simulation domain by constant inlet of the gases in a fixed mole fraction ratio (at ambient pressure,  $p$  and user-defined temperature,  $T$ ) at every time step.

$$\rho_{\text{inflow}} = \frac{p \cdot V_{\text{total}}}{n R_g T}, \quad (2.3)$$

where  $V_{\text{total}}$  is the volume of the simulation domain and  $R_g$  is the universal gas constant. In the DSMC method, each simulated molecule represents  $n$  molecules. The inlet velocity is picked at random from a Maxwell-Boltzmann distribution,

$$u_{\text{inlet}} = \sqrt{\frac{kT_{\text{face}}}{m}} \cdot R_G \cdot \hat{x} \quad (2.4)$$

where  $T_{\text{face}}$  is the temperature of the inlet face,  $R_G$  is a random number from a Gaussian distribution and  $\hat{x}$  is the normal unit vector such that the molecule is directed into the domain.

## 2.3 Elastic Collisions in DSMC

Collisions between two molecules are considered to be elastic, i.e., complete momentum and energy conservation. As collisions occur at very small distances, the most significant force between is the force of repulsion also known as the inverse power law model. The scattering distribution after collision from two spherically symmetrical molecules is determined by two impact parameters,  $d_{\text{app}}$  and  $\epsilon$ . The distance of closest approach of the two molecules from a reference plane at an angle  $\epsilon$  to the collision plane is given by  $d_{\text{app}}$ . The closer this distance, the greater the interaction. An effective cross-section of the two colliding partners is obtained by defining these impact parameters to produce the required realistic scattering law. The total collision cross-section is

$$A_{\text{coll}} = 2\pi \int_0^\pi \sigma \sin \chi d\chi, \quad (2.5)$$

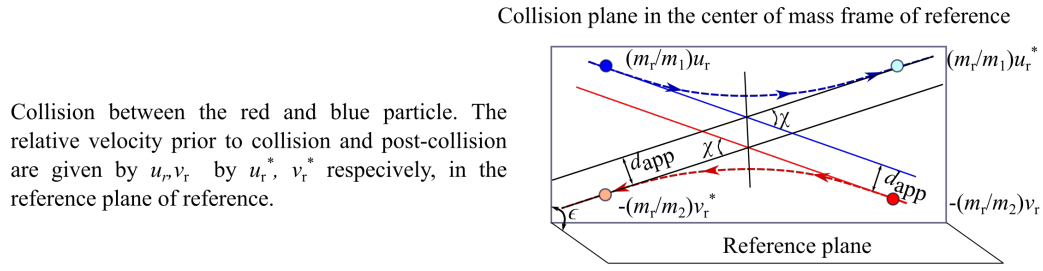
where  $\sigma$  is the cross-section and  $\chi$  is the deflection angle of the colliding molecules [67]. The transport properties in DSMC are dependent on the calculation of the diameter and hence, the total collision cross-section. Along with the total cross-section, the other two cross-section that are important in the transport theory are the viscosity cross-section  $A_\mu$  and momentum cross-section  $A_M$ ,

$$A_\mu = 2\pi \int_0^\pi \sin^3 \chi A_{\text{coll}} d\chi \quad (2.6)$$

$$A_M = 2\pi \int_0^\pi \sin \chi (1 - \cos \chi) A_{\text{coll}} d\chi \quad (2.7)$$

Throughout the years, many models have been developed to achieve realistic collision between two molecules (figure 2.2). The model used in this thesis is the Variable Soft Sphere model developed by Koura and Matsumoto [90] (more details about the

calculation of diameter and collision angle given in appendix). The other models developed for calculating collision cross-sections throughout the years are explained in the ref. [67].



|  | Collision Model      | $d$                           | $\chi$                             | $A_T$     | $A_\mu$                                    | $A_M$                      |
|--|----------------------|-------------------------------|------------------------------------|-----------|--|----------------------------|
| Inverse power law<br>$F = \kappa/r^\eta$ | Hard Sphere          | $(d_1 + d_2)^{0.5}$           | $2\cos^{-1}(d_{app}/d)$            | $\pi d^2$ | $(2/3)A_T$                                 | $A_T$                      |
|  | Variable Hard Sphere | $d_{ref} (u_{r,ref}/u_r)^\nu$ | $2\cos^{-1}(d_{app}/d)$            | $\pi d^2$ | $(2/3)A_T$                                 | $A_T$                      |
|  | Variable Soft Sphere | $d_{ref} (u_{r,ref}/u_r)^\nu$ | $2\cos^{-1}(d_{app}/d)^{1/\alpha}$ | $\pi d^2$ | $\frac{4\alpha}{(\alpha+1)(\alpha+2)} A_T$ | $\frac{2}{(\alpha+1)} A_T$ |

**Fig. 2.2.:** Binary collision in the center of mass frame of reference. The closest distance of approach between two molecules is  $d_{app}$ , the angle of deflection between the two colliding molecules is  $\chi$  and  $u_r$  is the relative velocity of the colliding partners. The angle between the colliding plane and the reference plane is  $\epsilon$ . The three collision models are derived based on inverse power law. The diameters of the colliding spheres are given by  $d_1$  and  $d_2$ , subscript  $_{ref}$  refers to reference values,  $\nu$  is a simple inverse law exponent,  $\alpha$  is the temperature exponent of viscosity coefficient. The value of  $\alpha$  generally lies in between 1 and 2. The three collision cross-sections are:  $A_T$ , total collision cross-section area,  $A_\mu$ , viscosity cross-section and  $A_M$ , momentum cross-section. [67, 90, 91]

### 2.3.1 Collision Sampling

Intermolecular collisions in dilute gas mainly consist of binary collisions. The DSMC algorithm excels at conserving the collision rates in gases. In the simulations, the collisions are elastic, that is, momentum is conserved pre- and post-collision. Collisions between parcels  $i$  and  $j$  may occur if both are located inside one cell independent of their exact location based on the collision probability calculated by

NTC (no-time-counter) scheme proposed by Bird ([67], page 219). Based on this rule, the collision probability is calculated for a set of

$$\frac{1}{2} N_C \overline{N_C} (n A_{\text{coll}} u_r)_{\text{max}} \cdot \Delta t / V_C \quad (2.8)$$

where  $N_C$  is the number of parcels in the cell,  $n$  is the parcel size, and  $V_C$  is the volume of the cell. Since  $n$  is a fixed size, equation 2.3.1 can be rewritten as,

$$\frac{1}{2} N_C \overline{N_C} n (A_{\text{coll}} u_r)_{\text{max}} \cdot \Delta t / V_C.$$

The probability of collision is calculated by

$$p_{\text{coll}} = \frac{A_{\text{coll}} u_r}{(A_{\text{coll}} u_r)_{\text{max}}}. \quad (2.9)$$

The right hand side term is the volume swept by the two colliding molecules during a time step  $\Delta t$  divided by the maximum value of  $(A_{\text{coll}} u_r)$  possible in the cell where  $A_{\text{coll}}$  is the cross-section area, and  $u_r$  is the relative velocity of the parcels in the cell. The advantages of the NTC scheme are that it allows prior selection of collision partners and avoids time penalty, successfully de-coupling the collision from movement [67].

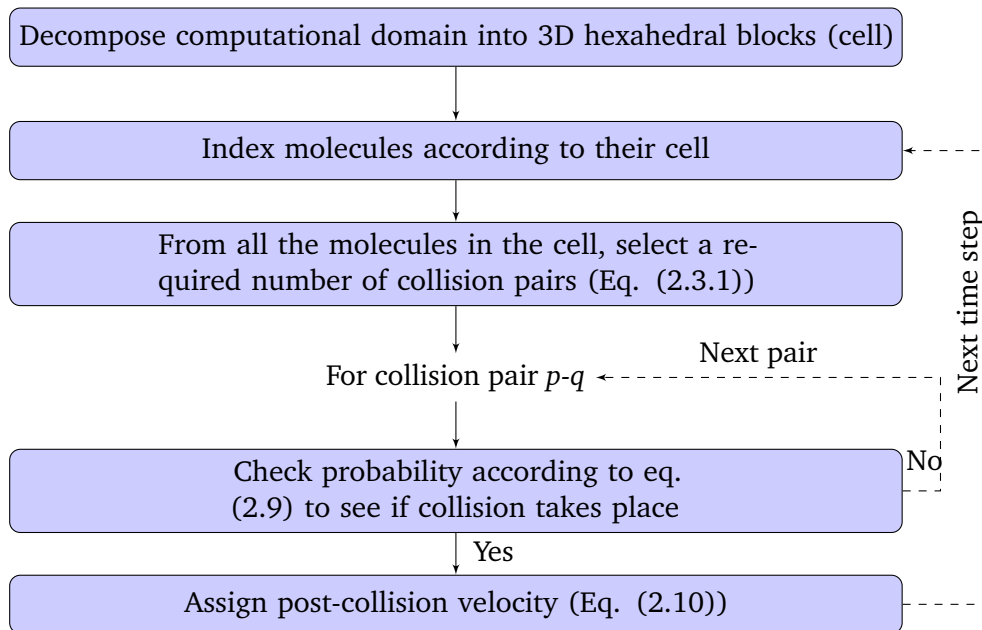


**Fig. 2.3.:** Collision algorithm followed in a typical DSMC simulation.

### 2.3.2 Post-collisional Velocities

The model for choosing the collision cross-section is independent of the scattering law. Based on momentum and energy conservation, the post-collision velocities after an elastic collision as derived by Bird ([67], equation 2.22, page 36) are

$$\begin{aligned} \mathbf{v}_{\mathbf{p}}^2 = & (\cos \chi u_x + \sin \chi \sin \epsilon (u_y^2 + u_z^2)^{0.5})^2 \hat{x} \\ & + (\cos \chi u_y + \sin \chi (u_r u_z \cos \epsilon - u_x u_y \sin \epsilon) / (u_y^2 + u_z^2)^{0.5})^2 \hat{y} \\ & + (\cos \chi u_z - \sin \chi (u_r u_y \cos \epsilon - u_x u_z \sin \epsilon) / (u_y^2 + u_z^2)^{0.5})^2 \hat{z} \end{aligned} \quad (2.10)$$

where  $u_x, u_y, u_z$  are the magnitudes of the relative velocity in  $x, y, z$  direction and  $u_r$  is the magnitude of relative velocity. In case of a collision with a “wall”, parcels may undergo specular or diffuse reflection depending on the degree of thermal accommodation. In specular reflection, parcels undergo direct elastic collision with the wall where the tangential velocity is unchanged and the perpendicular velocity is specularly reflected off the wall,

$$v_{\text{normal}} = -2 \cdot u_{\text{normal}}. \quad (2.11)$$

In diffuse reflection, only a fraction of the incident energy is returned to the reflected molecules. This fraction is often termed as thermal accommodation coefficient,  $\alpha$ , ranging from 0 to 1.

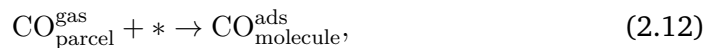
## 2.4 Surface Chemical Reactions in DSMC

Palharini et al. in conjunction with Scanlon et al. developed the freeware dsmcFOAM on the open source computational toolbox OpenFOAM, implementing Bird’s algorithm on a widely available and used network [92, 93]. This framework of DSMC has been modified for various applications. Dreyer et al. showed multi-component diffusion in simulated porous structure using DSMC and derived diffusion coefficients comparable to literature values [77]. Drawing on these results, Pesch et al. modified the DSMC code to include surface chemical reaction as an initiative to gain further insight into the mesoscopic processes occurring in heterogeneous catalyst [78]. They added a Kisliuk precursor based adsorption model, a Polanyi-Wigner based desorption model and Langmuir-Hinshelwood mechanism based reaction model to the diffusion study of Dreyer to study CO oxidation on mesoporous Pd substrate. The sticking coefficients for the reactant gases, CO and O<sub>2</sub> was calculated at different temperatures and surface coverage [94, 95]. Similarly, the pre-exponential factor

for Polanyi-Wigner desorption kinetics was derived from experimental temperature programmed desorption studies [78, 96]. The parameters for the reaction kinetics were derived from multiple works [2, 3, 13, 14, 35]. The general assumption behind the model is a mean-field approximation. The surface is assumed to be uniformly covered with the adsorbed molecules and defects, formation of islands, edges are neglected for simplification purposes. The work of Pesch et al. serves as the basis of this thesis. The schematic of the extended DSMC model can be seen in figure 2.4. The work in this thesis is based specifically on CO oxidation on Pd but it can be generalised to other surface reactions. First, the adsorption, desorption and reaction model and the parameters are discussed in details.

### 2.4.1 Adsorption

The surface mechanisms for adsorption written for single molecules were implemented by Pesch et al. [78]. A molecule colliding with the wall can adsorb on the surface depending on the sticking coefficient of the surface. As the surface coverage increases, the sticking coefficient reduces and thus the probability of further adsorption of molecules decreases. After all the molecules are adsorbed, the molecules are subsequently deleted from the gas composition. CO is molecularly adsorbed on the surface ( $\Delta E_{\text{CO}_{\text{ads}}} = 142.2 \text{ kJ/mol}$ ) while O<sub>2</sub> is dissociatively adsorbed on the surface ( $\Delta E_{\text{O}_{\text{ads}}} = 230.12 \text{ kJ/mol}$ ) [4]. So, CO needs one vacant site (\*) for adsorption and O<sub>2</sub> two nearby vacant sites for adsorption.



where \* denotes a vacant site. The adsorption energy of CO<sub>2</sub> is small [4]; CO<sub>2</sub> adsorption is neglected in the simulation.

Kisliuk from Bell Telephone Laboratories Inc. proposed a model for adsorption of monoatomic and diatomic gases on surfaces under the assumption that every molecule that is impinging on a surface is physisorbed independent of the surface atom configurations. Dependent on the sticking probability  $S$ , these physisorbed molecules may be chemisorbed on the surface. The sticking probability is reduced with increasing coverage and temperature. The probability of a molecule chemisorbing next to an empty site is higher than a filled site which explains the first conclusion. The latter can be explained by the non-negligible rate of desorption compared to the rate of chemisorption at higher temperature. The sticking probability is thus derived from the sum of probabilities of chemisorption on the visited sites preceding

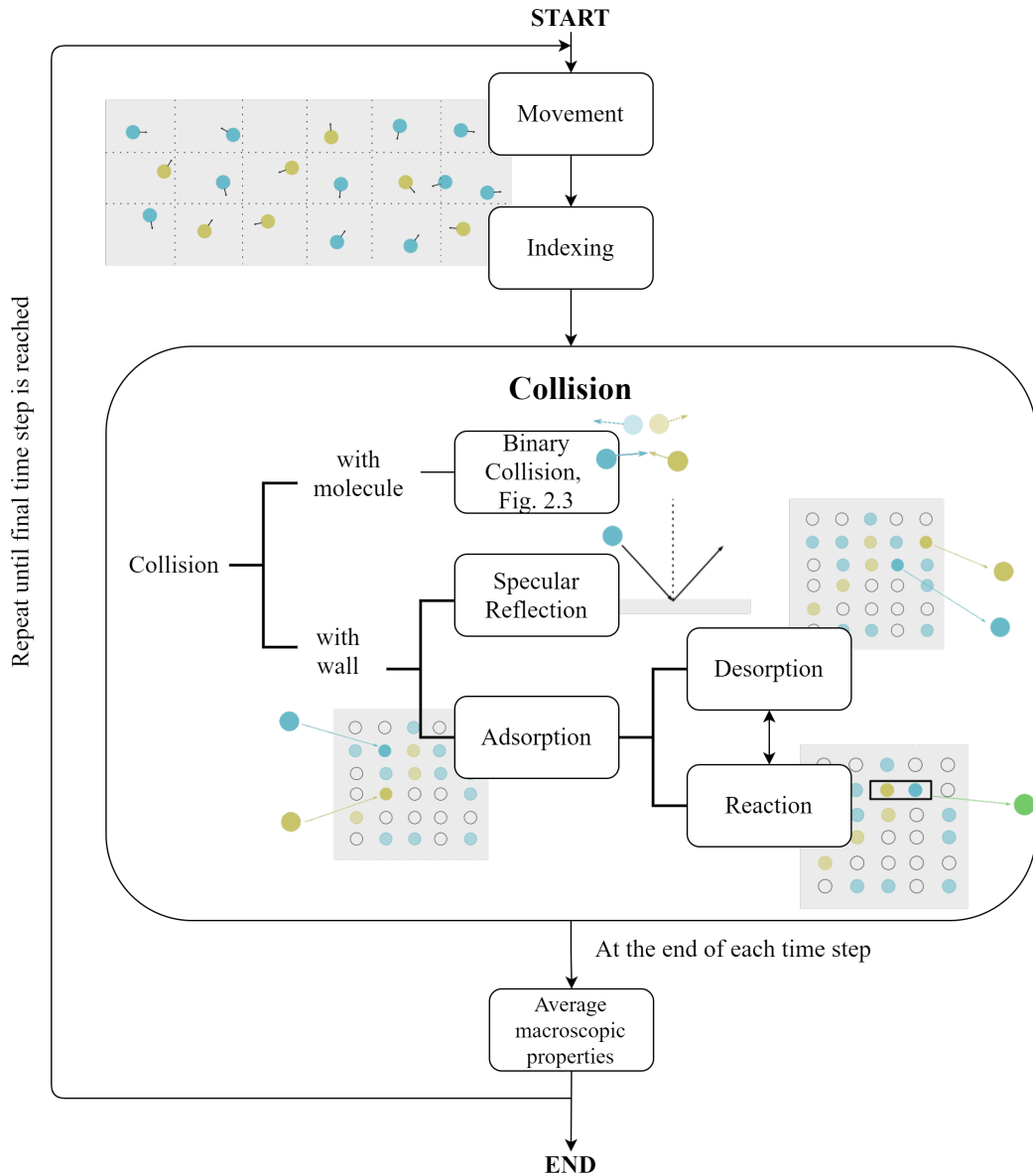


Fig. 2.4.: Schematic of the DSMC algorithm used to simulate surface reaction [78].

the present site of chemisorption. It shows a first order dependence on coverage for CO and a second order dependence for O<sub>2</sub>. In this work the sticking coefficient,  $S$ , is derived from the Kisliuk precursor mediated adsorption model [94, 95].

$$S = S_0(1 + K(1/\theta_{\text{req}} - 1)), \quad (2.14)$$

$$\theta_{\text{req,CO}} = \frac{\theta_{\text{sat,CO}} - \theta_{\text{CO}}}{\theta_{\text{sat,CO}}}, \quad (2.15)$$

$$\theta_{\text{req,O}} = \left( 1 - \frac{\theta_{\text{O}}}{\theta_{\text{sat,O}}} - \frac{\theta_{\text{CO}}}{\theta_{\text{sat,CO}}} \right)^2, \quad (2.16)$$

The coverage is defined as the ratio of the number of adsorbed molecules and the number of surface atoms,

$$\theta = \frac{\sigma_{\text{ads}}}{\sigma_{\text{surface}}}. \quad (2.17)$$

The pre-factor  $K$  is the probability of molecule to be chemisorbed or desorbed on an empty(\*) or a filled site(<sup>occupied</sup>) from a precursor state.

$$K = \frac{p_{\text{des}}^{\text{occupied}}}{p_{\text{des}}^* + p_{\text{ads}}^*}. \quad (2.18)$$

The variable  $\theta_{\text{req}}$  is the probability to find the required number of vacant surface sites,  $\theta_{\text{max}}$  is the maximum surface coverage from literature. In this work, a value of 1/3 for CO and 1/4 for O<sub>2</sub> was chosen from the molecular beam experiments [2]. Physically, there is competitive adsorption of CO and O<sub>2</sub> on the free surface sites (\*). For a surface covered by CO first, beyond a coverage of 0.33, O adsorption is completely inhibited. Whereas if the surface is covered by O ( $\theta = \theta_{\text{max}}$ ), even at maximum O coverage, CO can adsorb on the surface until  $\theta_{\text{CO}} = \theta_{\text{O}} = 0.5$ . The initial sticking coefficient  $S_0$  and the prefactor  $K$  are fitted to experimental data from  $S(\theta)$  curves by Engel and Ertl [2]. For CO,  $S_0$  and  $K$  values are determined as 1 and 0.15 while temperature dependent  $S_0$  and  $K$  values for O<sub>2</sub> can be found in Pesch's paper [78]. At every time step, for every parcel that reaches the catalyst surface,  $S(\theta)$  is first compared to a random number  $R$ . Any molecule of the parcel adsorbs if  $S(\theta) > R$ . The subsequent molecules' adsorption is then dependent on the recalculated sticking coefficient and coverage values. After the adsorption of the molecules, the algorithm loops through all faces and calculates for every molecules desorption and reaction probabilities.

## 2.4.2 Reaction

CO oxidation on Pd(111) surface follows the Langmuir-Hinshelwood mechanism [97] exclusively. CO oxidation occurs if adsorbed CO and O are present adjacent to each other. As the surface is considered as a mean field, the presence of one CO and O atom on a surface is sufficient condition for the possibility of a reaction.



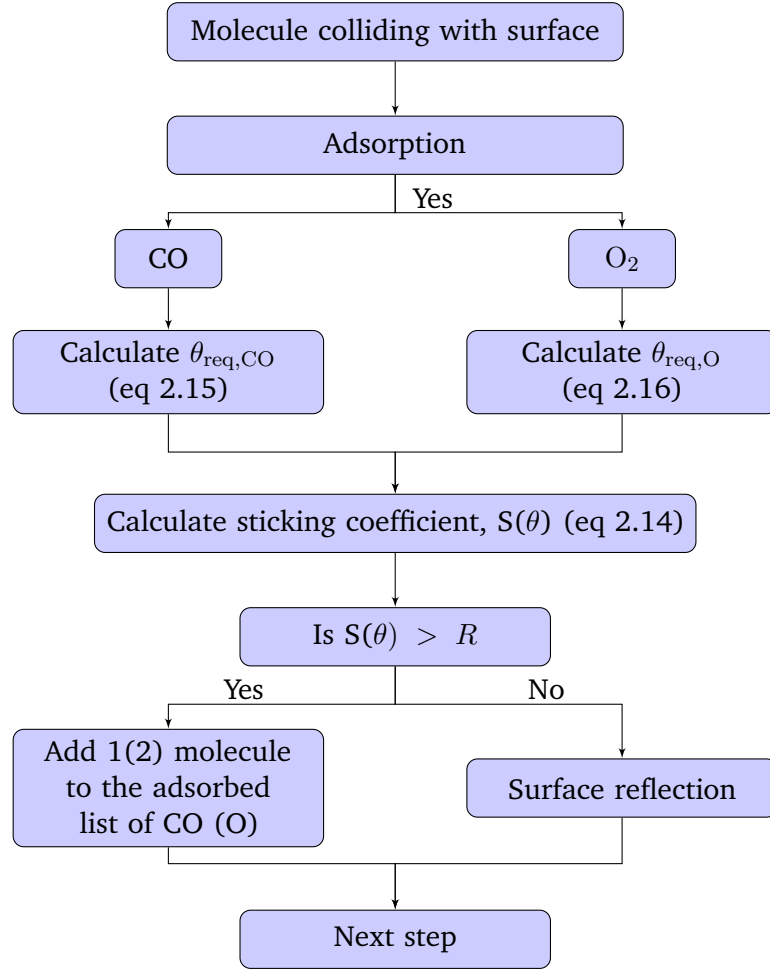


**Fig. 2.5.:** Adsorption algorithm developed by Pesch et al. [78].

The reaction frees up two occupied sites in the process.  $\text{CO}_2$  formed is immediately desorbed as it is weakly bound to the surface and has little surface lifetime beyond 100 K [96]. The Langmuir Hinshelwood reaction rate for  $\text{CO}_2$  formation is given by an Arrhenius-type equation

$$r_{\text{CO}_2} = \nu_{\text{LH}} N_{\text{adsCO}} N_{\text{adsO}} \exp\left(-\frac{E_{\text{LH}}}{R_g T}\right) / A_f^2, \quad (2.20)$$

where pre-exponential factor,  $\nu_{\text{LH}} = 2.5 \times 10^{-3} \text{cm}^2 \text{s}^{-1}$ , activation energy  $E_{\text{LH}} = 83.68 \text{kJ/mol}$ ,  $R_g$  is the universal gas constant,  $T$  is the temperature of the patch and  $A_f$  is the area of the patch, and the number of adsorbed molecules of both the gas molecules [35, 98]. The reaction probability is calculated by

$$p_{\text{reac}} = r_{\text{CO}_2} \cdot \frac{\Delta t A_f}{N_{\text{adsCO}}}. \quad (2.21)$$

CO<sub>2</sub> which desorbs instantaneously from the gas surface [96] is added to the gas phase composition. The participating adsorbed CO and O are removed from the adsorbed molecules list. The position and velocity vector of the desorbed molecule is decided according to Maxwellian distribution.

### 2.4.3 Desorption

Guo et al. performed temperature programmed desorption studies of CO and O<sub>2</sub> from the Pd(111) surface and modelled the desorption mechanism according to the Polanyi-Wigner equation [15, 32, 96],

$$r_{\text{des}} = \nu_{\text{des}} \theta^d \exp\left(\frac{-E_{\text{des}}}{R_g T}\right), \quad (2.22)$$

where rate of desorption is  $r_{\text{des}}$ , desorption activation energy  $E_{\text{des}}$  at an absolute temperature  $T$ , the pre-exponential factor,  $\nu_{\text{des}}$  and the desorption order,  $d$ , which is 1 for the molecular desorption of CO and 2 for the associative desorption of O<sub>2</sub>. The values of  $E_{\text{des}}$  and  $\nu_{\text{des}}$  for CO and O<sub>2</sub> are taken from ref. [15] and [32] respectively. The pre-exponential factor varies often in orders of magnitude for different coverage of CO and is independent of coverage for O<sub>2</sub> fitted with parameters  $a$  and  $b$ .

$$\nu_{\text{des}}(\theta) = 10^{a+b\theta} \quad (2.23)$$

From the comparison of experiments from Guo and desorption simulations by Pesch et al. [78], the values of  $a$  and  $b$  were found to be 16.0 and -15.0 for CO and -1.7 and 0.0 for O<sub>2</sub>. The coverage ( $\theta$ ) dependent activation energy is expressed as

$$E_{\text{des}}(\theta) = E_{\text{des}}(0) + W \cdot \theta \quad (2.24)$$

with  $W$  is the energy term describing lateral molecular interactions (either weakening or intensifying of the adsorption bonds),  $\omega_{\text{pair}}$  is the interaction potential between the nearest neighbours,  $N_{\text{nn}}$  at maximum coverage,  $\theta_{\text{max}}$ .

$$W \cdot \theta_{\text{max}} = \omega_{\text{pair}} \cdot N_{\text{nn}} \quad (2.25)$$

O<sub>2</sub> has 6 nearest neighbours and interaction potential between the nearest adsorbed molecules is 2.9 kJ/mol at a maximum coverage of 0.25 [15]. This gives  $W = -69.6$  kJ/mol [78]. Similar calculations give the values  $W = -153$  kJ/mol for CO [32, 78] at  $\theta_{\text{max}}=0.6$ . The zero coverage activation energy  $E_{\text{des}}(0) = 222$  and 147

kJ/mol for O<sub>2</sub> and CO respectively are taken from Guo's set of experiments. The probability of the desorption step is

**Tab. 2.1.:** Desorption parameters for CO and O<sub>2</sub> taken from Ref. [15] and [32].

| Molecules      | $E_{\text{des}}$          |          | $\nu_{\text{des}}$ |     |
|----------------|---------------------------|----------|--------------------|-----|
|                | $E_{\text{des},0}$ kJ/mol | W kJ/mol | a                  | b   |
| CO             | 147                       | -153     | 16                 | -15 |
| O <sub>2</sub> | 222                       | -69.6    | -1.7               | 0   |

$$p_{\text{des}} = r_{\text{des}} \cdot \frac{\Delta t A_f}{N_{\text{ads}_{\text{CO}}}} \quad (2.26)$$

A molecule desorbs if  $p_{\text{des}} > R$ . The participating CO and O<sub>2</sub> are removed from the adsorbed molecules list and are added to the gas phase composition. The coverage are updated before moving to the next step. CO<sub>2</sub>, having a short surface lifetime, desorbs immediately from the Pd surface and the desorption mechanism is neglected [2, 4, 96].

#### 2.4.4 Input Parameters

There are several input parameters needed to be given by the user for calculation of the macroscopic properties later. The input parameters consists of temperature, gas phase composition, a mesh that represents the catalyst surface, a reaction mechanism (adsorption, desorption, reaction) and a collision model unique to DSMC simulation. In addition, one can specify the initial adsorbates configuration, the temperature of the catalyst surface and the thermal accommodation of the catalyst surface. In the Appendix, all the parameters are discussed in more details divided by the files that they appear in as discussed in figure 2.6.

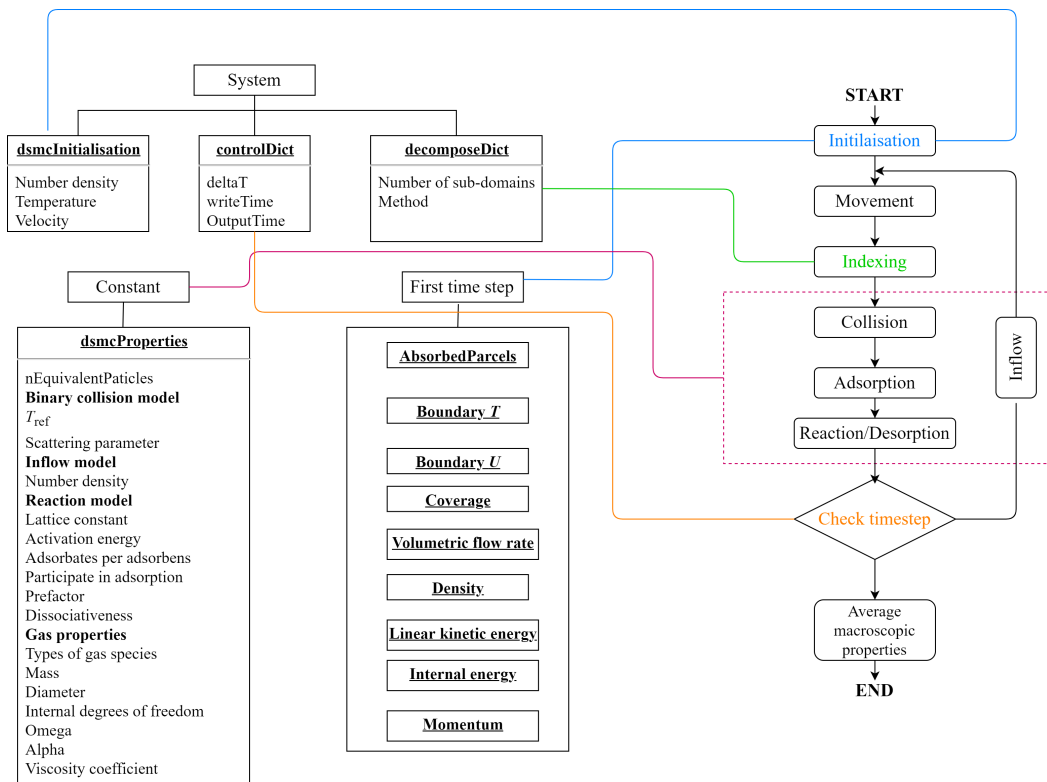


**Fig. 2.6.:** Parameters initialised in the DSMC algorithm. The dotted boxes refer to folders and the solid boxes refer to the files within the case file. Further details about each individual parameters are given in the appendix.

# Methodology

All research is additive, science doesn't work in breakthroughs.

---

*Hank Green*

The original DSMC code was implemented in OpenFOAM by Scanlon et al. in conjunction with Palharini et al. [92, 93]. Dreyer et al. [77] simulated multi-component diffusion in porous structure. The DSMC algorithm [67, 79] was extended by Pesch et al. [78] to simulate heterogeneous catalytic CO oxidation on mesoporous Pd layers. They added the Kisliuk precursor model for molecular adsorption of CO and dissociative adsorption of O<sub>2</sub> [94, 95]. Desorption is modelled according to Polanyi-Wigner Arrhenius-type equation [96]. The rate of CO<sub>2</sub> formation is defined by an Arrhenius equation following Langmuir-Hinshelwood mechanism [99]. The model has a length scale of 1  $\mu\text{m}$  and has a resolution up to few  $\mu\text{s}$ . An important outcome of their work is the transition from kinetic limited to diffusion limited regime as the temperature of the system increases. This is a great step towards understanding the complex mechanisms involved in porous layers. But, DSMC is an extensive program and uses a lot of computational power. In an attempt to study the original code, it is seen that, in particular, a study of 8  $\mu\text{s}$  of dynamical evolution of CO including adsorption, desorption and CO oxidation and molecular collisions needed 650,000s of simulation time on 10 processors of a 12 core Xeon server (2.7 GHz, 40 GB RAM) on OpenFOAM-4.1 DSMC code. Thus, it would require enormous amount of time to simulate even 1 s of the reactor. A variable parcel size has been developed to improve the efficiency of the surface reaction DSMC algorithm.

## 3.1 Simulation Domain

In the figure 3.1, the simulation domain is shown. The domain is divided into hexahedral computational cells. The DSMC computational cell size is chosen such that one molecule remains in the cell for few time steps before moving to a neighbouring cell, generally, less than 1/3rd of the molecular mean free path to remain in the

transition Knudsen regime [68, 70]. Macroscopic properties are under-predicted with larger cell sizes and a proper average is unattainable for smaller cell sizes. There are two phases in the domain, the gaseous phase comprises of the binary collisions and diffusion steps and the solid catalyst surface where surface reflection, adsorption, desorption and reaction takes place. The catalyst surface is then divided into patches and each patch is divided into faces. Separate lists are kept for all molecules adsorbing, desorbing and forming on the surface of each species for better data management which helps in producing highly resolved local properties. The progression of work flow of DSMC in OpenFOAM is as shown in figure 3.2.

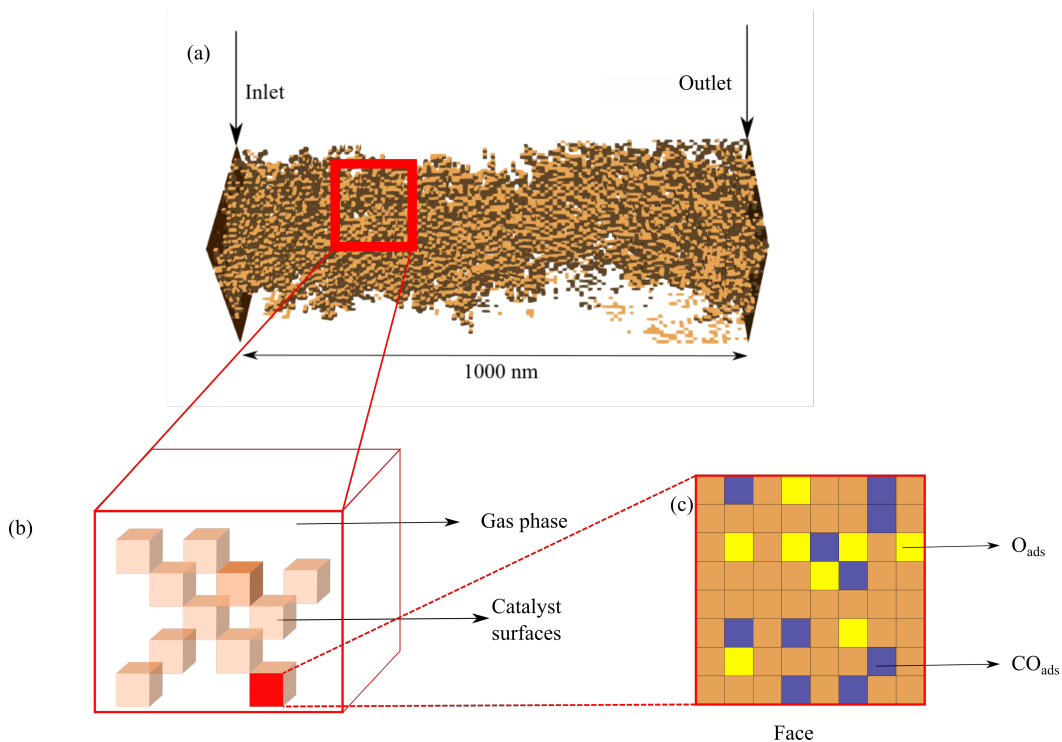


**Fig. 3.1.:** (a) Simulation domain showing the computer-generated porous structure [100]. There is one inlet, one outlet and periodic boundary conditions on the other four sides. Further details on the simulation of the mesoporous layers are given in ref. [77, 100]. (b) A 2D-view of the computational cell consisting of the gas phase and the solid catalyst surface. The catalyst surface is made up of several patches. (c) 2D-view of a patch. The patch is further divided into faces. All steps in the molecule-surface interaction are performed on the faces. A dynamic list of molecules adsorbed, desorbed and formed of each gas species is maintained on each face of each patch of the catalyst surface.

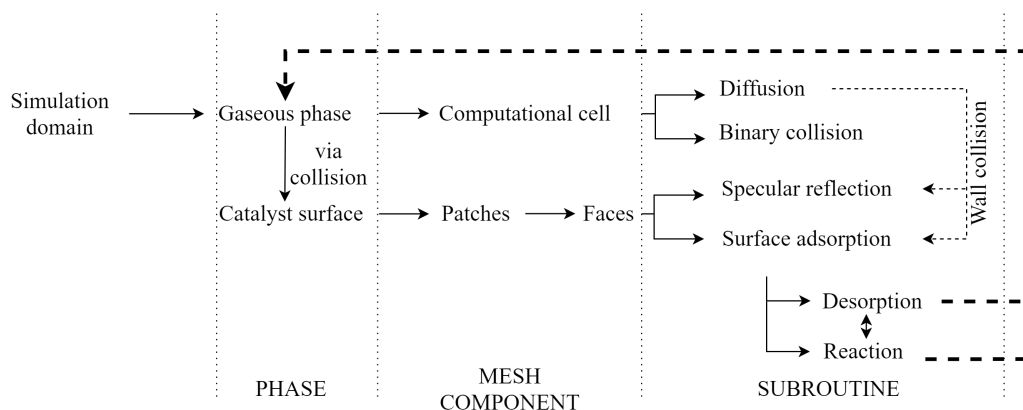


**Fig. 3.2.:** Workflow in a DSMC code. Collision and surface steps are decoupled from one another. Separate lists of data are maintained for the molecules in the gas phase and on the surface.

## 3.2 Variable Parcel Method

As mentioned earlier, the extended model by Pesch et al. is an early attempt to simulate catalytic processes in a reasonable time scale [78]. In the model, each simulated molecule represents one real gas molecule. After simulating movement in a deterministic manner and then collision in a stochastic way [67], molecules would interact with surfaces and adsorb, desorb and react based on individual molecular probabilities. The tracking of the molecules and handling all the separate processes for a mixture of three species makes it computationally expensive. Scanlon et al. in the implementation of DSMC on OpenFOAM have included a property where a group of real molecules could be identified as a parcel and the parcel could be followed during movements and collisions [92, 93]. A macroscopic average of the simulation environment would give physically accurate results. Bird designed DSMC in such a way because the early usage of the algorithm was to study atmospheric re-entry problems where the number of gas molecules could be particularly high under low atmospheric pressures [67]. The deterministic collision model is already modelled to calculate approximately equal number of collisions among parcels as it would be among real molecules. With a large variation in molecular masses, there is a practical problem associated with the collision process. The acceptance rate is then skewed in favour of light molecules with high collision probability,  $(A_{\text{coll}}u_r)_{\text{max}}$  and the selection process would be inefficient. Bird proposed a separation of the gas species to calculate  $((A_{\text{coll}}u_r)_{\text{max}})_{pq}$  for species p and q and the problem associated is the increase in storage of all variables generated increasing squarely with increasing number of species [67]. The selection procedure for variable parcels was modified by Schmidt and Rutland by the inclusion of parcel size in the probability calculation

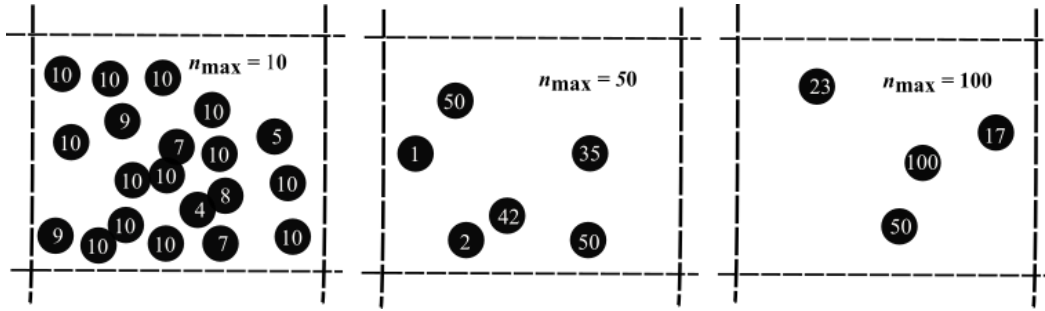


**Fig. 3.3.:** The working of variable parcel method. A simulated molecule is representing a group of molecules. This variable can be fixed by the user during initialisation. The larger the parcel size, lower the number of molecules that are to be tracked which reduces the computational time. Here, the gaseous phase is represented by parcels of variable sizes (parcel size mentioned inside the parcels). For a total of 180 molecules (for example) per computational cell, the distribution of parcels can be seen. The parcel size is limited by the maximum size specified by user. In general, with a larger  $n_{\max}$ , the number of parcels will be lower.

[88]. Nanbu developed a modified collision algorithm for assigning post-collision velocities to gas mixtures in plasma processing that involved electrons, ions and radicals [89]. Both of these modifications have been adopted to make the surface algorithm more robust. The gaseous phase is represented by parcels but of variable sizes rather than fixed sizes. The parcel sizes in case of Variable Parcel method can vary but are limited by  $n_{\max}$ , as shown in figure 3.3.

### 3.2.1 Inflow

The inflow routine remains unchanged. At ambient pressure,  $p$  and user-defined temperature,  $T$ , molecules are packed into parcels of maximum size  $n_{\max}$ ,

$$\rho_{\text{inflow}} = \frac{p \cdot V_{\text{total}}}{R_g T} / n_{\max}.$$

### 3.2.2 Collision Sampling

Schmidt and Rutland suggested a modified collision selection process for the simulation of dense sprays where the parcel size would vary depending on the size of droplet [88]. As the size remains constant in the simulation, the weight of the parcel is determined by the number of molecules a parcel represents. The total number of collision pairs selected per time step is given by equation 2.3.1, however, the scaling

fraction now consists of  $n_{\max}$  instead of  $n$ ,  $n_{\max}$  being the maximum parcel size in the cell.

$$N_{\text{sel}} = \frac{1}{2} N_C \overline{N_C} n_{\max} (A_{\text{coll}} u_r)_{\max} \Delta t / V_C \quad (3.1)$$

The collision probability of the selected pairs follows equation 2.9. The maximum value of probability is set as  $(n A_{\text{coll}} u_r)_{\max}$  per cell and automatically replaced by a larger value if encountered during the simulation. The probability of collision is then defined as,

$$p_{\text{coll}} = \frac{n A_{\text{coll}} u_r}{n_{\max} (A_{\text{coll}} u_r)_{\max}} \quad (3.2)$$

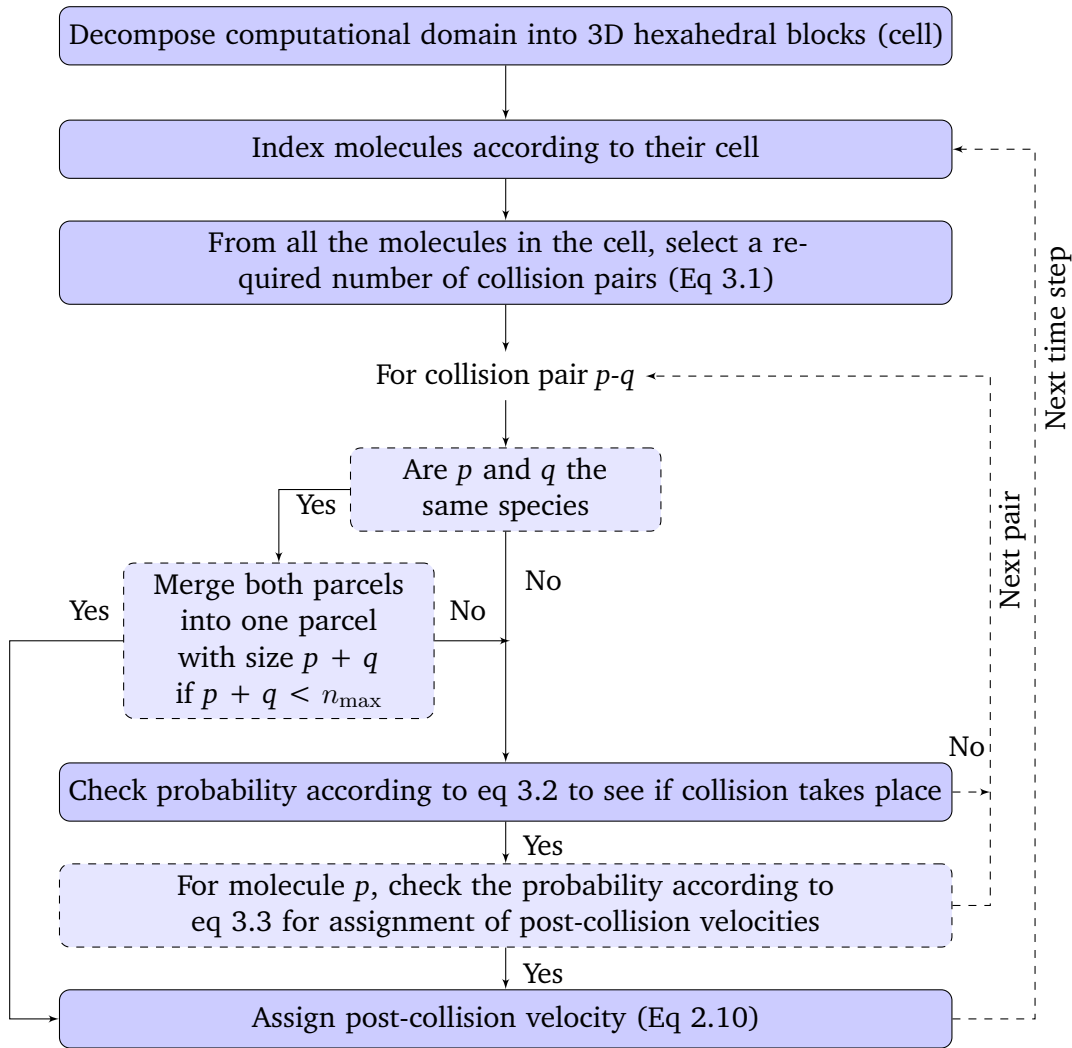
However, post collision velocities given by equation 2.10 are modified for molecules is they satisfy the following condition,

$$\frac{n_q}{\max(n_p, n_q)} > R \quad (3.3)$$

where  $n_p$  is the size of the parcel whose velocity is to be modified and  $n_q$  is the collision partner parcel size. This additional condition signifies that a lighter molecule (in this case lower parcel size) will definitely have a post-collision velocity while there is a chance that the velocity of the larger molecule will remain unchanged. Physical collision between the two parcels ( $n_p < n_q$ ) is improbable as collision is binary. So, the larger parcel, representing  $n_q$  number of molecules would be colliding with a reduced probability of  $p_{\text{coll}} \cdot n_p / n_q$  while the smaller parcel collides with a probability of  $p_{\text{coll}}$ . The complete collision scheme is shown in figure 3.4.

### 3.2.3 Particle merging

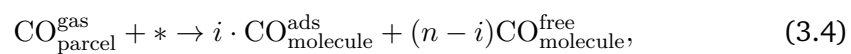
When parcels from the same gas species are selected for collision, additionally the parcels are combined into the maximum parcel size if possible in the attempt to reduce the number of parcels to be tracked. One of the parcels' size is increased to the new parcel size and the post-collision velocity is changed depending on whether the smaller or larger molecule was chosen. The other parcel is removed from the gas phase. It is acknowledged here that particle merging is highly debated as it is impossible to conserve energy and momentum at the same time. However, many-step solutions such as adaptive sampling [101, 102] or joint particle-cell management [103, 104] are proposed to work around this problem. As, macroscopical energy conservation is of low priority in this model, it was neglected for the purposes of this model. It can, of course, be added to the collision module if it is required.

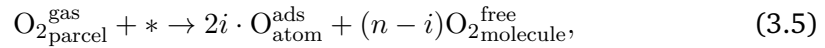


**Fig. 3.4.:** Collision scheme in VP method. The modifications from Pesch et al.'s code are shown in light blue.

### 3.2.4 Adsorption

Parcels that collide with the catalyst surface may adsorb on the surface. It is decided by comparing the sticking probability to a random number. The catalyst surface has been found to show a saturated coverage dependent on the temperature and the gas species adsorbing on the surface. The sticking coefficient of the surface is dependent on the surface coverage as explained in equations 2.14, 2.15 & 2.16. For each parcel that is selected for adsorption, depending on the coverage and sticking coefficient, a fraction of the  $n$  molecules in the parcel would be adsorbed, after removing the parcel from the gas phase.





The vacant sites are represented by \*. The number of molecules that are accepted in this step are represented by  $i$  used in equation 3.4 and 3.5 and  $i$  molecules are added to the adsorbed molecules list. And the  $(n - i)$  molecules are stored in a new free molecules list. The coverage is updated after every molecules' adsorption. So, it is highly unlikely that all molecules of a parcel will be accommodated on the surface if the saturation coverage is reached. Thus, a dummy list, *free molecules list*, is introduced to the existing code where the molecules of the parcel that remain unadsorbed are stored. This list is identified first by the species and then the local face identity. Parcels that are unadsorbed on the surface are automatically added to the free molecules list. These molecules are then re-initialised into the gaseous phase in the re-initialisation step. Adsorption subroutine is shown in figure 3.5.

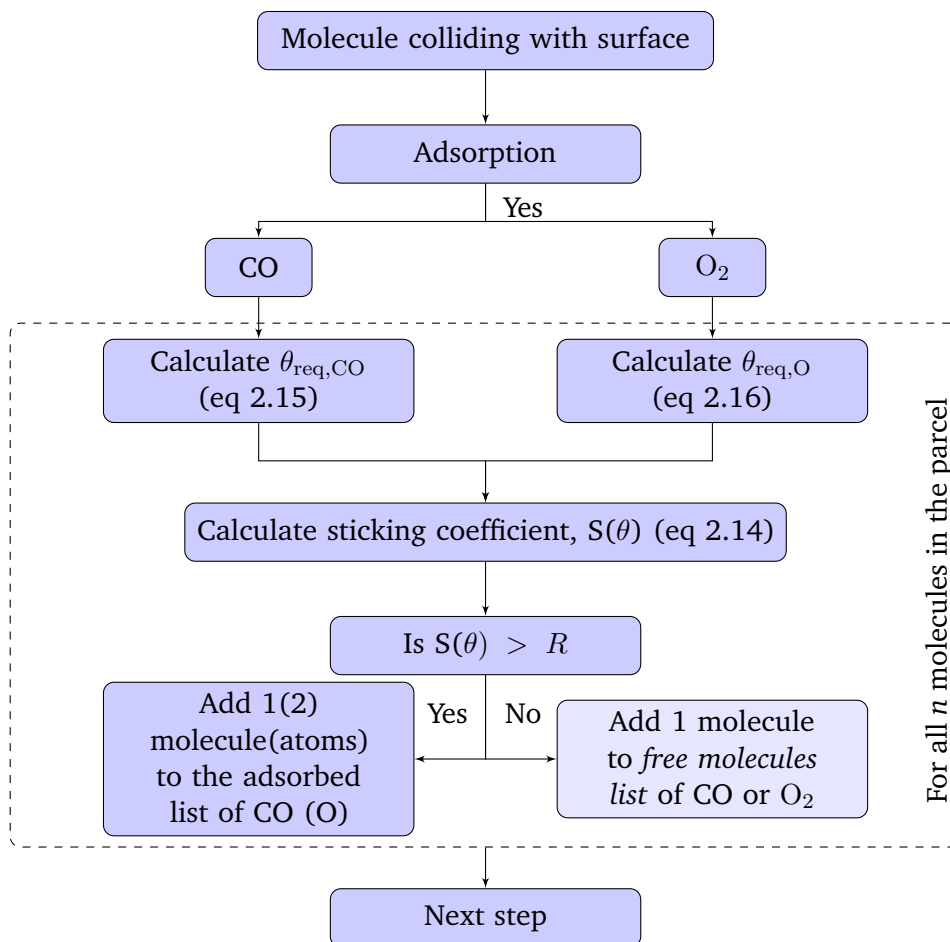


**Fig. 3.5.:** Modified adsorption algorithm accommodating parcels. Each parcel can represent varying number of real molecules. The modification is showed in light blue.

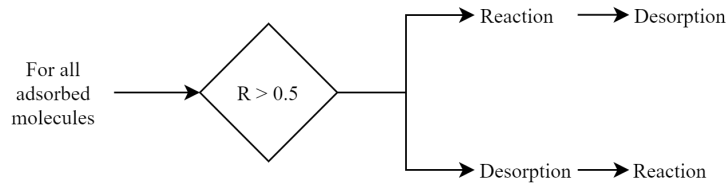


**Fig. 3.6.:** Available pathways for an adsorbed molecule

### 3.2.5 Desorption-Reaction

Once all the molecules are adsorbed on the surface, there are two ways for the simulation to proceed. The molecule can desorb or react depending on the individual desorption or reaction probability given by equation 2.26 and 2.21, respectively.

$$p_{\text{reac}} = r_{\text{CO}_2} \cdot \frac{\Delta t A_f}{N_{\text{adsCO}}}$$

$$p_{\text{reac}} = r_{\text{CO}_2} \cdot \frac{\Delta t A_f}{N_{\text{adsCO}}}$$

As both pathways are equally possible, the reaction or desorption path is chosen at random as shown in figure 3.6. A simple random number generator decides if the adsorbed molecules would react or desorb first. If the reaction path is followed first,  $p_{\text{reac}}$  is compared to a random number for every possible reaction event. If  $p_{\text{reac}} > R$ , the molecule reacts to form the product. After the reaction subroutine is completed for all adsorbed molecules, it proceeds to desorption. Here, when  $p_{\text{des}} > R$ , the molecule desorbs. Same process is followed for desorption first. In case of successful comparisons, the participating molecules are removed from the adsorbed molecules list and are added to the *free molecules list* (see fig. 3.7). Once the loop goes through both desorption and reaction, the next step of the algorithm is started.

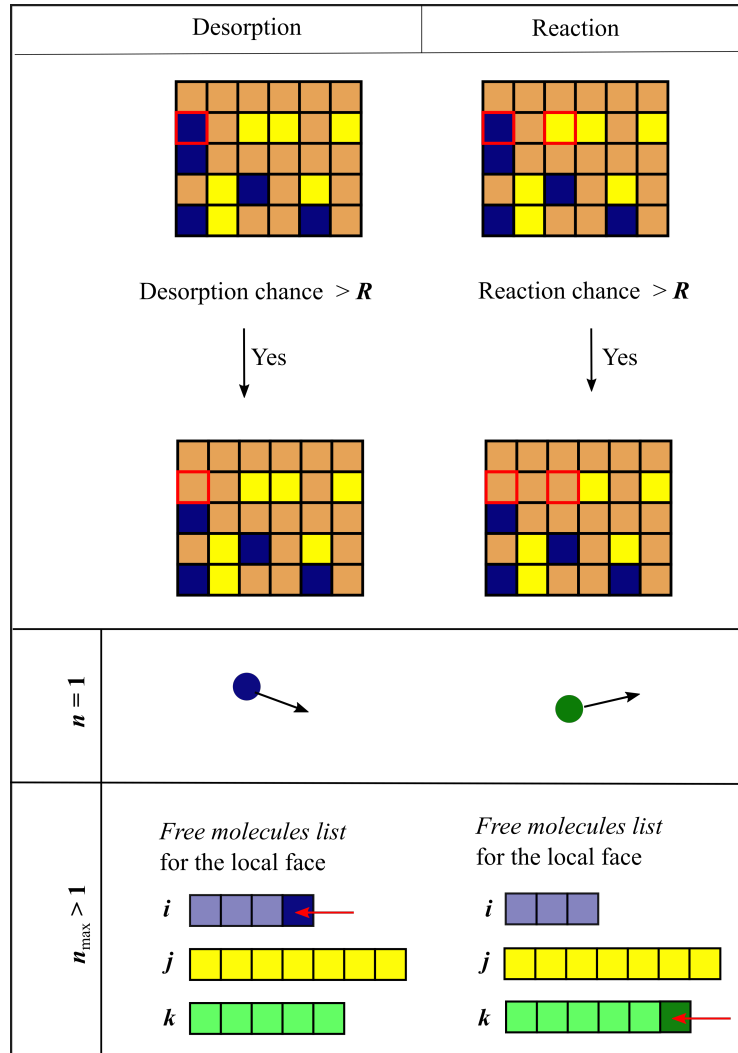


**Fig. 3.7.:** Desorption and Reaction mechanism following adsorption of molecules. When a molecule desorbs from the surface, under the condition that it has sufficient energy to overcome desorption barrier (in case of CO and O<sub>2</sub>) or a product molecule is formed (in this case, CO<sub>2</sub> desorbs instantaneously from the surface). Blue: CO; Yellow: O<sub>2</sub>; Green: CO<sub>2</sub>.  $R$  is a newly generated number uniformly distributed between 0 and 1.

### 3.2.6 Re-initialisation

There are four separate lists maintained for all species of molecules

1. *Adsorption data*

All the molecules that are adsorbed on the catalyst surface are added to a list that handles the number of each type of molecule on a given face on a surface. Molecules are removed from this list when they either react or desorb.

2. *Desorption data*

The rate of desorption on the catalyst surface is added to this list for each face on the surface and the list is made for all species.

3. *Reaction data*

The rate of reaction on the catalyst surface is added to this list.

4. *Free molecules list*

All the molecules that desorb from the catalyst surface, whether molecular desorption of CO or associative desorption of O<sub>2</sub> or instantaneous desorption of CO<sub>2</sub> are added to this list. The gas phase molecules that interact with the surface but unadsorbed are also added to this list. This list contains the number of each type of molecule on a given patch on a surface.

The free molecules list is emptied every time step. The molecules are sorted into the least number of parcels possible. Thus, the molecules are first sorted into groups of  $n_{\max}$  and then the residual molecules are put into one parcel. With increasing  $n_{\max}$ , the number of molecules to be tracked decrease. An example situation is shown in figure 3.8.

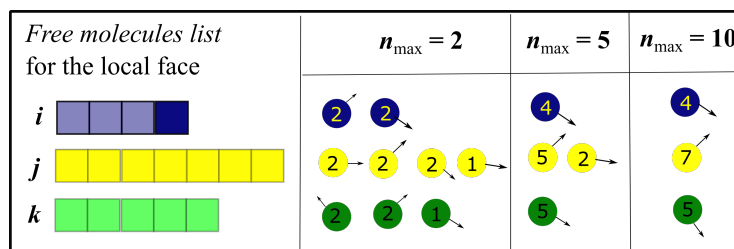


**Fig. 3.8.:** Parcel re-introduction process of gas molecules to parcels in gaseous phase under VP method. All the molecules are packed as efficiently as possible into parcels, regardless of the number of available molecules.

### 3.3 Summary of all modifications from surface reaction model by Pesch et al. [78] in this work

The modifications are all tabulated in table 3.1.

**Tab. 3.1.:** Differences between the DSMC surface algorithm used by Pesch et al. [78] and the Variable Parcel method proposed in this thesis.

| Step  | Pesch et al. [78]  | Variable Parcel Method (this work)  |
|---|--|---|
| Parameters                                  | Equivalent parcel size, $n = 1$ (A simulated molecules represents a real molecule) | Parcel Size, $n_{\max}$ (A simulated molecule can represent any number (between 1 to $n_{\max}$ ) real molecules)   |
| Inflow                                      | $\rho_{\text{inflow}} = \frac{p \cdot V_{\text{total}}}{R_g T}$                    | $\rho_{\text{inflow}} = \frac{p \cdot V_{\text{total}}}{R_g T} / n_{\max}$<br>Each inflow parcel has $n_{\max}$ real molecules  |
| Collision (Post-collision velocity, $v^*$ ) | If two molecules collide, assign $v^*$ to both                                     | If two molecules collide, assign $v^*$ to one (both) molecule which satisfies $n_q / \max(n_p, n_q)$  |
| Adsorption                                  | If molecule adsorbs, update absorbed parcels list, else, add it back to gas phase  | If parcel collides, calculate sticking coefficient and coverage for every molecule that is adsorbed. If the molecule is not adsorbed it is added to <i>free molecule list</i> |
| Desorption, Reaction                        | Molecules desorbed or product formed is directly added to gas phase                | Molecules desorbed or product formed is added to <i>free molecules list</i>   |
| Re-initialisation                           | Not required   | Molecules from the <i>free molecules list</i> are added to gas phase packed in parcels  |

## 3.4 Experimental Validation

The surface reaction model is first validated with experimental data. For this purpose, experimental results are collected from the Physics department of Chalmers University. They have developed an in-house state of the art manufacturing process of chips. The chips consists of parallel microchannels with pure catalyst nanoparticles embedded in the microchannels [105]. The particles were fabricated by electron beam deposition and annealing at 550 °C in Ar. The chip is mounted on a flat ceramic plate and heater with a feedback circuit. This circuit coupled with a thermocouple helps in maintaining the temperature throughout. The inlet gas concentration to the microchannels is controlled by mass-flow controllers. The setup is equipped with a quadrupole mass spectrophotometer (QMS) mounted on an UHV chamber, such that the pressure is of the order of  $10^{-6}$  mbar, to measure the outlet gas concentration. The setup is also equipped generally with dark-field scattering spectroscopy to probe localised surface plasmonic resonance (LSPR) of the particles. Generally, Pd and Pt are very attractive materials as they remain undamaged even in severe conditions and are easily recoverable. However, the noble metals are also poor scatterers of light and it is difficult to obtain accurate in-situ plasmonic resonance used for other metals by the group [106–108]. This setup is described in more detail in the paper by Liu et al. [108].

The schematic of the setup used for the specific oxidation reaction is shown in figure 3.9. Chips are manufactured with embedded Pd nanoparticles. The inlet flow is maintained according to different concentration ratios. The temperature of the chip is maintained at 498 K. There are 40 parallel channels on the chip. Each parallel channel has 18 Pd nanoparticles which are evenly spaced at 5  $\mu\text{m}$ . The channel dimensions are  $100000 \times 100 \times 500 \text{ nm}^3$ . Each individual Pd particle is a cylinder of 100 nm diameter and 40 nm height. The entire surface is assumed to be active. The deposited particles are polycrystalline in nature. Alekseeva et al. have showed grain boundaries for different material produced by the same method [109]. The collective gas concentration is measured at the outlet using a QMS at 10s intervals. The experimental data produced with this setup is used as the prime source of experimental results for comparison with DSMC simulations.

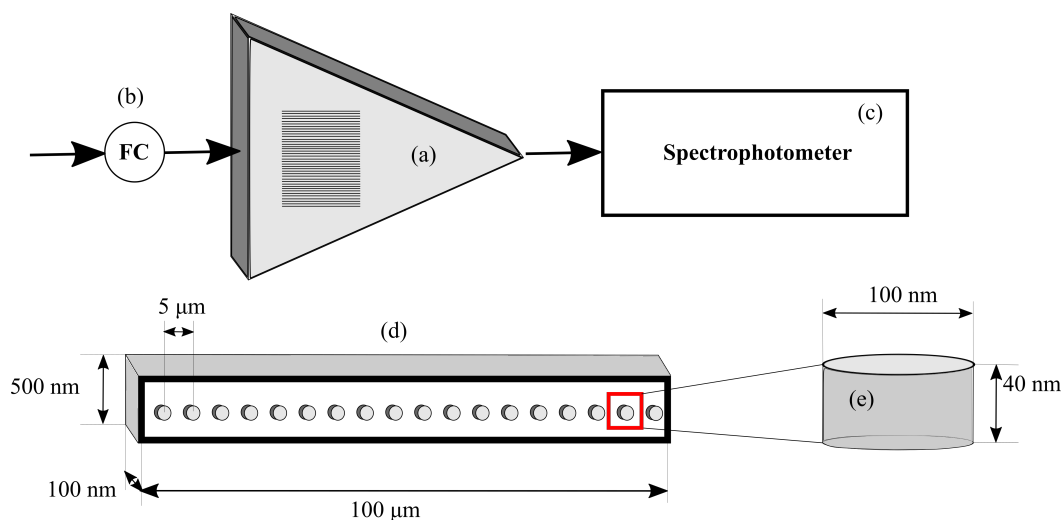


**Fig. 3.9.:** Schematic of the chip manufactured by Physics group at Chalmers [105]. (a) The uniformly heated chip which is a support of the 40 parallel nano-channels. The inlet gas flow is controlled by a (b) flow controller and the outgoing gas is collected and analysed by a (c) spectrophotometer. The (d) nano-channel comprises of 18 Pd cylinders spaced  $5\ \mu\text{m}$  apart. (e) Each cylinder is purely Pd of 100 nm diameter and 40 nm height and the complete surface is active.

It is assumed that the 40 parallel channels will have similar activity. Thus, to save computational time, essentially one entire channel is simulated and  $\text{CO}_2$  just at the boundary is measured. Using the blockMesh mesh generator in OpenFOAM, an empty cuboid mesh with cells of 8 nm cubic dimensions is generated. Then the mesh generation utility SnappyHexMesh is used to setup the cylindrical particles and these are the only active substance in the entire simulation domain. The generated mesh is shown in figure 3.10.

In this setup, the evolution of the reaction is studied with the surface reaction model in DSMC in OpenFOAM. The variable parcel scheme is implemented to improve the computational efficiency of the surface reaction model, as proposed by Pesch et al. [78], as the scale of this simulation is quite high compared to the preceding simulations. The mass flow of each gas species is measured at the inlet and outlet to calculate conversion rate of reactants. The inlet gas comprises of CO,  $\text{O}_2$  and Ar. CO and  $\text{O}_2$  adsorb on the surface. Adsorbed CO and O can react to form  $\text{CO}_2$  or may desorb from the surface depending on the probabilities.

### 3.4.1 Sensitivity Analysis

In this work, the influence of certain input parameters is analysed on the overall  $\text{CO}_2$  production at the outlet. The simulation requires initialisation of a number of

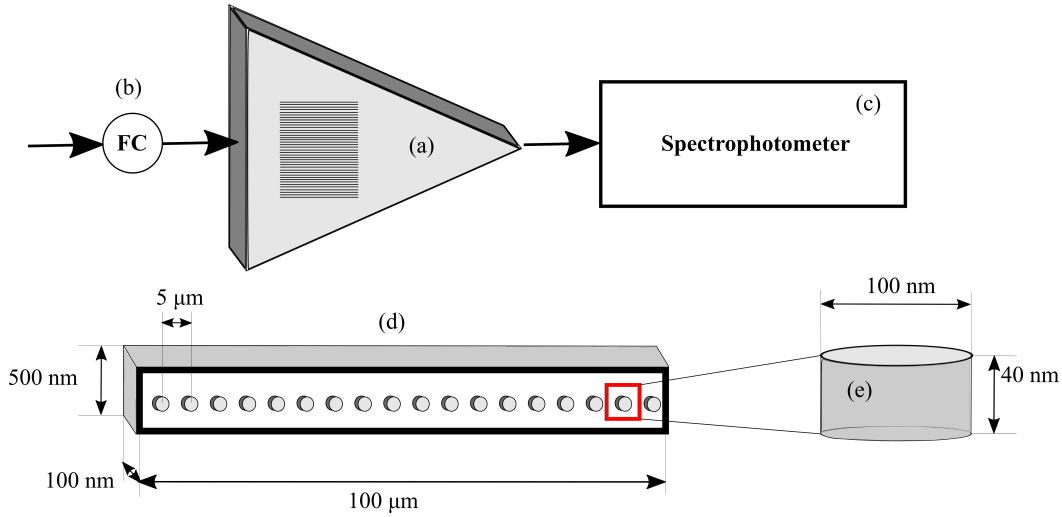


**Fig. 3.10.:** Computational mesh of the setup. Each cell has 8nm cubic dimensions. (a) This shows the yz cross-section of the domain. (b) The cylindrical Pd particle.

parameters. All parameters are listed in the next chapter. The major parameters of the simulation are the saturation surface coverage of the gas  $\theta_{\text{sat}}$ , the activation energy of the reaction  $E_A$ , the desorption activation energy  $E_{\text{des}}$ , the sticking coefficient  $S$ , the inlet gas composition and temperature. The most important output from the simulation is the concentration of  $\text{CO}_2$ . In this work, the influence of four of these parameters;  $\theta_{\text{sat}}$  for CO and O,  $E_A$  and the inlet gas composition, is studied. The saturation surface coverage of the gas or  $\theta_{\text{sat}}$  gives the maximum amount of atoms of a gas species that can adsorb on a surface. So, a  $\theta_{\text{sat}} = 1$  would imply that the surface can be covered by a monolayer of the adsorbing species. CO and  $\text{O}_2$  exhibit co-adsorption properties that are complex in nature. On the one hand, when the surface is initially filled with CO, even at a coverage of  $1/3$ , the adsorption of O is completely inhibited. When  $\theta_{\text{CO}} < 1/3$ , O can still adsorb. On the other hand, if the surface is initially filled with O, CO can still adsorb on the surface even on surfaces with  $\theta_{\text{O}} = \theta_{\text{O,max}}$  [3, 4, 33]. As the adsorption of both species is necessary for a reaction event to occur, this parameter can influence the surface composition and as a consequence, the overall conversion in the process.

The reaction rate is also dependent on the activation energy and temperature of the system. Since the temperature stays constant in the system, the activation energy can play an important role in the reaction process. The reaction rate is inversely proportional to the exponential of the activation energy,

$$r_{\text{CO}_2} \propto \exp\left(-\frac{E_A}{R_g T}\right). \quad (3.6)$$

The lower the activation energy, the higher the chances of a reaction and thus, the higher the conversion. The inlet gas composition is the easiest parameter to understand. It was explained above that CO is a dominating adsorption species. Thus the concentration of CO can impact the reaction process. It is also shown later that CO could effectively poison the surface. From the results predicted from the simulation, there was an absence of desorption of O<sub>2</sub> species. Several other studies have also shown that molecular desorption of O<sub>2</sub> occurs only at higher temperatures [15, 78]. To do the sensitivity analysis, the Pearson correlation coefficient is used. The Pearson correlation is a linear dependence of one quantity of interest on the set of influencing variables. A hypothetical parameter space is shown in figure 3.11. A coefficient  $r^2$  changes between -1 to 1. A value of 1, positive or negative, shows purely linear dependence. A value of zero suggests that the output has zero correlation to the chosen parameter. The coefficient is calculated as,

$$r^2 = \frac{\sum_{i=1}^{N_{SS}} (x_i - \tilde{x})(y_i - \tilde{y})}{\sqrt{\sum_{i=1}^{N_{SS}} (x_i - \tilde{x})^2} \sqrt{\sum_{i=1}^{N_{SS}} (y_i - \tilde{y})^2}} \quad (3.7)$$

where  $N_{SS}$  is the number of samples of the variable,  $x_i$  is the value of the  $i$ th parameter in question,  $\tilde{x}$  is the mean of the parameter values,  $y_i$  is the value of the desired output of the  $i$ th sample and  $\tilde{y}$  is the mean of all output values. The sensitivity analysis is finally used to develop a parameter space for the DSMC simulation to validate against the spectroscopic results obtained from the experiments.

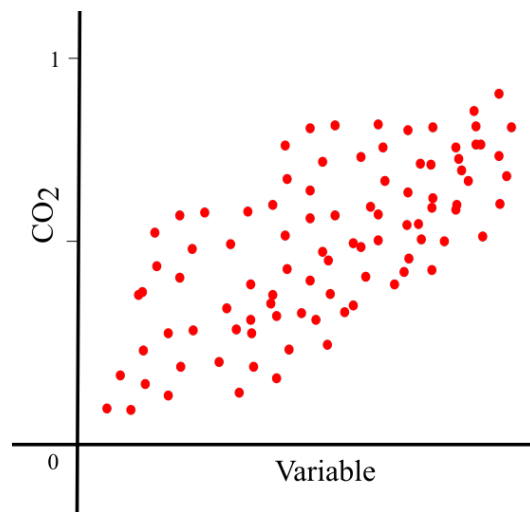


**Fig. 3.11.:** Hypothetical parameter space showing the dependence of the desired output, CO<sub>2</sub> concentration on an input variable. Graphs like this help in determining the degree of dependence for different variables. This particular example shows a positive linear dependence of the output on this particular input variable. However, there are many outliers also. Thus, while the Pearson coefficient method is good for linear dependencies, it may miss out on non-linear ones.

## Results and discussion

Users do not care about what is inside the box, as long as the box does what they need done.

---

*Jef Raskin*

All physical properties of the gas flow in DSMC are derived from the positions and velocity information of the parcels. Macroscopic properties of gas density, stream or mass velocity, mass and number flux, pressure can be determined at any location of the flow. For a small elemental volume, the properties can be time averaged (summing the properties over a large time interval) or instantaneously averaged (average in corresponding volume element over large number of similar systems). Both type of averages are probabilistic and provide fluctuations but they can describe macroscopic properties. The surface coverage per area is calculated individually for each species at each face,

$$\sigma_{p,j} = \frac{N_{\text{ads},p,j}}{A_j}, \quad (4.1)$$

where  $N_{\text{ads},p,j}$  is the number of adsorbed molecules of species  $p$  on face  $j$  and  $A_j$  is the area of the face. The desorption and reaction rate for species  $p$  are also calculated individually at each face  $j$  given by equation 2.22 and 2.20. The other macroscopic properties such as linear momentum, linear kinetic energy, internal energy and density (mass and number) are calculated as an ensemble average in each computational cell and are expressed in equation 4.2 to 4.6. Each of these macroscopic properties is averaged over all the parcels existing in the cell independent of the species.

$$p = \sum_{i=1}^{N_c} m_i u_i n_i, \quad (4.2)$$

$$E_k = \frac{1}{2} \sum_{i=1}^{N_c} m_i u_i^2, \quad (4.3)$$

$$E_i = \sum_{i=1}^{N_c} \sqrt{\frac{k_B T}{m_i}} u_i, \quad (4.4)$$

$$\rho_m = \frac{\sum_{i=1}^{N_c} m_i n_i}{V_C}, \quad (4.5)$$

$$\rho_n = \frac{\sum_{i=1}^{N_c} n_i}{V_C}, \quad (4.6)$$

where  $m_i$  is the mass of the gas species,  $u_i$  is the velocity and  $n_i$  is the size of the parcel  $i$ , the number of parcels in a cell is given by  $N_C$ , the Boltzmann constant  $k_B$ , the constant temperature  $T$  and  $V_C$  is the volume of the cell.

## 4.1 Variable Parcel Size Method

In the implementation of this scheme, parcels are initialised into the gas phase with any number of molecules. However, the maximum number possible is cut-off at  $n_{\max}$ , specified by the user. Thus, the parcels in the simulation have 1 to  $n_{\max}$  molecules. The value,  $n_{\max}$  can be entered by the user termed as “nEquivalentParticles”. Reducing the number of tracked parcels like this aids in reducing computational expense. The parcels can be maximum size in areas of high concentration and smaller in areas of lower concentration. This routine helps in preserving local concentration as well as ensemble average. The gas parcels have two vital information: parcel size (the number of molecules this particular parcel is representing) and the species of the parcel (be it CO, O<sub>2</sub> or any other type). Along with this, a parcel also contains the information about the position and velocity of the parcel.

### 4.1.1 Diffusion only

As explained in section 1.6, a balance is needed between the number of particles per cell (PPC) and parcel size ( $n$ ) to reduce the error in a DSMC computation and simulate in a reasonable time. In the following section, pure diffusion of 10 % CO in 90 % O<sub>2</sub> at 1 atm and 323 K is studied in three different groups

1. The empty computational domain is divided into hexahedral cells of different dimensions (2-20 nm) and every parcel represents a fixed number of real molecules ( $n$  ranging from 1-100). The execution time is recorded for all cases to find an adequate PPC and  $n$ .
2. The computational domain is set to a semi-infinite open cuboid. The parcel size is set to variable. The CO concentration is compared with an analytical solution.

## Diffusion in an empty cuboid; fixed parcel size: Equivalent Parcel Method

In this section, diffusion is simulated in an empty cuboid to study the dependence of the results on the computational cell size and parcel size separately. The dimensions of the cuboid are  $1000 \times 240 \times 240 \text{ nm}^3$ . The gas flows in and out of the volume through the inlet. The opposite side is a reflecting wall has a fixed zero velocity boundary condition. The other four walls are cyclic. For the first case, the simulation domain is divided into cells of different sizes ranging from 2 – 20 nm. The parcel size,  $n$  is maintained as 1. In the second case, the parcel size is differed from 1- 100 while keeping the computational cell size 8 nm. Unlike the VP method, every parcel will have a fixed number of  $n$  molecules (Fixed parcel sizes or EP method). Local CO concentration agrees well with the analytical solution of diffusion in 1D given by ,

$$c(x, t) = c_0 - \frac{4c_0}{\pi} \sum_{p=0}^{\infty} \frac{\exp\left(-\frac{D_a t (2p+1)\pi}{2l}\right)^2}{2p+1} \sin \frac{(2p+1)\pi x}{2l} \quad (4.7)$$

$$x \in [0, 1], t > 0$$

where  $c_0$  is the initial concentration,  $D_a$  is the associated diffusion coefficient and  $l$  is the distance between the inlet and the wall. For the simulation domain, diffusion is considered in the  $x$ -direction, hence,  $l = 1000 \text{ nm}$ . After doing least square minimization, a diffusion coefficient,  $D_a = 0.12 \text{ cm}^2/\text{s}$  is obtained at  $Kn = 0.54$  which is in good agreement with the literature value of  $0.18 \text{ cm}^2/\text{s}$  (diffusion of CO in air, [122]). The expected value from the empirical solution suggested by Wilke et al. is about  $0.16 \text{ cm}^2/\text{s}$  for CO-O<sub>2</sub> in an empty cuboid [123]. Figure 4.1 shows the computational time required to achieve a steady CO concentration in the domain, which is noticed around 300 ns. As the cell size increases, the computational time increases by 560 %. The computational time reduces by a further 6.5 times upon the implementation of parcel method.

**Tab. 4.1.:** Simulation parameters for study of diffusion in an empty cuboid only using fixed size parcels, given in figure 4.1.

| Parameters                          | Value                                   |
|-------------------------------------|---|
| $p$                                 | 1 atm                                   |
| $T$                                 | 323 K                                   |
| Inlet gas concentration             | 10:90                                   |
| $E_A$                               | Not applicable                          |
| Parcel Size ( $n$ )                 | (a)1 (b) Fixed, 1-100                   |
| $t$                                 | Variable up to 20 ns                    |
| Inlet and Outlet boundary condition | Fixed zero value; Reflecting outlet     |
| Computational cell size             | (a) Variable (b) 8 nm                   |
| Dimensions                          | 1000 nm $\times$ 240 nm $\times$ 240 nm |

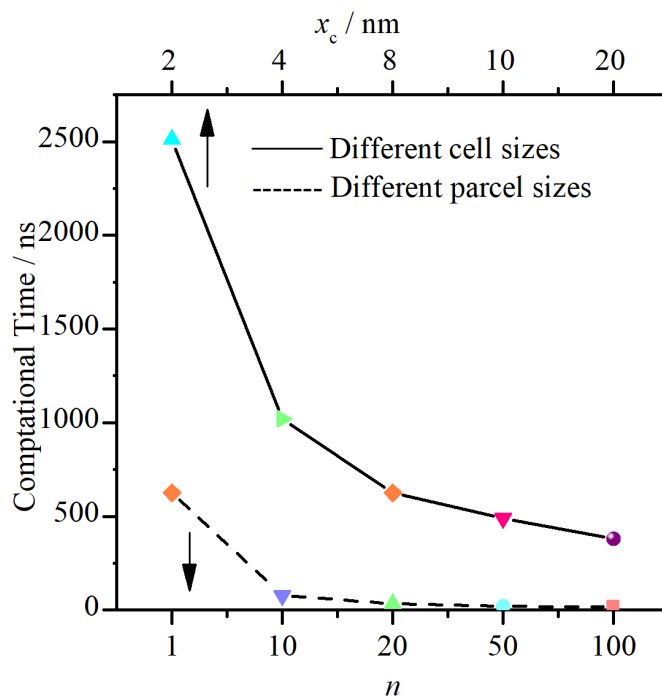


**Fig. 4.1.:** Diffusion in an empty cuboid. Gas composed of 10 % CO and 90 % O<sub>2</sub> is flowed through the inlet of the cuboid at  $T = 323$  K,  $p = 1$  atm. Computational time required to simulate 300 ns of diffusion in the cuboid is plotted here. The solid line represents the simulation volume divided into cells of different sizes at  $n = 1$  (upper  $x$ -axis). The dashed line represents the computational time for various parcel sizes when the volume is divided into 8 nm cell sizes (lower  $x$ -axis). Parameters are given in table 4.1.

## Diffusion in a semi-infinite empty cuboid; variable parcel size: Variable Parcel Method

Given that the computational time decreases with  $n$ , diffusion is simulated using the variable parcel method (VP) in a semi-open volume to check if the VP method performs as well as the EP method. The results were validated by comparison with the well-known semi-infinite one-dimensional diffusion equation [121] (see figure 4.2).

$$c(x, t) = c_0 \cdot \operatorname{erfc} \frac{x}{2\sqrt{D_a t}} \quad (4.8)$$

where initial CO concentration is  $c_0 = 0.1$  and  $\operatorname{erfc}$  is the complementary error function. As, it is impossible to implement infinite dimensions, it is instead cut off at large finite distance. Time step is chosen such that corresponding displacement is much less than root-mean-square distance for diffusion. A Monte Carlo simulated annealing algorithm [124] is used and after least squared error optimization, it leads to a diffusion coefficient value of  $D_a = 3.0619 \times 10^{-5} \text{ m}^2\text{s}^{-1}$  (Reference values: Diffusion coefficient of CO in air =  $1.817 \times 10^{-5} \text{ m}^2\text{s}^{-1}$ ). The difference observed in the two values is due to the difference of the Knudsen number. The simulation domain has  $Kn \sim 2.1853$  which is less than that for air. The lower  $Kn$  then corresponds to a higher diffusion coefficient [77].

**Tab. 4.2.:** Simulation parameters for study of diffusion only using variably sized parcels shown in figure 4.2.

| Parameters                          | Value   |
|-------------------------------------|---|
| $p$                                 | 1 atm   |
| $T$                                 | 323 K   |
| Inlet gas concentration             | 10:90   |
| $E_A$                               | N.A.  |
| Parcel Size ( $n_{\max}$ )          | 50  |
| $t$                                 | Up to 20 ns   |
| Inlet and Outlet boundary condition | Zero gradient   |
| Computational cell size             | 8 nm  |
| Dimensions                          | $10^6 \text{ nm} \times 240 \text{ nm} \times 240 \text{ nm}$ |

## Summary of diffusion only using parcels of fixed size and variable size

Two different validation cases have been shown for pure diffusion using DSMC simulation equivalent and variable parcel method. The latter method has been devised to provide more accurate representation of surface chemical reaction, while reducing the computational load. The two cases can be summarised as:

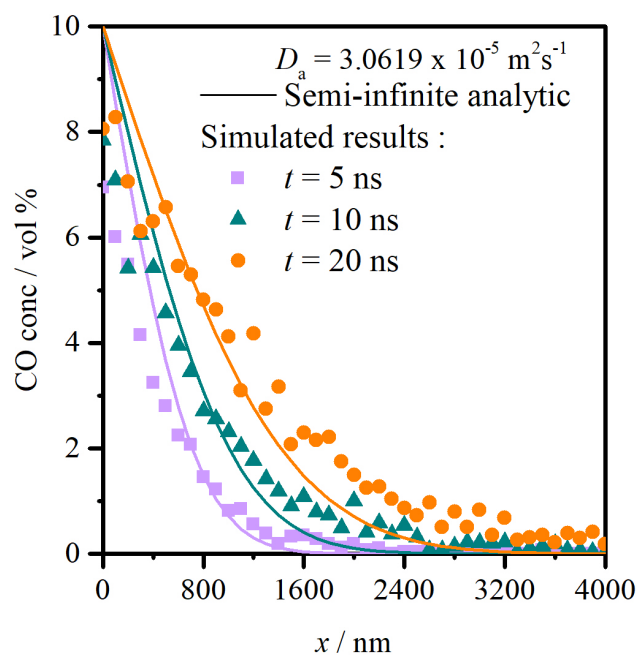


**Fig. 4.2.:** Simulation of diffusion using DSMC-VP method in a semi-infinite box. The analytical result is shown by the solid line and the simulated results are plotted as data points. Parameters are given in table 4.2.

1. Both methods show higher computational efficiency than for single molecule method. The first case shows that modulating the parcel size has a higher impact than changing the cell size.
2. Both parcel methods agree well with the analytical solution for varying boundary conditions.

#### 4.1.2 Diffusion, Adsorption and Reaction

The simulation volume described in section 3.1, figure 3.1 is divided into computational cells of 8 nm to simulate surface reactions along with diffusion. CO poisoning is highly reviewed particularly in Pd catalysts [110, 111]. In a mesoporous catalyst, it is of interest to see how poisoning occurs with respect to inlet CO:O<sub>2</sub> composition. For figure 4.3 and 4.4, the simulation is started with a surface completely clean and saturated by CO and O respectively. In both cases, the surface is completely poisoned by CO and the O coverage drops to zero for a CO:O<sub>2</sub> concentration ratio of 5:95 (see inset for 5:95). The depletion of the O coverage inhibited by CO adsorption is also seen in Engel and Ertl's molecular beam investigations [2]. Below that, the system

seems to have reached a steady state. The excess CO adsorbed gets used up in the reaction thereby, preventing poisoning of the surface (dark green and red curves). Below the concentration ratio of 1:99, the CO is completely used up in the reaction and the corresponding surface coverage is quite low (red). The opposite is valid for O<sub>2</sub>. In the absence of surface CO, the O coverage increases. Especially for the ratio 1:99, the simulation is continued up to 0.175 ms and there is an absence of CO poisoning. In figure 4.4, the initial decrease seen in the O<sub>2</sub> curves is due to the initial consumption in reactions. In contrast, for figure 4.3, the CO coverage increases with increasing CO:O<sub>2</sub> ratio and increasing time, being the dominant species of the two. For O, there is an initial increase observed for all concentration ratios as the sites are filled up simultaneously by both species. This is followed by a steep decline for higher concentration ratios 50:50 and 90:10, as CO quickly displaces the O<sub>ads</sub>. In both cases, the same steady state coverage are reached. Henceforth, the simulation can be started from maximum coverage to reduce computational time and a concentration ratio of 1:99 is maintained to avoid CO poisoning.

**Tab. 4.3.:** Simulation parameters for study of CO poisoning using VP scheme, used in figure 4.3 and 4.4.

| Parameters                          | Value                               |
|-------------------------------------|-------------------------------------|
| $p$                                 | 1 atm                               |
| $T$                                 | 723 K                               |
| Inlet gas concentration             | Variable                            |
| $E_A$                               | 83.68 kJ/mol                        |
| Parcel Size ( $n_{\max}$ )          | 100                                 |
| $t$                                 | 15000 ns (0.175 ms for ration 1:99) |
| Inlet and Outlet boundary condition | Zero gradient                       |
| Computational cell size             | 8 nm                                |
| Dimensions                          | 1000 nm × 240 nm × 240 nm           |

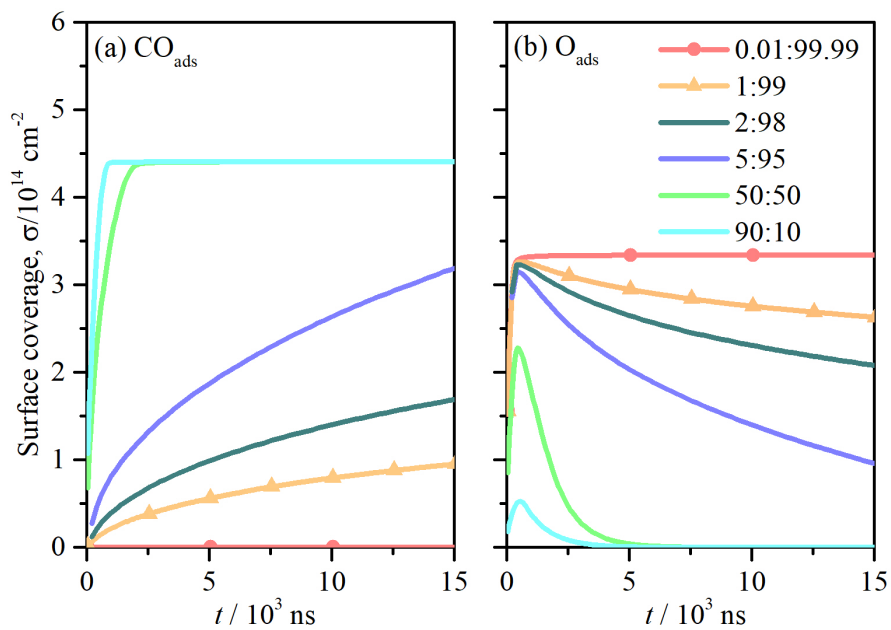


**Fig. 4.3.:** Surface coverage as a result of different CO:O<sub>2</sub> ratio starting from zero coverage. Parameters are given in table 4.3.

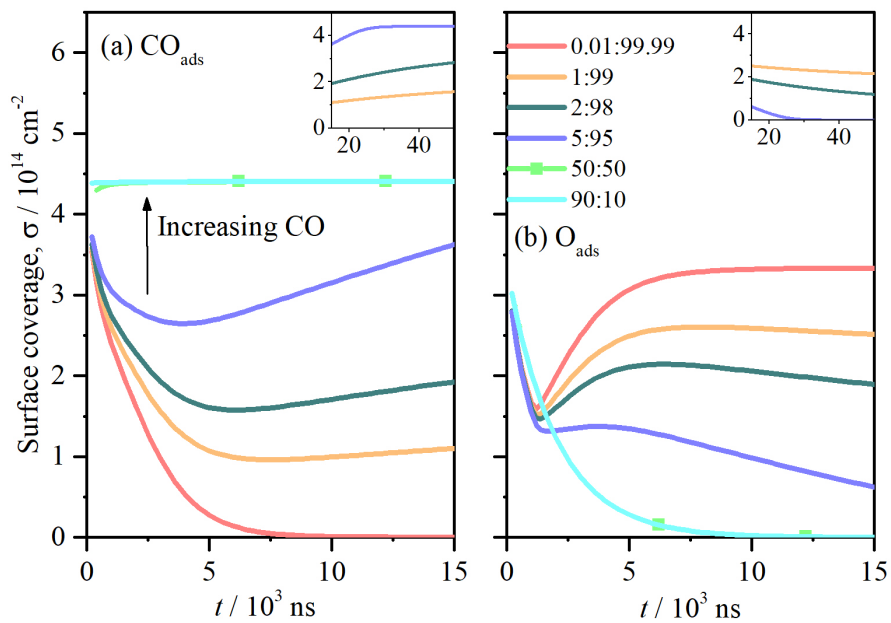


**Fig. 4.4.:** Surface coverage as a result of different CO:O<sub>2</sub> ratio starting from full coverage. Parameters are given in table 4.3.

## Physical description of the results at $n = 1$

First, all the results are described in order to decouple the rest of the discussion from the physical descriptions. As discussed above, gas composed of 1 % CO and 99 % O<sub>2</sub> is flowed through the inlet of the cuboid at different temperatures,  $p = 1$  atm. There is fixed *zero velocity gradient* at inlet and outlet and cyclic boundaries are used for other four sides in both cases. Isothermal conditions are enforced throughout the porous structure. As seen in the last section, similar steady states are achieved if the surface is clean or pre-covered. Thus, to save computational time, the surface is pre-covered with CO and O. The local CO<sub>2</sub> and cumulative CO<sub>2</sub> concentration is plotted in figure 4.5. The local concentration is quite low near the inlet as it acts as an outlet for the gases. The CO coverage is high near the inlet due to the dominant adsorption behaviour of CO seen later in figure 4.10(a) which results in poisoning of the surface and thus, reduction in CO<sub>2</sub> formation. As the gas diffuses through the structure, CO is adsorbed and reacts to form CO<sub>2</sub>. At the beginning, the coverage is maximum keeping the reaction rate high. With time, the CO coverage drops, which is followed by a drop in reaction rate. This explains the overall downwards trend of the local CO<sub>2</sub> concentration profile seen in figure 4.5. A steady state is reached at  $t = 8000$  ns. As a function of time, the conversion is at its maximum at the initial time steps as the coverage is maximum and number of CO<sub>2</sub> molecules is large. The conversion drops with time as the reaction becomes diffusion-limited.

**Tab. 4.4.:** Simulation parameters for study of local CO<sub>2</sub> and cumulative CO<sub>2</sub> using VP scheme, shown in figure 4.5.

| Parameters                          | Value                                   |
|-------------------------------------|---|
| $p$                                 | 1 atm                                   |
| $T$                                 | 723 K                                   |
| Inlet gas concentration             | 1:99                                    |
| $E_A$                               | 83.68 kJ/mol                            |
| Parcel Size ( $n_{\max}$ )          | 1                                       |
| $t$                                 | up to 8000 ns                           |
| Inlet and Outlet boundary condition | Zero gradient                           |
| Computational cell size             | 8 nm                                    |
| Dimensions                          | 1000 nm $\times$ 240 nm $\times$ 240 nm |

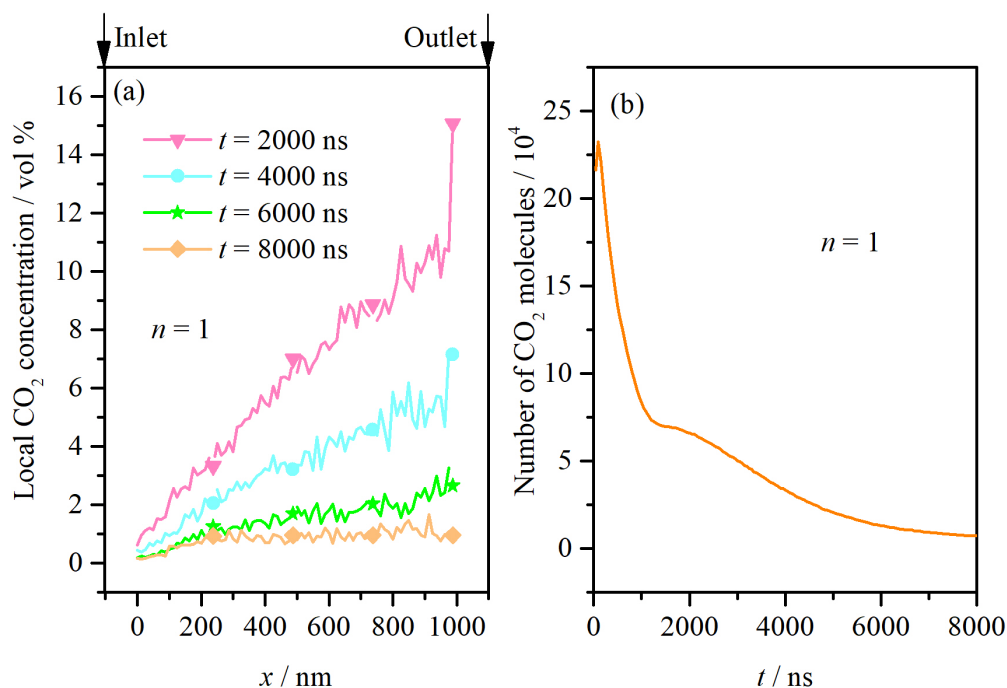


**Fig. 4.5.:** (a) Local CO<sub>2</sub> concentration and (b) Cumulative CO<sub>2</sub> versus time. The parcel size is kept fixed at 1. Parameters are given in table 4.4.

The corresponding surface coverage and local reaction rate at steady state is plotted in figure 4.6. The CO coverage is significantly higher than O near the inlet as CO adsorption is quite dominant. The local reaction rate is a product of the surface coverage and is plotted in figure 4.6(b). Thus, the local maximum is observed at  $x$  where  $\sigma_{\text{CO}} = \sigma_{\text{O}}$  is satisfied. The reaction rate curve can be divided into three regimes. The first regime is the low reaction rate near the inlet, due to the complete domination by CO. Further, in the middle region, an increase in the reaction rate occurs as the corresponding CO coverage decreases due to participation in reaction. As the CO gets completely exhausted, the reaction rate drops again and this is the final diffusion-limited regime.

**Tab. 4.5.:** Simulation parameters for study of steady state local surface coverage and reaction rate of CO and O at 723 K.

| Parameters                          | Value                                   |
|-------------------------------------|---|
| $p$                                 | 1 atm                                   |
| $T$                                 | 723 K                                   |
| Inlet gas concentration             | 1:99                                    |
| $E_A$                               | 83.68 kJ/mol                            |
| Parcel Size ( $n_{\max}$ )          | 1                                       |
| $t$                                 | 8000 ns                                 |
| Inlet and Outlet boundary condition | Zero gradient                           |
| Computational cell size             | 8 nm                                    |
| Dimensions                          | 1000 nm $\times$ 240 nm $\times$ 240 nm |

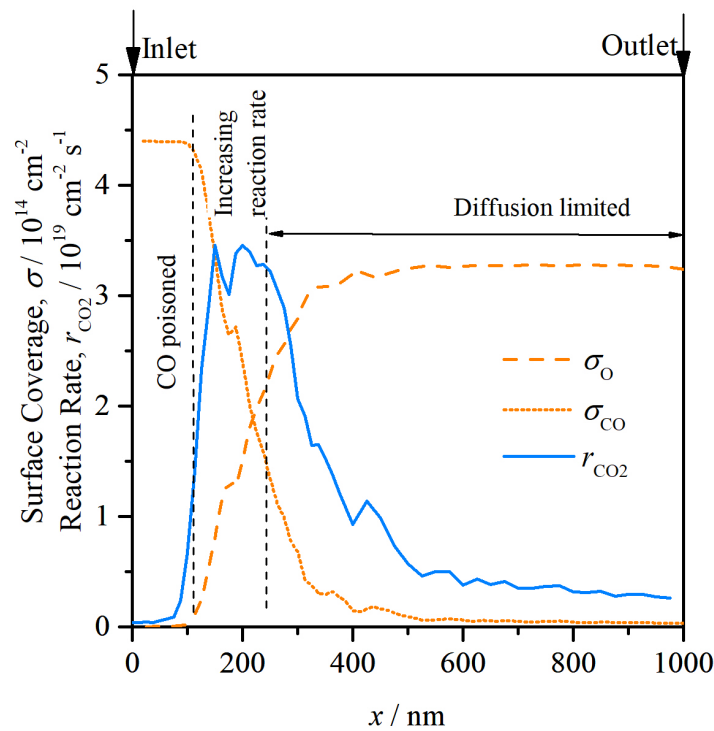


**Fig. 4.6.:** Local surface coverage (blue, solid) for  $T = 723$  K and corresponding local reaction rate  $r_{\text{CO}_2}$  (orange, dashed) as a function of  $x$  at steady state  $t = 8000$  ns using parcel size of 1. Parameters are given in table 4.5.

Arrhenius plots are often drawn to study the influence of temperature on reaction rate. In the next figure, Arrhenius plot is generated for CO oxidation in the porous structure used above in a temperature range of 473-823 K. The slope of this plot gives the activation energy of the reaction which is 81.94 kJ/mol compared to the literature value of 83.68 kJ/mol. In the steady state plot, a diffusion is seen. At higher  $T$ , the reaction rate is initially quite high because of the abundance of adsorbed CO

and O and higher reaction chance, but as CO gets depleted the reaction rate drops due to mass transfer limitation.

**Tab. 4.6.:** Simulation parameters for study of Arrhenius plots using VP scheme for figure 4.7.

| Parameters                          | Value                     |
|-------------------------------------|---------------------------|
| $p$                                 | 1 atm                     |
| $T$                                 | 473-823 K                 |
| Inlet gas concentration             | 1:99                      |
| $E_A$                               | 83.68 kJ/mol              |
| Parcel Size ( $n_{max}$ )           | 1                         |
| $t$                                 | Up to steady state        |
| Inlet and Outlet boundary condition | Zero gradient             |
| Computational cell size             | 8 nm                      |
| Dimensions                          | 1000 nm × 240 nm × 240 nm |

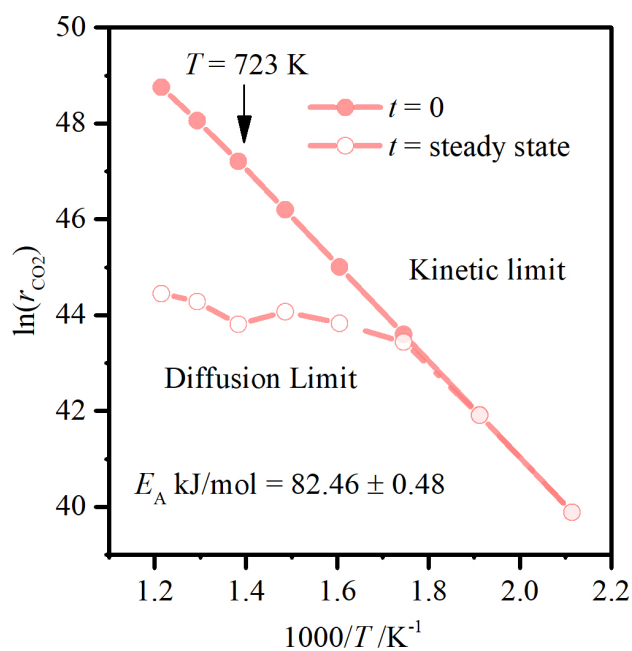


**Fig. 4.7.:** Arrhenius plot: Dependence of reaction rate on temperature at  $n = 1$ . Parameters are given in table 4.6

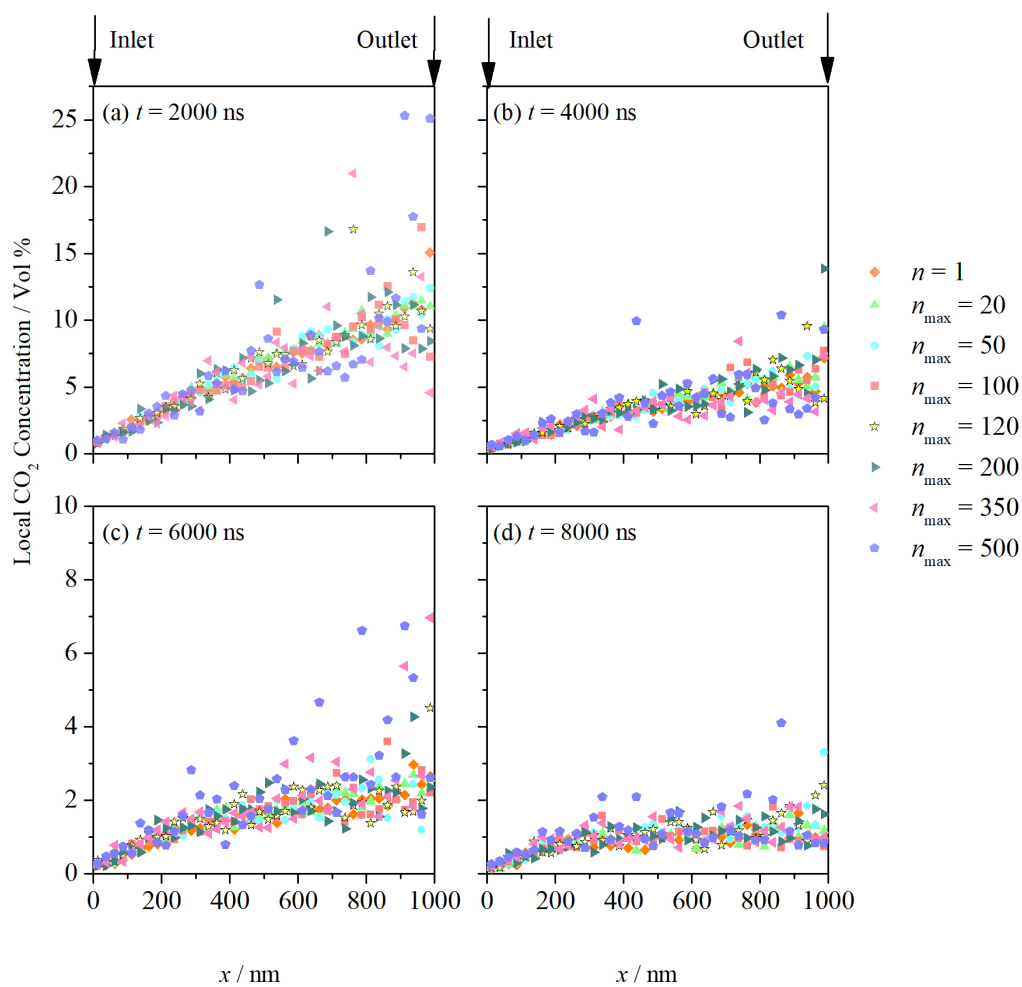
## Comparison of the results with variable parcel method

In this section, the results produced with variable parcel are compared with the results seen in the previous section. The local concentration of gaseous CO<sub>2</sub> is plotted as a function of spatial sections,  $x$  of the mesoporous structure at different time in figure 4.8. The profiles obtained show good agreement with  $n = 1$  for all the time steps. There is deviation observed for the larger parcel sizes. For parcel sizes  $\leq 200$ , the error is always less than 20 % and higher for larger parcel sizes. The discrepancy arises probably from the transfer of a larger molecule (parcel with larger  $n_{\max}$ ) from one spatial section to another. This error can be removed by averaging over larger sections at the cost of losing spatial resolution. However, unlike the EP method, the local values match better for any parcel size in this VP method which is reflected in the next figure.

**Tab. 4.7.:** Simulation parameters for study of local CO<sub>2</sub> and cumulative CO<sub>2</sub> using VP scheme.

| Parameters                          | Value                                   |
|-------------------------------------|---|
| $p$                                 | 1 atm                                   |
| $T$                                 | 723 K                                   |
| Inlet gas concentration             | 1:99                                    |
| $E_A$                               | 83.68 kJ/mol                            |
| Parcel Size ( $n_{\max}$ )          | Variable                                |
| $t$                                 | up to 8000 ns                           |
| Inlet and Outlet boundary condition | Fixed zero value; Reflecting outlet     |
| Computational cell size             | 8 nm                                    |
| Dimensions                          | 1000 nm $\times$ 240 nm $\times$ 240 nm |

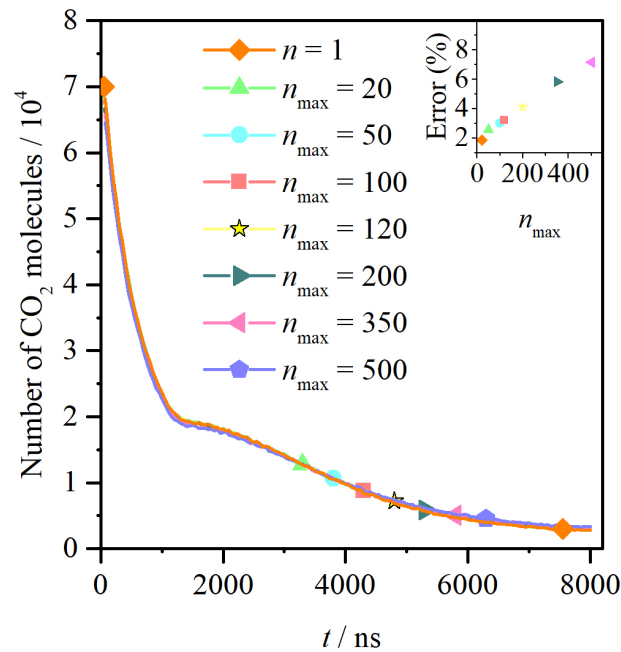
Number of molecules in each individual parcel is added up to find the cumulative CO<sub>2</sub> per time step in the total domain. Figure 4.9 shows the cumulative CO<sub>2</sub> predictions of the VP method. In VP method parcels can be re-initialised with any number of molecules and thus, it gives an accurate representation of the CO<sub>2</sub> molecules in the system. The inset in the figure shows the percentage error in the determination of cumulative CO<sub>2</sub> compared to single molecule method. The overall error is less than 7% for all cases for 4.9(a) (the standard deviation is less than the size of the symbols used) which is a good indication of the temporal resolution of the algorithm which is 50 ns.



**Fig. 4.8.:** Local CO<sub>2</sub> concentration at  $t =$  (a) 2000 ns, (b) 4000 ns, (c) 6000 ns and (d) 8000 ns. CO and O<sub>2</sub> react on Pd porous structure to form CO<sub>2</sub> following Langmuir Hinshelwood mechanism.

**Tab. 4.8.:** Simulation parameters for study of cumulative CO<sub>2</sub> using VP scheme, given in figure 4.9.

| Parameters                          | Value                     |
|-------------------------------------|---------------------------|
| $p$                                 | 1 atm                     |
| $T$                                 | 723 K                     |
| Inlet gas concentration             | 1:99                      |
| $E_A$                               | 83.68 kJ/mol              |
| Parcel Size ( $n_{\max}$ )          | Variable                  |
| $t$                                 | Up to 8000 ns             |
| Inlet and Outlet boundary condition | Zero gradient             |
| Computational cell size             | 8 nm                      |
| Dimensions                          | 1000 nm × 240 nm × 240 nm |



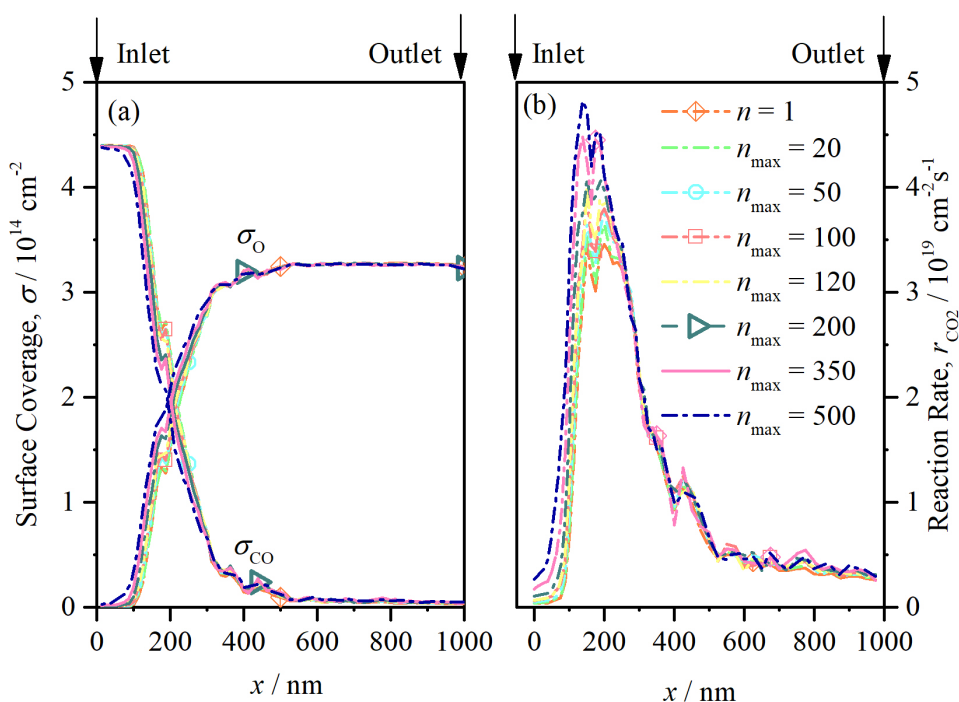
**Fig. 4.9.:** Cumulative CO<sub>2</sub> versus time simulating diffusion, adsorption and reaction in a cuboid with a mesoporous structure. Parameters are given in table 4.8.

Figure 4.10 shows the influence of variable parcel sizes on the local surface coverage and reaction rate. The CO coverage is slightly underestimated at higher parcel sizes. When the parcel size increases, the probability of O<sub>2</sub> adsorbing near the inlet increases purely due to the excess inlet composition in favour of O<sub>2</sub>. Thus, a slight increase in reaction rate is noted near the inlet with increasing  $n_{\max}$ . As the coverage are predicted well for both components, the reaction rate agrees well for all parcel

sizes. A slightly increasing reaction rate is observed for increasing  $n_{\max}$  but the position of the middle regime is similar for all cases. This shows that the VP scheme can be used to accurately predict the reaction front after optimising the parcel size with the number of processors for minimum computational time.

**Tab. 4.9.:** Simulation parameters for study of steady state local surface coverage and reaction rate of CO and O at 723 K, used in figure 4.10.

| Parameters                          | Value                                   |
|-------------------------------------|---|
| $p$                                 | 1 atm                                   |
| $T$                                 | 723 K                                   |
| Inlet gas concentration             | 1:99                                    |
| $E_A$                               | 83.68 kJ/mol                            |
| Parcel Size ( $n_{\max}$ )          | Variable                                |
| $t$                                 | 8000 ns                                 |
| Inlet and Outlet boundary condition | Zero gradient                           |
| Computational cell size             | 8 nm                                    |
| Dimensions                          | 1000 nm $\times$ 240 nm $\times$ 240 nm |



**Fig. 4.10.:** (a) Local surface coverage for  $T = 723 \text{ K}$  at steady state  $t = 8000 \text{ ns}$  for different  $n_{\max}$ . (b) Corresponding local reaction rate  $r_{\text{CO}_2}$  as a function of  $x$  using different parcel sizes.

In the figure 4.11, the Arrhenius plots are shown for different parcel sizes. The initial reaction rates match well with the “ideal” case, i.e., simulated molecules showing

one-to-one correspondence with real molecules. The values match well with the different parcel sizes used except for some over-estimation at higher temperatures for  $n_{\max} = 500$ . This corresponds to the slightly overestimated local reaction rate at this  $n_{\max}$ . These parameters are compared in figure ?? . At higher  $T$ , the reaction rate is initially quite high because of the abundance of adsorbed CO and O and higher reaction chance, but as CO gets depleted the reaction rate drops due to mass transfer limitation. The reaction rate is, in general, directly proportional to temperature as can be seen from Arrhenius plots.

**Tab. 4.10.:** Simulation parameters for study of Arrhenius plots using VP scheme, used in figure 4.11.

| Parameters                          | Value                                   |
|-------------------------------------|---|
| $p$                                 | 1 atm                                   |
| $T$                                 | 473-823 K                               |
| Inlet gas concentration             | 1:99                                    |
| $E_A$                               | 83.68 kJ/mol                            |
| Parcel Size ( $n_{\max}$ )          | 1, 20, 100 and 500                      |
| $t$                                 | Up to steady state                      |
| Inlet and Outlet boundary condition | Zero gradient                           |
| Computational cell size             | 8 nm                                    |
| Dimensions                          | 1000 nm $\times$ 240 nm $\times$ 240 nm |

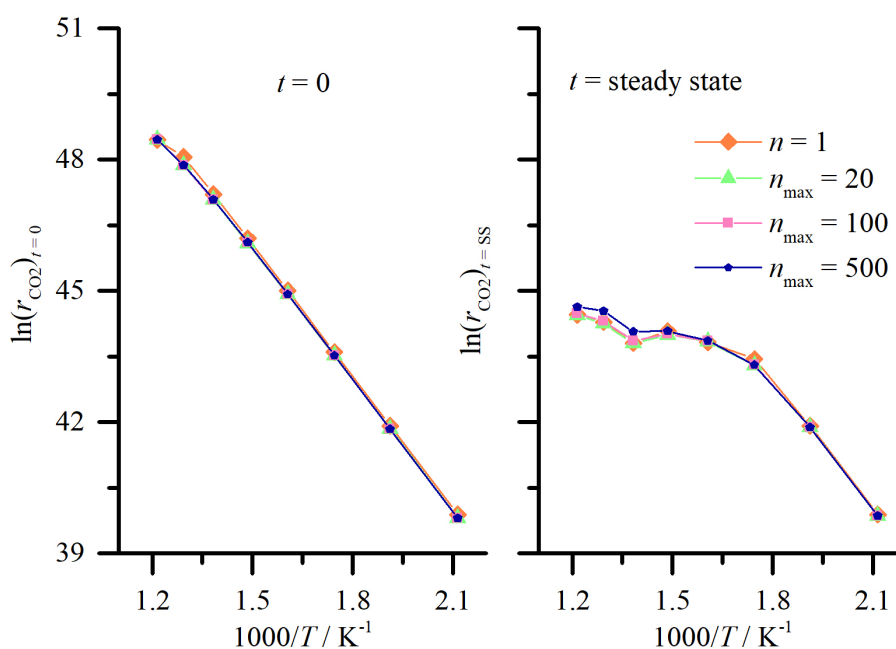


**Fig. 4.11.:** Arrhenius plot corresponding to CO oxidation on Pd representing different maximum parcel sizes in the VP scheme.

Figure 4.12 shows the computational time to achieve steady state using various parcel sizes for  $T = 723$  K. Every point represents a simulation with different  $n_{\max}$  such that all parcels in the simulation have molecules in the range 1 to  $n_{\max}$ . The computational time drops maximum by 50 % for  $n_{\max} = 50$  and decreases by 26 % for  $n_{\max} = 500$ . The efficiency of the scheme reaches a plateau as the computational time gained by tracking less parcels is lost by the amount of unnecessary calculations while adsorbing a larger parcel. For even larger parcel sizes, the significant weight difference in the parcels creates unequal distribution of work between processors. As all the results are collated at the end of each time step for such lateral decomposition of work between processors, time is used up in waiting for other processors to finish all the assigned jobs before proceeding to next time step. Thus, further increase in VP leads to a reduction in the efficiency as the workload of the processors near the inlet increases and huge communication imbalance occurs between the processors. A particle merging algorithm, as explained in section 3.2.3, is also implemented. It is

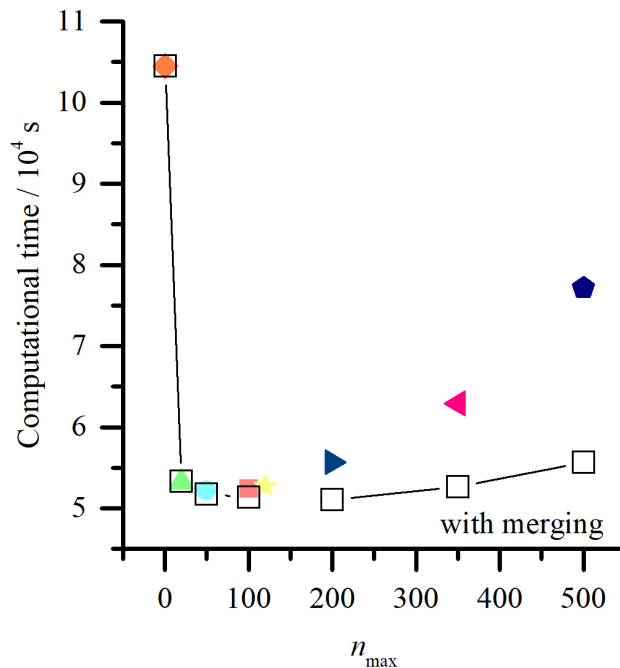


**Fig. 4.12.:** Computational time required reach steady state for CO oxidation on Pd using VP scheme. The coloured points represent simulations where agglomeration was neglected. The hollow black squares represent simulations where particle merging is achieved during collisions.

acknowledged that merging is inaccurate in terms of energy conservation. However, since that is inconsequential in terms of the big picture of this project, it has been shown here. But, it needs to be adjusted if particle size is of concern in a flow, such

as spray drying. Under this merging step, binary collisions between like parcels leads to formation of parcels of larger size, if possible. This reduces the number of parcels and along with it the tracking time. Hence, there is a significant reduction in computational time at larger parcel sizes and a more stable result overall. The general reduction is about 50 % when the merging algorithm is added along with VP scheme independent of parcel size.

### Dependence of local surface coverage on time and temperature

In figure 4.13 and 4.14, the surface coverage for CO and O are recorded versus time for  $T = 723$  K and  $573$  K respectively. For  $T = 723$  K, near the inlet, the CO coverage increases with time because surfaces are filled with CO. Figure 4.15 shows the CO coverage near the inlet for lower times. The surface is pre-covered with CO and O. Hence, the local reaction rate is uniform and high at the beginning. Thus, a uniform drop is seen in CO coverage. As the influx of CO continues, it re-covers the surface with CO again, such that at  $t = 8000$  ns, a large fraction of the surface again has full CO coverage.

Inside the reactor, more number of reactions are possible as the surfaces are less poisoned. Additionally, there is diffusion limitation of CO gas molecules. Thus, CO coverage reduces dramatically. In the absence of CO, O is adsorbed and consequentially, O coverage increases with time. At  $T = 523$  K, the reaction rate is relatively low and the adsorbed CO concentration increases and O coverage decreases steadily.

**Tab. 4.11.:** Simulation parameters for study of local surface coverage of CO and O using VP scheme. Used for figure 4.13, 4.14 and 4.15.

| Parameters                          | Value                                   |
|-------------------------------------|---|
| $p$                                 | 1 atm                                   |
| $T$                                 | 523, 723 K                              |
| Inlet gas concentration             | 1:99                                    |
| $E_A$                               | 83.68 kJ/mol                            |
| Parcel Size ( $n_{max}$ )           | Variable                                |
| $t$                                 | Up to 8000 ns                           |
| Inlet and Outlet boundary condition | Zero gradient                           |
| Computational cell size             | 8 nm                                    |
| Dimensions                          | 1000 nm $\times$ 240 nm $\times$ 240 nm |

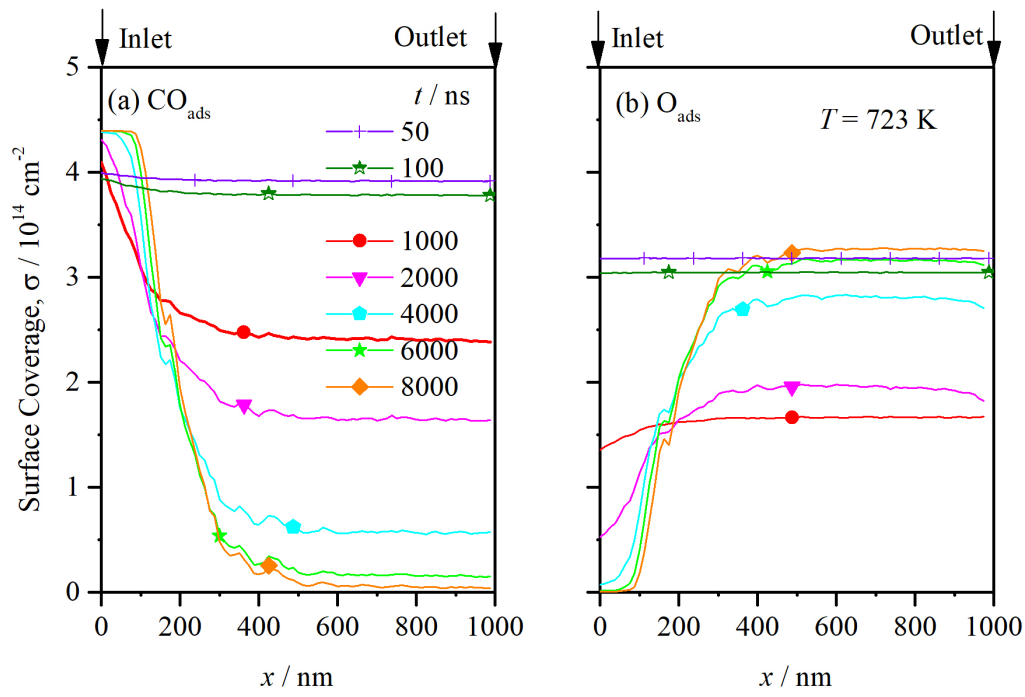


**Fig. 4.13.:** Local surface coverage (a) CO and (b) O for  $T = 723 \text{ K}$  at different  $t$  for  $n_{\text{max}} = 100$ . Parameters are given in table 4.11.

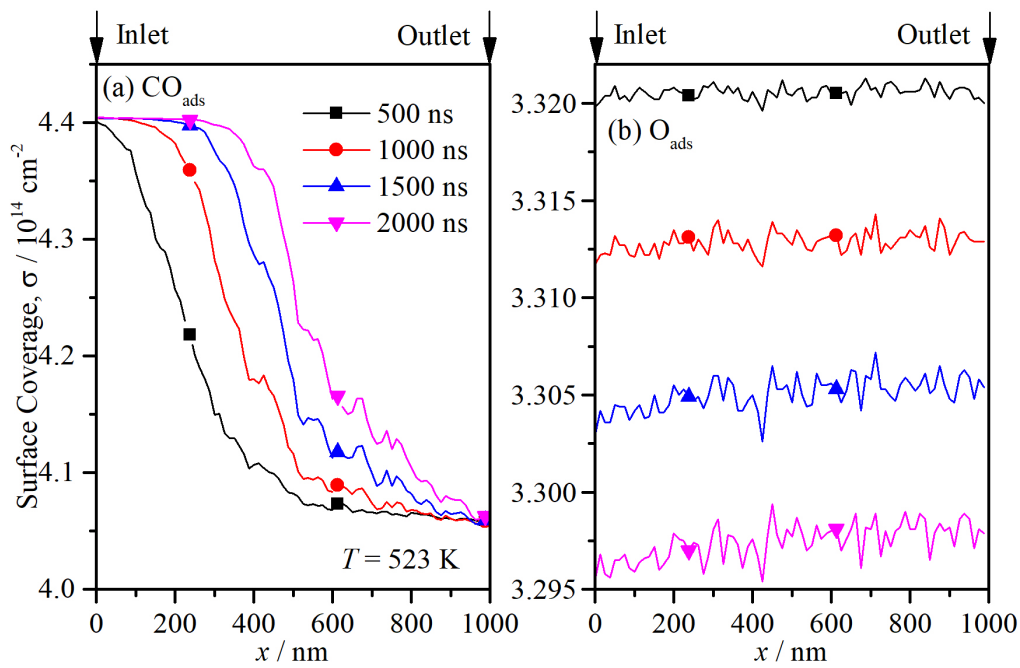


**Fig. 4.14.:** Local surface coverage (a) CO and (b) O for  $T = 523 \text{ K}$  at different  $t$  for  $n_{\text{max}} = 100$ . Parameters are given in table 4.11.

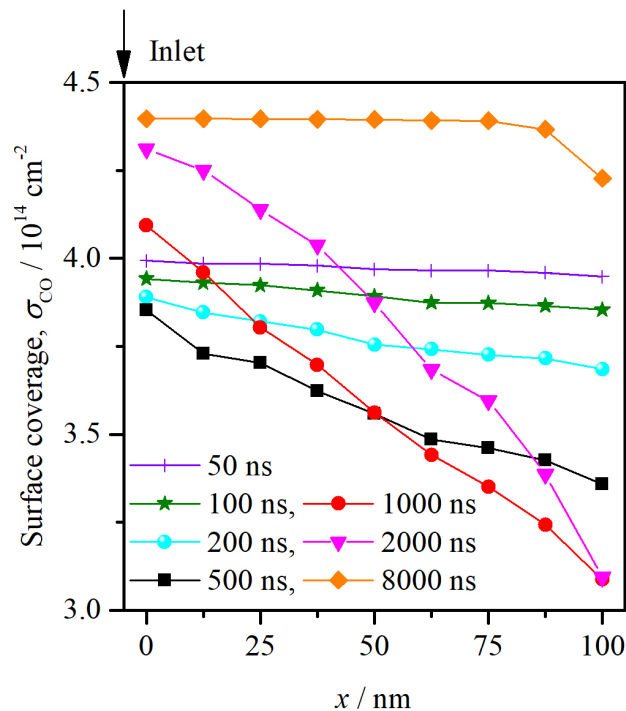


**Fig. 4.15.:** Local CO coverage near the inlet of the structure. The simulation is pre-covered with maximum CO coverage. Hence, the reaction rate is high initially and the coverage drops quickly. With time, the CO reacts off and the CO coverage drops. However, the CO coverage increases again with time due to the influx of CO molecules near the inlet and it gets covered with CO. Parameters are given in table 4.11.

In figure 4.16, the local reaction rate evolution with time is shown to compare the reaction fronts at different temperatures. At 523 K (a), the overall reaction rate is increasing as the CO coverage is increasing with time (shown in figure 4.14). Contrasting that at 723 K (c), an overall decrease of average reaction rate with time is observed in the system. The three regimes that have been described earlier also exist for each of these time steps: an initiation distance, where the surface is poisoned, followed by a gradual increase in reaction rate due to increasing adsorption of O and then a final decline owing to the depletion of adsorbed CO. A similar trend is also seen for 673 and 823 K in figure 4.16(b) and (d). However, due to the high temperature at 823 K (d), the reaction peak is achieved very early and the decline is equally steep due to a faster exhaustion of  $\text{CO}_{\text{ads}}$ . As the sticking coefficient of  $\text{O}_2$  increases with decreasing temperature while that of CO stays constant [107], the reaction rate near the inlet is high. This is because of initial maximum coverage for both species. The decline observed later is again as a result of depleted CO. The main difference observed between the  $T = 523\text{ K}$  and the other temperatures is the overall trend of the reaction rate.

**Tab. 4.12.:** Simulation parameters for study of local surface coverage and reaction rate with increasing time at different temperatures used in figure 4.16.

| Parameters                          | Value                                   |
|-------------------------------------|---|
| $p$                                 | 1 atm                                   |
| $T$                                 | 523, 623, 723 and 823 K                 |
| Inlet gas concentration             | 1:99                                    |
| $E_A$                               | 83.68 kJ/mol                            |
| Parcel Size ( $n_{\max}$ )          | 100                                     |
| $t$                                 | Up to 10000 ns                          |
| Inlet and Outlet boundary condition | Zero gradient                           |
| Computational cell size             | 8 nm                                    |
| Dimensions                          | 1000 nm $\times$ 240 nm $\times$ 240 nm |

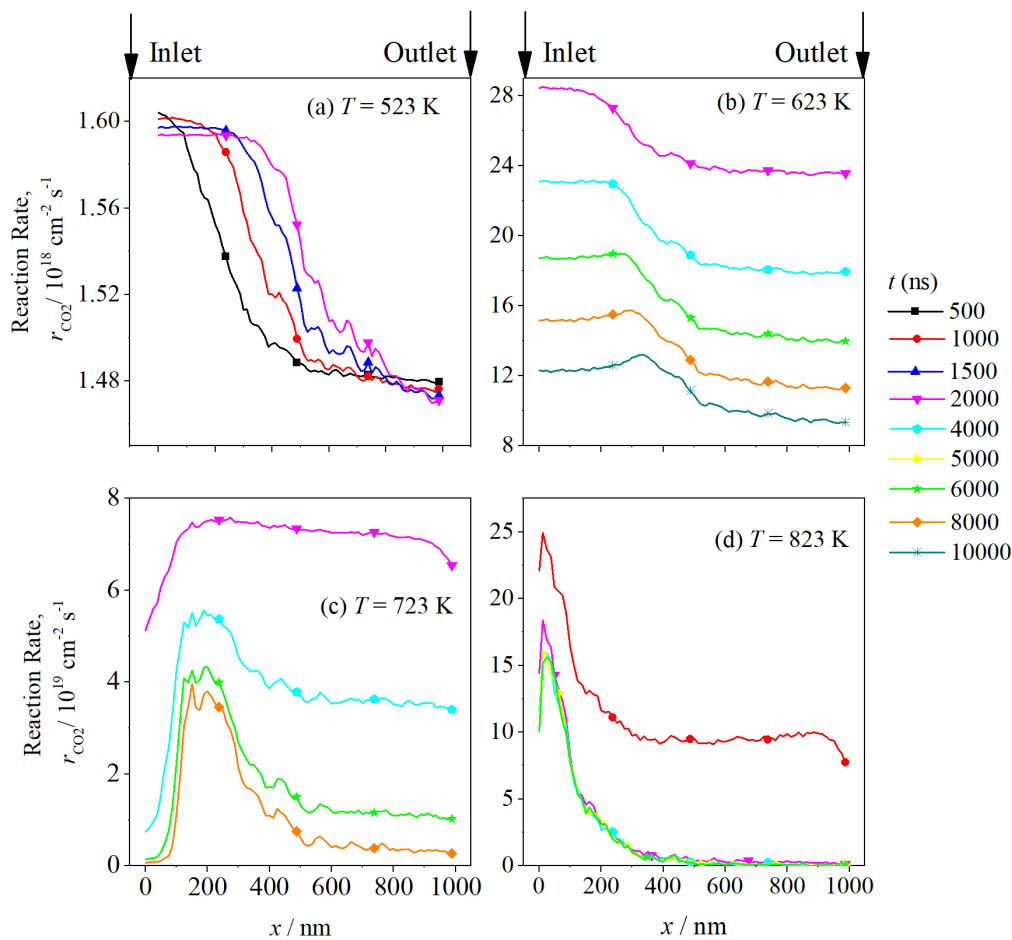


**Fig. 4.16.:** Local reaction rate with increasing time for  $T =$  (a) 523 K, (b) 623 K, (c) 723 K and (d) 823 K computed at  $n_{\max} = 100$ . Parameters are stated in table 4.12.

## Summary

The variable parcel (VP) method was developed as a modification to the equivalent parcel (EP) method to improve the accuracy of the local macroscopic properties. It was indeed possible to improve the local CO<sub>2</sub> concentration drastically by removing the restriction of a fixed parcel size (figure 4.8). The local CO and O coverage also agrees well when the parcel size is varied unlike the EP method (figure 4.10). The observations from the simulations can be summarized in these points

1. The concentration of CO was predicted in a semi-infinite system and compared with an analytical solution and the results agree well with data available from literature [10].
2. In the study of CO oxidation on the Pd catalyst, the local concentration and surface coverage were improved using parcels of varying sizes. The Arrhenius plots resulted in an activation energy of 81.94 kJ/mol, which is close to the literature value of 83.68 kJ/mol by Creighton et al. [19].
3. The computational time is significantly reduced using DSMC. However, unlike the EP method, the execution time increases with increasing  $n$ . Instead, an increase in the computational time is noticed as  $n_{\max}$  increases beyond 200. It remains constant for  $n_{\max}$  from 10 to 200. The simulation time is same for even a greater range of parcel size when agglomeration of colliding particles is assumed along with variable parcel size. Agglomeration is the combination of colliding molecules into a parcel provided the molecules are of same species with a total of  $\leq n_{\max}$ .
4. With the improved accuracy, the limit for inlet CO concentration is found to avoid Pd surface poisoning due to CO. It was found that a concentration of CO and O<sub>2</sub> below the ratio 1:99 is unable to cover the surface with CO.

## 4.2 Sensitivity Analysis

In the previous sections, it is shown that the use of DSMC code with a variable parcel scheme helps in reducing the computational load of simulating surface reactions, which is otherwise a multiscale problem with high cost of computations. In this work, it is assumed that the kinetic parameters that are adapted from UHV conditions will help in gaining a basic understanding of the system. It is clear that these parameters, thus, carry a certain degree of accommodation. The best way to test the accuracy

of the DSMC simulation would be to validate the results against an experimental setup. The results obtained from the experiments conducted by the group from Chalmers is taken as the nominal case for sensitivity study. The setup and the methodology for the experiments is explained in section 3.4. In brief, varying inlet gas composition of CO, O<sub>2</sub> and Ar is flowed through nano-channels having active Pd particles and the outlet concentration is measured using a QMS spectrophotometer. The sensitivity analysis, explained in section 3.4.1 would help in ranking the effect of input parameters. By acknowledging the rank of these input parameters, an informed decision is taken to improve the simulation parameters. This analysis is also used to verify physical models used in DSMC. It narrows the parameter space required for a full DSMC simulation.

In this study, CO, O<sub>2</sub> and Ar are diffusing through a  $10^5 \times 100 \times 500 \text{ nm}^3$  cubic channel. Only the inlet composition of CO is varied, O is kept constant at 6 % and the rest is filled by Ar. The pressure is maintained initially and is 1 atm. The temperature is kept constant at 498 K for most of the study. The channel has 18 Pd particles spaced  $5 \mu\text{m}$  apart. The entire surface of the Pd particles is assumed to be completely active. The adsorption, desorption and reaction mechanism is similar to the one explained in the previous sections. It is shown previously in figure 4.4 and 4.3 that irrespective of the initial surface coverage, the final surface coverage is decided by the saturation coverage. Thus, all the simulations are started with excess O coverage.

In the simulations, all input parameters are taken from literature obtained on CO oxidation on single crystal Pd in UHV conditions. The parameters are always subject to reactor conditions, state of the catalyst and many other factors. For the sake of simplicity and easier understanding of the simulations, the influence of the parameters is neglected and have considered an ideal reactor volume with as "ideal" conditions as possible. While comparing simulation to an experiment, the input parameters are of much more significance than before. Thus, a deep sensitivity analysis of all the input parameters is done. For the sensitivity study, certain quantities of interest (QoI) are chosen depending on the degree of influence of the input parameters (IP). These parameters would be varied from the "ideal" values considered in the earlier simulations. The four input parameters in consideration are saturation coverage of CO and O ( $\theta_{\text{sat,CO}}, \theta_{\text{sat,O}}$ ), activation energy ( $E_A$ ) and inlet CO concentration ( $\text{CO}_{\text{inlet}}$ ). The maximum influence of these parameters would be on the surface coverage of the atoms. With increasing  $\theta_{\text{sat,CO}}$  and  $\theta_{\text{sat,O}}$ , the respective surface coverage would increase proportionally. However, the dependence of CO surface coverage on increasing  $\theta_{\text{sat,O}}$  and vice versa is uncertain and needs to be explored. Inlet CO concentration also has a positive influence on the surface coverage of CO as CO is a dominant species regarding to adsorption. The influence of  $E_A$  on

the surface coverage is opposite in nature. With decreasing activation energy, more number of molecules can participate in reaction, thus, reducing the surface coverage. The next quantities of interest are reaction rate and CO<sub>2</sub> concentration. The reaction rate is directly dependent on the surface coverage of CO and O. However, an increase in CO<sub>ads</sub> could mean a decrease O<sub>ads</sub>. A reduction in the activation barrier could lead to higher reaction rate but a lower activation energy also implies lowers surface coverage. Since the formation of CO<sub>2</sub> is a direct consequence of the reaction rate, the average CO<sub>2</sub> would exhibit similar behaviour. Although, as seen later, the local CO<sub>2</sub> is different compared to average CO<sub>2</sub>. Thus, this investigation could really help in determining the important input parameters as well as the optimised combination of said parameters for the following output parameters: CO<sub>2outlet</sub>, r<sub>CO<sub>2</sub></sub>, σ<sub>CO</sub> and σ<sub>O</sub>. Table 4.13 shows a summary of the expected influence of the four input parameters on the four output variables explained above.

**Tab. 4.13.:** The input parameters (↓) and their expected influence on the quantities of interest (→) when increased in value. When the input parameter is increased, if the output parameter also increases, it is represented by a '+' and vice-versa is represented by '-'. A '+-' refers to an initial increase followed by a decrease in the output as the input parameter is increased.

|                     | CO <sub>2outlet</sub> | r <sub>CO<sub>2</sub></sub> | σ <sub>CO</sub> | σ <sub>O</sub> |
|---------------------|-----------------------|-----------------------------|-----------------|----------------|
| θ <sub>sat,CO</sub> | +                     | + -                         | +               | -              |
| θ <sub>sat,O</sub>  | +                     | +                           | -               | +              |
| E <sub>A</sub>      | -                     | -                           | +               | +              |
| CO <sub>inlet</sub> | + -                   | + -                         | +               | -              |

#### 4.2.1 Sensitivity analysis with varying input parameter θ<sub>sat,CO</sub>, θ<sub>sat,O</sub>

The saturation surface coverage of the gas or θ<sub>sat</sub> gives the maximum coverage of the adsorbing gas species on an empty surface. So, a θ<sub>sat</sub> = 1 would imply that the surface can be covered by a monolayer of the adsorbing species. CO and O<sub>2</sub> exhibit co-adsorption properties that are complex in nature. When the surface is initially filled with CO, even at a coverage of 1/3, the adsorption of O is completely inhibited. When θ<sub>sat,CO</sub> < 1/3, O can still adsorb. On the other hand, if the surface is initially filled with O, CO can still adsorb on the surface even on surfaces with θ<sub>O</sub> = θ<sub>sat,O</sub> [7, 8, 18]. As the adsorption of both species is necessary for a reaction event to occur, this parameter can influence the surface composition and as a consequence, the overall conversion in the process. For the study, θ<sub>sat,CO</sub> is increased from 0.33 to 1 and θ<sub>sat,O</sub> is increased in the range of 0.25 and 1. The coverage or the number of

adsorbed molecules can be expressed as

$$N_{\text{ads},p,j} = \sigma_{p,j} \cdot A_j. \quad (4.9)$$

Since the face area is constant, number of adsorbed parcels  $N_{\text{ads}}$  is a direct indication of coverage. The corresponding surface coverage or number of adsorbed parcels can be seen in figure 4.17 (a). It is evident from the plot 4.18(a) that the surface coverage increases with a corresponding increase in the saturation coverage. The hypothesis that is presented earlier: surface coverage on one species could affect another's is disproved. As  $\theta_{\text{sat},\text{CO}}$  is increased while keeping  $\theta_{\text{sat},\text{O}}$  constant, the  $N_{\text{ads},\text{O}}$  remains unchanged and vice-versa. The corresponding reaction rate is plotted in figure 4.17(b). The same increase in  $r_{\text{CO}_2}$  is seen with a 300 % increase in  $\theta_{\text{sat},\text{O}}$  (cyan, ▼) and just 51 % increase in  $\theta_{\text{sat},\text{CO}}$  (blue, ▲). In figure 4.18 (b), it is shown that  $r_{\text{CO}_2}$  depends on  $\theta_{\text{sat},\text{CO}}$  more than on  $\theta_{\text{sat},\text{O}}$ . When both  $\theta_{\text{sat},\text{CO}}$  and  $\theta_{\text{sat},\text{O}}$  are increased to 1.0, there is a dramatic increase in the coverage and reaction rate (figure 4.17, orange, ◀).

In figure 4.19, the change in the output,  $\text{CO}_{2\text{outlet}}$  is plotted against  $\theta_{\text{sat},\text{CO}}$  and  $\theta_{\text{sat},\text{O}}$ . As explained earlier, the production of  $\text{CO}_2$  is influenced by  $\theta_{\text{sat}}$  in the same manner that reaction rate is dependent on  $\theta_{\text{sat}}$ . Figure 4.19(b) shows that  $\text{CO}_{2\text{outlet}}$  increases almost linearly upon increasing  $\theta_{\text{sat},\text{CO}}$  while it increases exponentially in the order of  $\theta_{\text{sat},\text{O}}^{0.011}$ .

**Tab. 4.14.:** Simulation parameters for sensitivity study of  $\text{CO}_{2\text{outlet}}$ ,  $r_{\text{CO}_2}$ ,  $\sigma_{\text{CO}}$  and  $\sigma_{\text{O}}$  for each of the input variables:  $\theta_{\text{sat},\text{CO}}$ ,  $\theta_{\text{sat},\text{O}}$ . The parameters are used in figures 4.17, 4.18 and 4.19.

| Parameters  | Value                                  |
|---|--|
| $p$   | 1 atm                                  |
| $T$   | 498 K                                  |
| Inlet gas concentration                                       | CO = 1%; O <sub>2</sub> = 6 %; Rest Ar |
| $E_A$   | 83.68 kJ/mol                           |
| Parcel Size ( $n_{\text{max}}$ )                              | 50                                     |
| $t$   | 15000 ns                               |
| Inlet and Outlet boundary condition                           | Zero gradient                          |
| Computational cell size                                       | 8 nm                                   |
| $\theta_{\text{sat},\text{CO}}, \theta_{\text{sat},\text{O}}$ | Variable                               |
| Dimensions  | 86000 nm × 100 nm × 500 nm             |

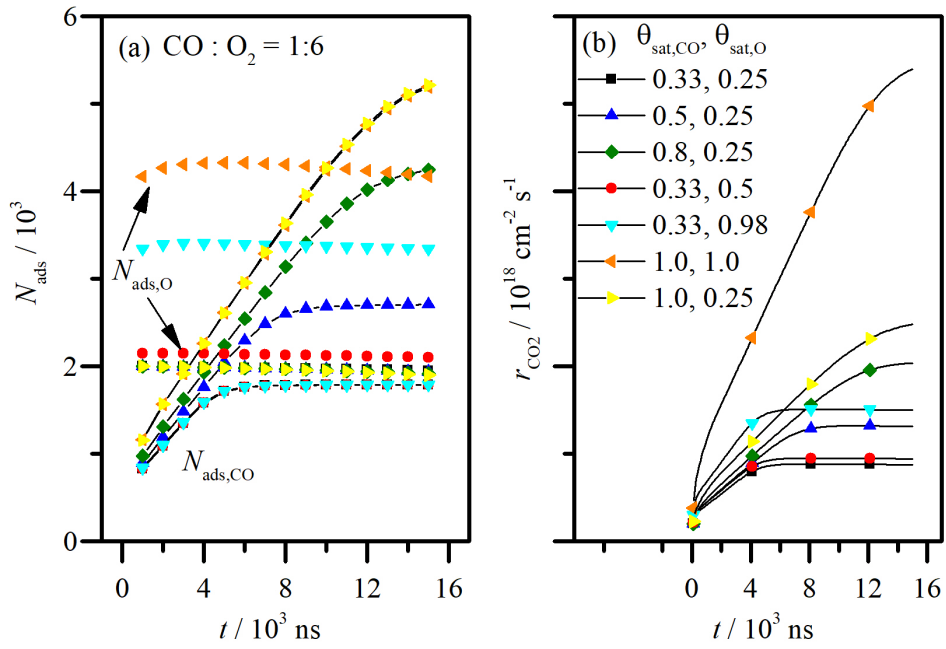


Fig. 4.17.: (a) CO (line + symbol) and O coverage (symbol) and (b) average reaction rate versus time. Input Parameters:  $\theta_{sat,CO}, \theta_{sat,O}$ . Parameters are given in table 4.14.

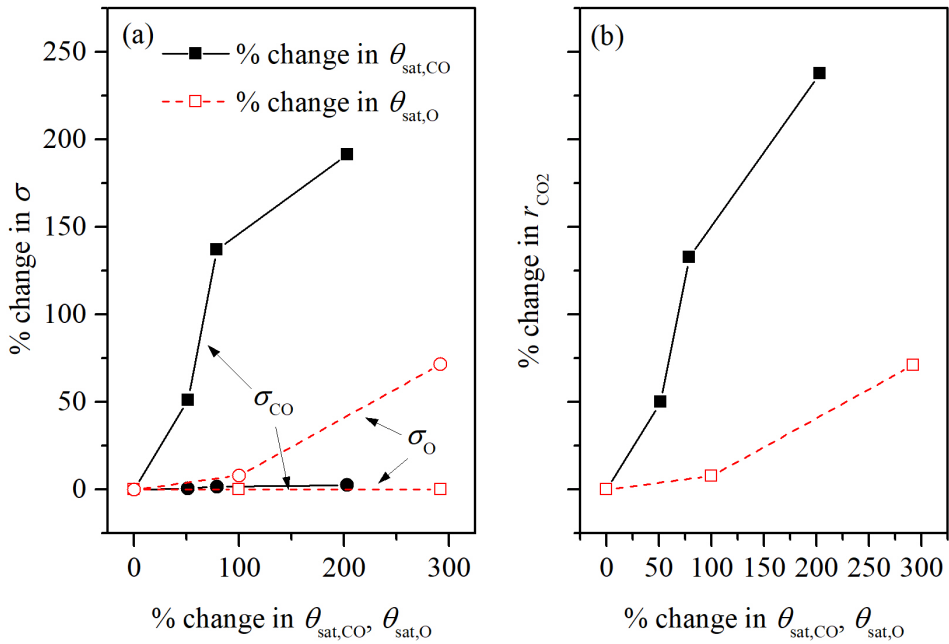
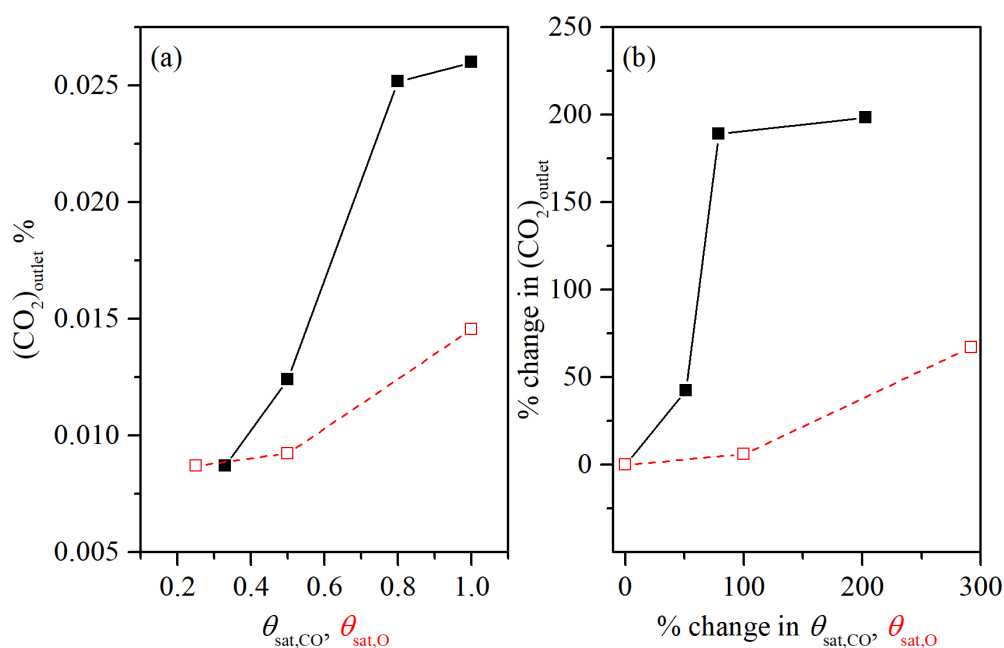


Fig. 4.18.: Sensitivity plot for % change in QoI vs IP: (a)  $\sigma_{CO}$  vs  $\theta_{sat,CO}$  (solid, square),  $\theta_{sat,O}$  (dashed, square),  $\sigma_O$  vs  $\theta_{sat,CO}$  (solid, circle),  $\theta_{sat,O}$  (dashed, circle), (b)  $r_{CO_2}$  vs  $\theta_{sat,CO}$  (solid),  $\theta_{sat,O}$  (dashed). Parameters are given in table 4.14.



**Fig. 4.19.:** (a) QoI:  $\text{CO}_{2\text{outlet}}$  at time  $t = 15000 \text{ ns}$ ; IP:  $\theta_{\text{sat,CO}}, \theta_{\text{sat,O}}$  (b) % change in  $\text{CO}_{2\text{outlet}}$  vs  $\theta_{\text{sat,CO}}, \theta_{\text{sat,O}}$ . Parameters are given in table 4.14.

#### 4.2.2 Sensitivity analysis with varying input parameter $E_A$

The activation energy,  $E_A$  is one of the crucial parameters in the prediction of reaction rate. With decrease in activation energy, there is an increase in chance of reaction given by equation 2.20. An increase in reaction probability implies that the adsorbed atoms have an increased chance of being used up in a reaction. Thus, decrease in  $E_A$  is also followed by a decrease in coverage as shown in figure 4.20. The CO surface coverage decreases dramatically with decrease in  $E_A$  (figure 4.21, black, ■). The O coverage decreases with an initial decrease and then increases as the O atoms now can adsorb on sites left by CO. The reaction rate increases due to a decrease in activation energy and decreases when the coverage is low. Thus at  $E_A < 40 \text{ kJ/mol}$ , a continuous increase and decrease in reaction rate is seen (figure A.1 shown in appendix). For  $E_A > 40 \text{ kJ/mol}$ , a diffusion limited regime follows a kinetic regime. Thus, the reaction rate drops after an initial increase. In figure 4.21, the reaction rate at  $t = 15000 \text{ ns}$  is plotted as a function of  $E_A$ . The outlet  $\text{CO}_2$  is a direct function of the reaction chance and thus, a decrease in  $E_A$  is followed by an increase in the outlet  $\text{CO}_2$  concentration, as seen in figure 4.22. Decreasing the  $E_A$  by 88 % increased the output by three orders of magnitude.

**Tab. 4.15.:** Simulation parameters for sensitivity study of  $\text{CO}_{2\text{outlet}}$ ,  $r_{\text{CO}_2}$ ,  $\sigma_{\text{CO}}$  and  $\sigma_{\text{O}}$  for the input variable:  $E_A$  shown in figures 4.20, 4.21 and 4.22.

| Parameters                                      | Value                                  |
|---|--|
| $p$   | 1 atm                                  |
| $T$   | 498 K                                  |
| Inlet gas concentration                         | CO = 1%; O <sub>2</sub> = 6 %; Rest Ar |
| $E_A$   | Variable                               |
| Parcel Size ( $n_{\text{max}}$ )                | 50                                     |
| $t$   | 15000 ns                               |
| Inlet and Outlet boundary condition             | Zero gradient                          |
| Computational cell size                         | 8 nm                                   |
| $\theta_{\text{sat,CO}}, \theta_{\text{sat,O}}$ | 0.33;0.25                              |
| Dimensions                                      | 86000 nm × 100 nm × 500 nm             |

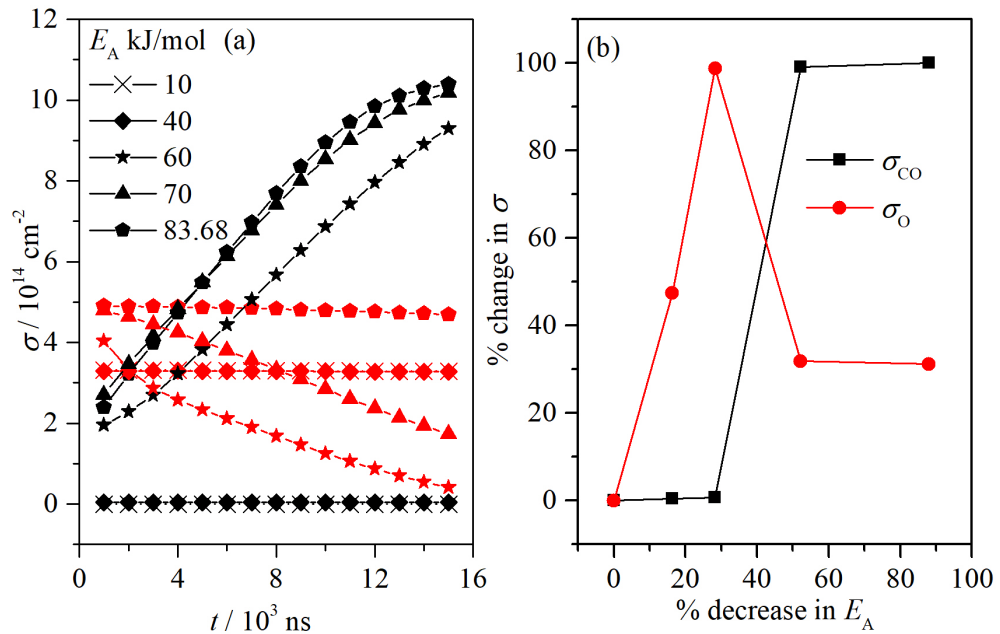


**Fig. 4.20.:** (a) QoI: CO (black),  $\sigma_{\text{CO}}$  and O (red) coverage,  $\sigma_{\text{O}}$ ; IP:  $E_A$  (b) % change in steady state coverage of CO and O vs % decrease in  $E_A$ . Parameters re given in table 4.15.

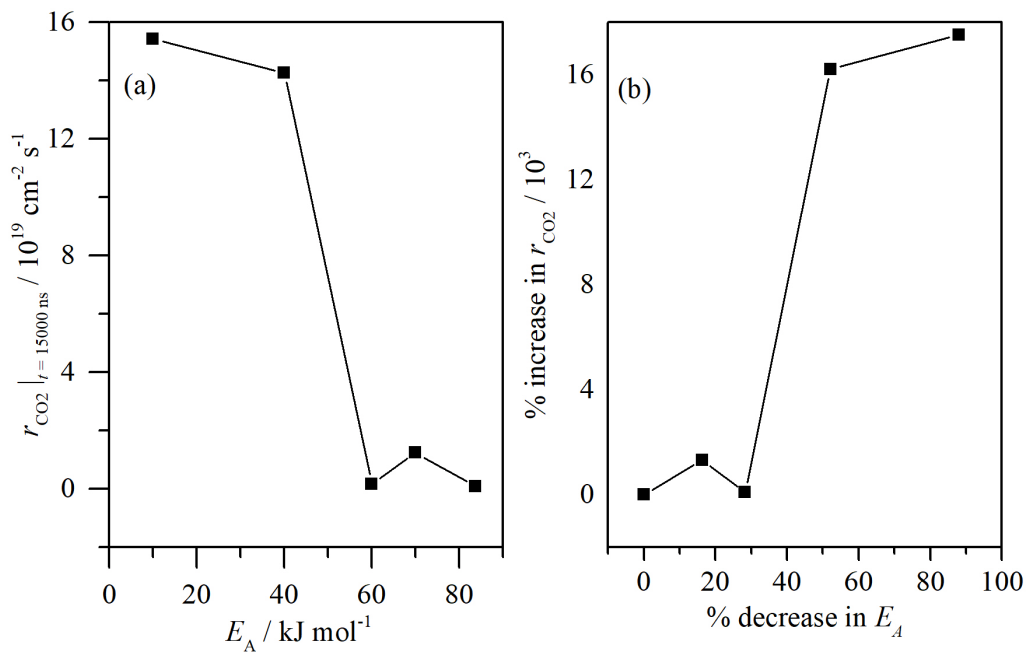


**Fig. 4.21.:** (a) QoI:  $r_{\text{CO}_2}$  at time  $t = 15000$  ns; IP:  $E_A$  (b) % change in  $r_{\text{CO}_2}$  vs % decrease in  $E_A$ . Parameters re given in table 4.15.

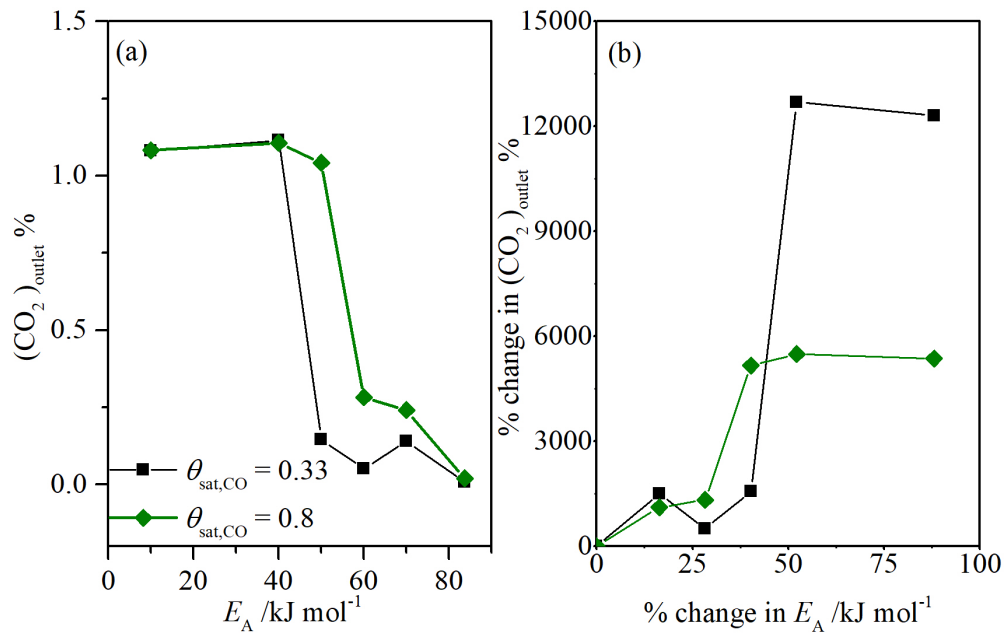


**Fig. 4.22.:** (a) QoI:  $\text{CO}_2_{\text{outlet}}$  at time  $t = 15000$  ns; IP:  $E_A$  (b) Sensitivity plot. Parameters re given in table 4.15.

### 4.2.3 Sensitivity analysis with varying input parameter $\text{CO}_{\text{inlet}}$

In this section, the inlet CO concentration is increased in the range of 0.05 to 1.4 while keeping the O concentration constant. The temperature is maintained at 498 K. The activation energy is set to 70 kJ/mol. The initial surface is filled with excess  $\text{O}_2$ . The saturation coverage for CO and O is kept 0.33 and 0.25 respectively. The corresponding average surface coverage and average reaction rate is shown in figure 4.23. As the CO concentration is increased, the CO coverage increases and it poisons the surface, the O coverage decreases. The rate of increase of CO coverage to its maximum value increases with increase in  $\text{CO}_{\text{inlet}}$ . As a result, the descent slope of O coverage also increases. This means that the reaction rate would be higher for a few time steps and then decrease as the O coverage declines. In figure 4.23(b), it is shown that this is indeed true. The average reaction rate shows a steep incline at the beginning and then it decreases. The slope of the decline is increasing with  $\text{CO}_{\text{inlet}}$ . To summarise, the  $\text{CO}_2$  production increases with increasing  $\text{CO}_{\text{inlet}}$  and then decreases when the CO begins to poison the surface. In figure 4.24,  $\text{CO}_{2\text{outlet}}$  is plotted against  $\text{CO}_{\text{inlet}}$ . There is a peak at  $\text{CO}_{\text{inlet}} = 0.4\%$  and  $0.5\%$  when  $E_A = 70$  kJ/mol and  $50$  kJ/mol respectively. A different trend is seen when  $E_A = 83.68$  kJ/mol. The amount of  $\text{CO}_{2\text{outlet}}$  increases initially but later the gradient is almost zero. This peak behavior matches well with the observed experimental results (red,  $\circ$ ) also shown in figure 4.24. The results obtained with  $E_A = 50$  kJ/mol match surprisingly well for lower CO concentrations. This is an indication that the Pd particles in question here are polycrystalline in nature rather than single crystal. Experiments on the nano-fabricated chips have already confirmed that the deposited Pd particles are polycrystalline [105]. However, the  $\text{CO}_{2\text{outlet}}$  is under-estimated for higher CO concentrations.

**Tab. 4.16.:** Simulation parameters for sensitivity study of  $\text{CO}_{2\text{outlet}}$ ,  $r_{\text{CO}_2}$ ,  $\sigma_{\text{CO}}$  and  $\sigma_{\text{O}}$  for the input variable:  $\text{CO}_{\text{inlet}}$  shown in figures 4.23 and 4.24.

| Parameters                                      | Value                                    |
|---|--|
| $p$   | 1 atm                                    |
| $T$   | 498 K                                    |
| Inlet gas concentration                         | Variable CO concentration                |
| $E_A$   | 70 kJ/mol                                |
| Parcel Size ( $n_{\text{max}}$ )                | 50                                       |
| $t$   | 15000 ns                                 |
| Inlet and Outlet boundary condition             | Zero gradient                            |
| Computational cell size                         | 8 nm                                     |
| $\theta_{\text{sat,CO}}, \theta_{\text{sat,O}}$ | 0.33;0.25                                |
| Dimensions                                      | 86000 nm $\times$ 100 nm $\times$ 500 nm |

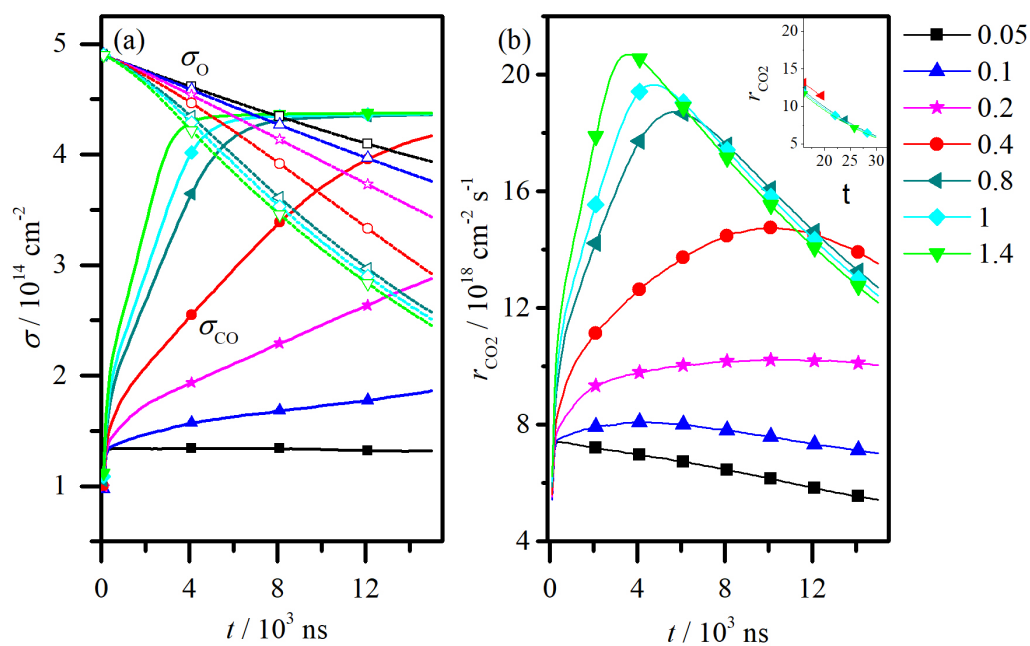


Fig. 4.23.: QoI: (a) CO and O coverage  $\sigma_{\text{CO}}, \sigma_{\text{O}}$  and (b) average reaction rate versus time. IP:  $\text{CO}_{\text{inlet}}$ . Parameters are given in table 4.16.

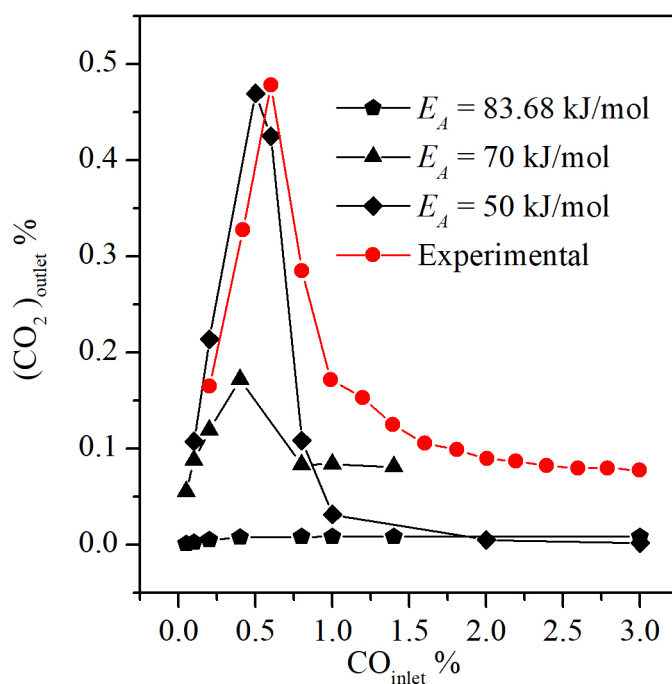


Fig. 4.24.: QoI: (a) Predicted (black)  $\text{CO}_2_{\text{outlet}}$  at two different activation energy. IP:  $\text{CO}_{\text{inlet}}$  at  $T = 498 \text{ K}$ . Parameters are given in table 4.16.

## 4.2.4 Pearson coefficient calculation

As mentioned earlier, the Pearson correlation coefficient  $r^2$  is a measurement of the linear dependence of an output on the input variables. The coefficient is calculated for all quantities of interest:  $\text{CO}_{2\text{outlet}}$ ,  $r_{\text{CO}_2}$ ,  $\sigma_{\text{CO}}$  and  $\sigma_{\text{O}}$  for each of the input variables:  $\theta_{\text{sat,CO}}$ ,  $\theta_{\text{sat,O}}$ ,  $E_{\text{A}}$  and  $\text{CO}_{\text{inlet}}$ . The value of the coefficient varies between -1 to 1, where a value of 1 or -1 means a positive or negative linear dependence respectively and a value of 0 signifies zero correlation whatsoever. The input parameters can then be ranked in order of influence. For all QoIs, the first rank is clearly explained. The dependence of  $\sigma_{\text{CO}}$  and  $\sigma_{\text{O}}$  on the maximum saturation coverage  $\theta_{\text{sat,CO}}$  and  $\theta_{\text{sat,O}}$  respectively is straightforward. Higher the value of  $\theta_{\text{sat}}$ , more molecules can adsorb on the surface and thus, the respective coverage would be higher. The negative dependence of  $r_{\text{CO}_2}$  on  $E_{\text{A}}$  is also explained in the earlier sections. This reasoning also explains why the production of  $\text{CO}_2$  is also dependent on  $E_{\text{A}}$ . However, some of the values are incorrect. For example, in figure 4.17 and 4.19, it is shown that the reaction rate and  $\text{CO}_{2\text{outlet}}$  increases with increasing  $\theta_{\text{sat,O}}$ , non-linearly in nature. But the coefficient shows negative value which is untrue. The Pearson coefficient is not the best method to capture non-linearity of relationships between two variables [125]. The implementation of the sophisticated methods for doing such analysis is suggested in ref. [125] but is beyond the scope of this work. The table 4.17 shows that the  $\text{CO}_{2\text{outlet}}$  concentrations is most influenced by  $E_{\text{A}}$ ,  $\theta_{\text{sat,CO}}$  and  $\theta_{\text{sat,O}}$ . Although the linear relationship with  $E_{\text{A}}$  is clear from figure 4.24, the dependence on coverage is still unclear. It seems from that figure that at higher  $\text{CO}_{\text{inlet}}$  concentrations (1-3 %), the CO coverage inhibits the adsorption of O and reduces the reaction rate. In the future sections, adsorption and desorption parameters are probed to develop a new model for CO and O coverage (previous model: equation 2.15 and 2.16.)

**Tab. 4.17.:** Summary of the Pearson correlation coefficient for different QoI at varying IP.

| Parameter                  | $\text{CO}_{2\text{outlet}}$ | $r_{\text{CO}_2}$ | $\sigma_{\text{CO}}$ | $\sigma_{\text{O}}$ |
|----------------------------|------------------------------|-------------------|----------------------|---------------------|
| $\theta_{\text{sat,CO}}$   | 0.234373                     | 0.318023          | 0.660216             | 0.112472            |
| $\theta_{\text{sat,O}}$    | -0.11301                     | -0.09391          | 0.280545             | 0.693912            |
| $E_{\text{A}}$             | -0.88895                     | -0.75269          | 0.4625               | 0.435619            |
| $\text{CO}_{\text{inlet}}$ | -0.08617                     | -0.06677          | 0.045362             | 0.083707            |

#### 4.2.5 Sensitivity analysis of desorption parameters

In section 2.4.3, the desorption mechanism is described in detail. For the sensitivity analysis all the desorption parameters, the pre-exponential factor and the desorption activation energy are varied. However, the desorption parameters hardly have any significant effects on the outlet concentration.

#### 4.2.6 Sensitivity analysis of adsorption parameters

The adsorption subroutine is explained in section 2.4.1. Out of all the parameters considered in the adsorption model, two significant parameters are chosen: sticking coefficient,  $S$  and exponent used to describe the coverage term (shown in bold).

$$S_{\text{CO}} = S_0 \left( 1 + K \left( \frac{1}{(1 - \theta_{\text{current}})^{\mathbf{1}}} - 1 \right) \right)$$

$$S_{\text{O}} = S_0 \left( 1 + K \left( \frac{1}{(1 - \theta_{\text{current}})^{\mathbf{2}}} - 1 \right) \right)$$

Figure 4.25(a) shows that  $\text{CO}_{2\text{outlet}}$  increases with decreasing  $S_{\text{CO}}$ . However, the O parameters (red) show that an increase in O coverage always leads to higher  $\text{CO}_2$  output. Similar to desorption parameters, adsorption parameters are insignificant to making changes in  $\text{CO}_{2\text{outlet}}$  concentration. In figure 4.19, it is shown that reduction in  $\theta_{\text{satCO}}$  increases the  $\text{CO}_2$  concentration. To expand the effects and to reduce the inhibition ramifications of CO coverage, a new parameter is introduced,  $k_{\text{CO}}$ . The parameter  $k_{\text{CO}}$  accounts for a lower inhibition effect of adsorbed CO with increasing temperature. Equation 2.16 implies that the number of available vacant sites for O adsorption is inversely proportional to the sum of occupied CO and O sites. However, modifying the equation like this,

$$\theta_{\text{req,O}} = \left( 1 - \frac{\theta_{\text{O}}}{\theta_{\text{max,O}}} - k_{\text{CO}} \cdot \frac{\theta_{\text{CO}}}{\theta_{\text{max,CO}}} \right)^2, \quad (4.10)$$

reduces the effect of CO adsorption. In figure 4.26, it is shown that, reducing  $k_{\text{CO}}$  makes a dramatic increase in  $\text{CO}_{2\text{outlet}}$ . However, further increase in  $k_{\text{CO}}$  has little influence on the  $\text{CO}_2$  concentration as O surface adsorption is completely inhibited.

**Tab. 4.18.:** Simulation parameters for sensitivity study of adsorption parameters  $S_{CO}$ ,  $S_O$ ,  $expCO$  and  $expO$  used in figure 4.25.

| Parameters                          | Value                                    |
|-------------------------------------|--|
| $p$                                 | 1 atm                                    |
| $T$                                 | 498 K                                    |
| Inlet CO gas concentration          | 1 %                                      |
| $E_A$                               | 70 kJ/mol                                |
| Parcel Size ( $n_{max}$ )           | 50                                       |
| $t$                                 | 15000 ns                                 |
| Inlet and Outlet boundary condition | Zero gradient                            |
| Computational cell size             | 8 nm                                     |
| $\theta_{sat,CO}, \theta_{sat,O}$   | 0.33;0.25                                |
| Dimensions                          | 86000 nm $\times$ 100 nm $\times$ 500 nm |

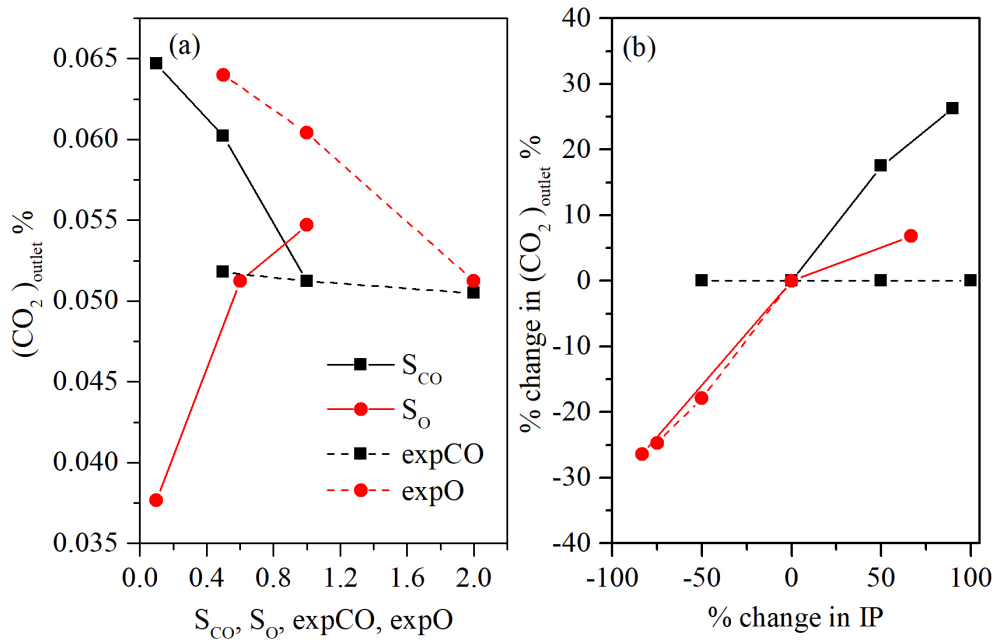


**Fig. 4.25.:** (a)  $CO_{2outlet}$  concentration as sticking coefficients,  $S_{CO}$  and  $S_O$  and exponent of the coverage term to calculate  $S$ ,  $expCO$  and  $expO$  are modified. (b) % change in  $CO_{2outlet}$  versus % change in the adsorption parameters. Parameters are given in table 4.18.

**Tab. 4.19.:** Simulation parameters for sensitivity study of a new adsorption parameter  $k_{\text{CO}}$  shown in figure 4.26.

| Parameters                                      | Value                                    |
|---|--|
| $p$   | 1 atm                                    |
| $T$   | 498 K                                    |
| Inlet CO gas concentration                      | 4 %                                      |
| $E_A$   | 50 kJ/mol                                |
| Parcel Size ( $n_{\text{max}}$ )                | 50                                       |
| $t$   | Until steady state                       |
| Inlet and Outlet boundary condition             | Zero gradient                            |
| Computational cell size                         | 8 nm                                     |
| $\theta_{\text{sat,CO}}, \theta_{\text{sat,O}}$ | 0.1; 0.25                                |
| Dimensions                                      | 86000 nm $\times$ 100 nm $\times$ 500 nm |

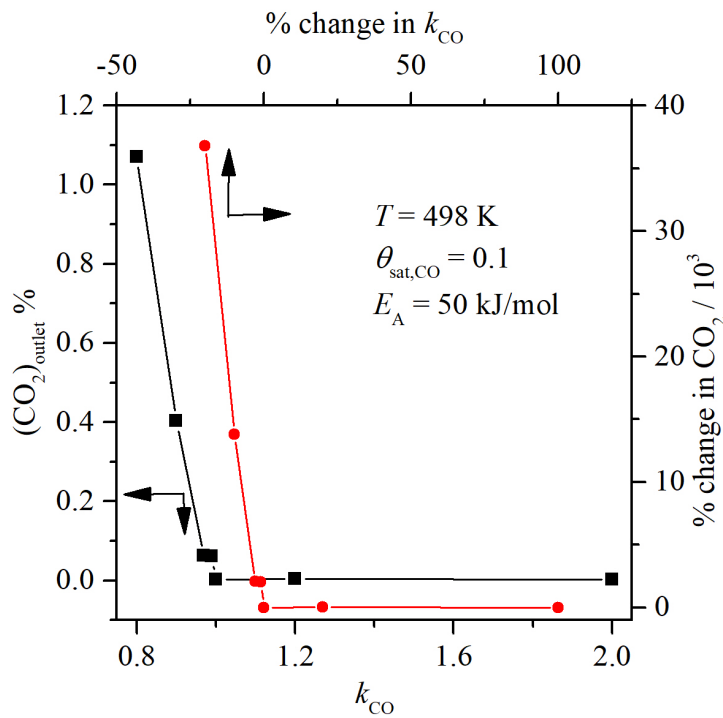


**Fig. 4.26.:**  $\text{CO}_{2,\text{outlet}}$  as a function of  $k_{\text{CO}}$  at  $T = 498$  K. It is combined with a lower  $\theta_{\text{sat,CO}}$  and a lower activation energy. This also shows that a change of 30 % increases the  $\text{CO}_{2,\text{outlet}}$  by three orders of magnitude. Parameters are given in table 4.19.

## 4.2.7 Validation and further insights

After doing the comprehensive sensitivity study,  $E_A$ ,  $\theta_{\text{sat,CO}}$  and  $k_{\text{CO}}$  are the most influential parameters. For validation with experimental results, a new combination of values for these parameters has been used to build a microkinetic model specific to the experimental setup. All new parameters have relevance within physical bounds. Polycrystalline surfaces such as the Pd particles deposited in the nanochannels have a lowered  $E_A$  and  $\theta_{\text{sat,CO}}$  due to exposed facets and steps [105]. Snabl et al. and Kaukonen et al. have shown that a heightened diffusion process at higher temperature helps reducing CO coverage and this explains the parameter  $k_{\text{CO}}$  which is dependent on temperature [112, 113]. Snabl et al. reported CO diffusion on Pd(111) defect-sites with the diffusion coefficient increasing with temperature [112]. Kaukonen et al. support this in their MC simulation, CO diffusion on the surface improves reactivity by avoiding formation of CO clusters [113]. In figure 4.27, simulations are performed at three different temperatures. At all temperatures, the coverage extent of CO ( $\theta_{\text{sat,CO}}$ ) is limited to 0.1 and  $E_A$  is fixed at 50 kJ/mol. Since  $k_{\text{CO}}$  depends on temperature, the best fits are found for each temperature and are shown in the figure. Different models were tested prior to adopting the model given by equation 4.10. An example for such analysis at  $T = 548$  K is given in appendix. The decreasing values of  $k_{\text{CO}}$  are representative of the reducing effect of CO coverage on O adsorption.

As the simulation is validated against the experimental results, the simulation can be exploited to gather local data. DSMC is a phenomenological model where all macroscopic properties can be directly derived from the parcels directly. Aside from that, DSMC also provides detailed data on the local surface coverage and reaction rates. These details are vital in determining the operation and performance of the nanofluidic channels via the reactivity of the particles, yield per particle, the most active particle. This type of flow physics gives direct access to data unavailable in experiments alone.

In figure 4.28, the average local reaction rate and coverage is shown. The temperature is a constant 548 K and  $\text{CO}_{\text{inlet}}$  is increased from 0.1-3 %. The results confirm that increasing CO coverage on the particles increase the reaction rate at first. But further increase in CO coverage, for  $\text{CO}_{\text{inlet}} \geq 0.8$ , renders the particle inactive. For the higher concentrations ( $\text{CO}_{\text{inlet}} \geq 2.0$ ) most of the Pd particles are inactive at steady state. Only the Pd particles near the outlet are barely active with a low reaction rate. In figure 4.29, the CO inlet is fixed at 2 % while the temperature is regularly increased. As shown in the previous figure, the Pd particles in the nanofluidic channel are almost poisoned at 498 K at such inlet concentrations. Upon increasing temperature, the reaction rate increases removing the overcrowding CO

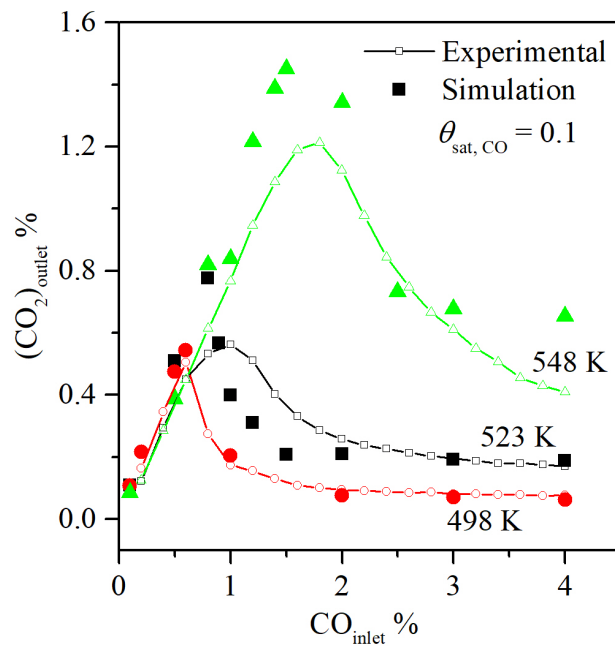


**Fig. 4.27.:** CO<sub>2</sub><sub>outlet</sub> predicted (dashed) and experimental (solid) concentration as CO<sub>inlet</sub> concentration is increased. Three temperatures are included. The  $k_{\text{CO}}$  values are the best fits obtained for that temperature.

coverage keeping the Pd particles active longer and providing a higher CO<sub>2</sub> turnover. Such comprehension into the channels can be used to find reaction fronts in reactors with ramping temperatures.

But, DSMC can provide even further insights into the coverage on individual Pd particles. In figure 4.30, the CO coverage and reaction rate are shown on the 6<sup>th</sup> particle in the nanofluidic channel at 523 K. Each individual Pd particle is represented in the simulation by a series of patches. Only the top surface is shown here. As the number of time steps increases, CO coverage increases, thus increasing the reaction rate (shown in background of the Pd particle). But as CO coverage continually increases, O adsorption gets inhibited and the reaction rate falls to zero.

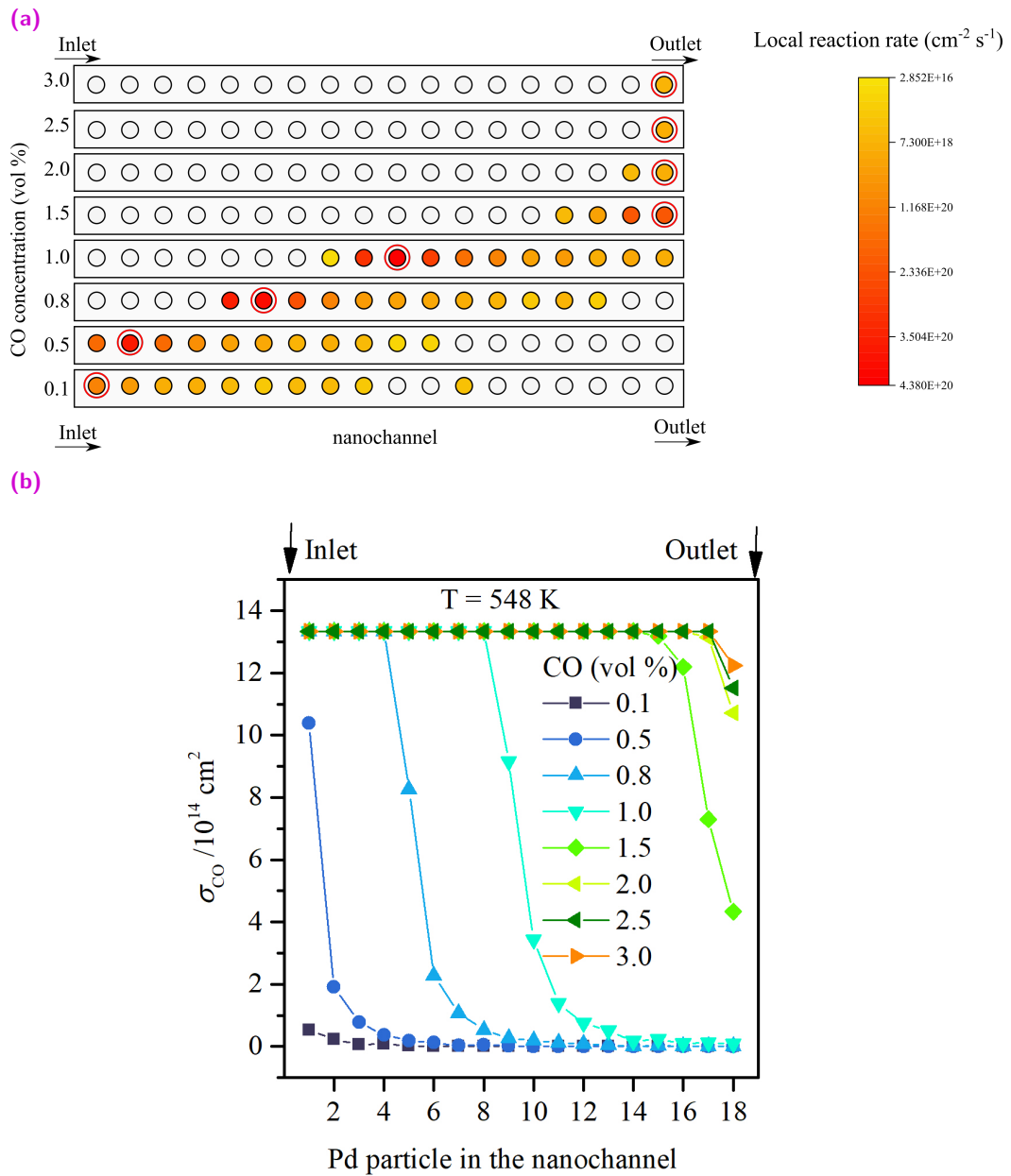


**Fig. 4.28.:** (a) Local average reaction rate and (b) local average CO coverage across the channel at  $T = 548 \text{ K}$  as  $\text{CO}_{\text{inlet}}$  is increased from 0.1 to 3.0 %. The particle with the maximum reaction rate at any particular  $\text{CO}_{\text{inlet}}$  is encircled in red. The maximum reaction rate observed on an individual Pd particle shifts towards the centre of the channel ( $\text{CO}_{\text{inlet}} = 1.0 \%$ ) as the  $\text{CO}_2$  peak is crossed and moves towards the outlet as the concentration is further increased. Below  $\text{CO}_{\text{inlet}} = 1.0 \%$ , the Pd particles near the outlet have zero reactivity owing to a lack of adsorbed reactants. Higher concentration white particles indicates poisoning of the Pd surface by CO leading to very low reaction rate.  $\theta_{\text{CO}} = 0.1, k_{\text{CO}} = 1.0$ .

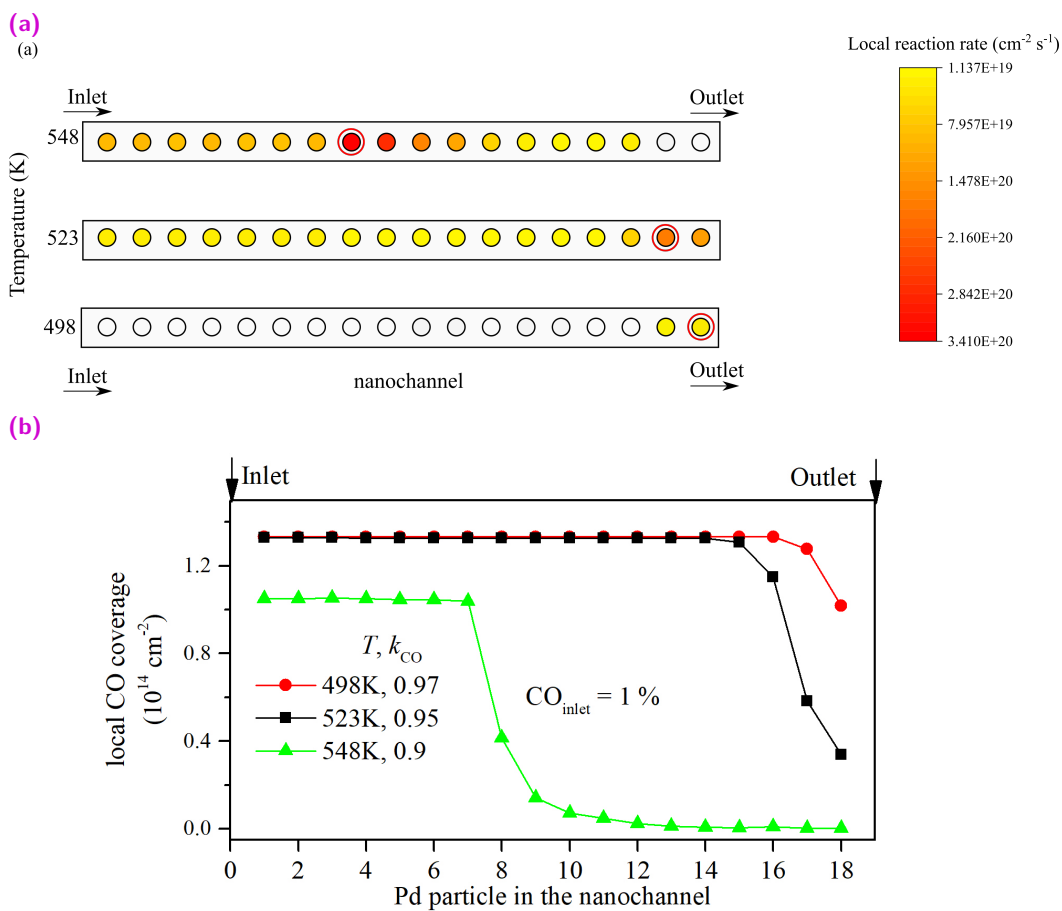


**Fig. 4.29.:** (a) Local average reaction rate and (b) local average CO coverage for  $\text{CO}_{\text{inlet}} = 1.0\%$  at different temperatures. The Pd particles at 498 K are CO poisoned and the reaction rate is very low. For 498 K, the entire channel is poisoned whereas the nanochannel is active at 523 K and 548 K due to reduced CO coverage because of higher reaction rate.

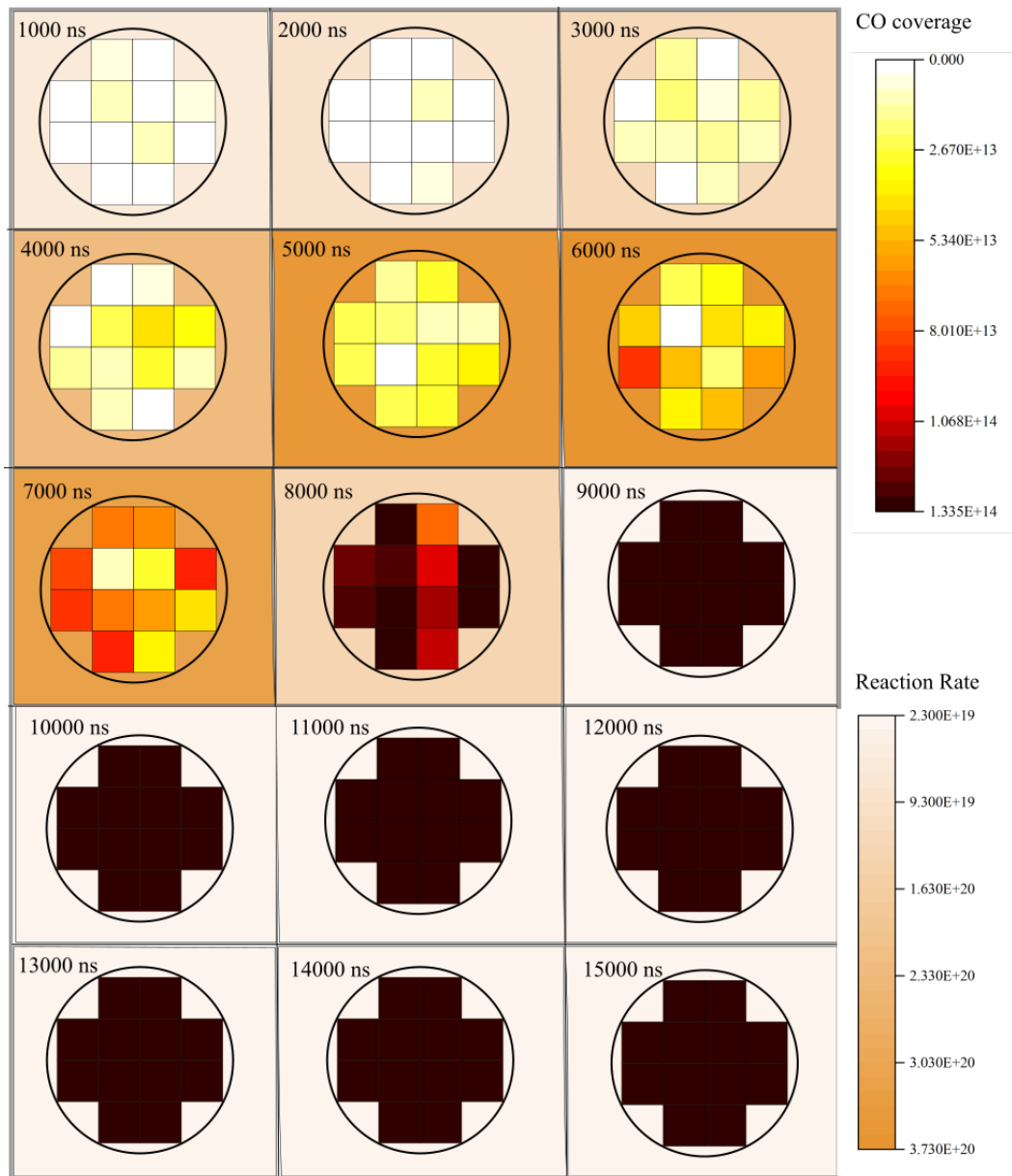


**Fig. 4.30.:** Local CO coverage on a single Pd particle at different time steps. The background shows the mean reaction rate across the entire particle. Here, the 6<sup>th</sup> particle from the inlet is shown at  $T = 523$  K from  $t = 1000$  to  $15000$  ns. As the CO coverage increases with time, the reaction rate increases and then reduces as CO adsorption dominates.  $\theta_{CO} = 0.1$ ,  $k_{CO} = 0.95$

## 4.3 Summary

In this work, a DSMC simulation is presented with a surface reaction model. A new clustering method is implemented to achieve a discrete model with prescribed accuracy and a reduced computational effort. The combination has successfully predicted gas concentration when compared to experimental results. Beyond that, DSMC provides precise insights into the kinetics of the individual parts of a reactor. DSMC is able to simulate rarefied gas flows in the reactor and also preserve the kinetics and transport phenomena at a molecular level.

## Conclusion

A descriptive simulation is presented for surface reactions, in this case, a simple bimolecular reaction, CO oxidation on Pd (which can always be extended to other noble metal catalysts). It could be extended to simulate chain reactions often seen in industrial applications such as low temperature gold-catalyzed water gas shift reaction [114, 115], methanol production used in methanol fuel cell [116, 117] and many more. Be it multiple shelled hollow nanospheres [118] or carbon nanotubes [119] for applications in chemical industries or porous microfluidic channels in microelectromechanical systems, systems are being shrunk to smaller sizes to reduce global footprint and waste and turn towards greener solutions. DSMC provides a wonderful solution to have more insights into the gas flow in such newly developed catalysts prior to scaling up. A model is designed in DSMC to simulate surface reactions such as CO oxidation on porous Pd. The model has then been modified with a variable parcel algorithm. The variable parcel method allows us to represent any number of real gas molecules in one simulated molecule. This modification makes it easy to represent gases in low and high concentration in different parcel sizes to conserve all local data, which is the biggest advantage of a DSMC simulation. This reduces the computational effort and thus makes the simulation more useful. Elementary steps of diffusion, adsorption, desorption and reaction are modified accordingly. Parcels colliding with the surface may adsorb. Adjacent adsorbed molecules of CO and O undergo reaction following Langmuir-Hinshelwood mechanism. The product CO<sub>2</sub> is immediately desorbed. Adsorbed CO and O are desorbed into the gas phase in parcels when sufficient desorption energy is available. The parcels are provided with a new velocity based on the temperature of the surface from a Maxwellian distribution.

To validate the model, experimental results are sought from CO oxidation in nanofluidic channels with Pd nanoparticles embedded in it [105]. The gas outlet concentration is monitored with gas spectrophotometer and the inlet is controlled using flow controllers. Results from the DSMC simulation agreed well with the experimental results. It could also handle temperature variation in the nanofluidic channels. Doing an extensive sensitivity analysis on all the input parameters of the simulation provided us with an opportunity to adjust the parameters in an order of influence on the output. All the input parameters changed to match with the experiments could

be then successfully explained. One example is the final parameter value reached for activation energy, which was 50 kJ/mol. According to literature study, such activation energies are seen for polycrystalline Pd. Without having the prior knowledge of the type of surface of Pd, it was possible to determine it. The experiments had also predicted polycrystalline structure for the embedded Pd. Another example is the introduction of a new parameter,  $k_{CO}$ . This parameter represents a reduction in the effect of O adsorption inhibition on surface covered with CO and it reduces with temperature. Physically, any adsorbed molecules on the surface diffuse more with increase in temperature. For a surface covered with CO (up to saturation values), it would mean that CO molecules can hop to other vacant sites thereby reducing the inhibition effect on any O adsorption. Apart from this, DSMC has the unique ability to preserve local data. Having already shown that, it is possible to adequately present the chemical kinetics, it is also shown that DSMC is able to provide local mass transport data. Local gas concentrations, surface coverage, reaction rates could be easily calculated from the DSMC data. From the local data, regions of the nanofluidic channels could be identified that showed maximum reactivity. Sections of the channel could be identified that showed complete CO poisoning. Since the model worked well with temperatures, it was possible to identify maximum yield conditions. This provision of local data is what makes the model so lucrative. It opens up avenues for simulating such nanoreactor systems without loss of data. Despite the arguably high computational expense of DSMC, which the author has tried to manage with the variable parcel method, it provides insight into reactors that would be unavailable to present-day experimental techniques. The reaction kinetics are hitherto unknown as the timescale of the formation of intermediates is as small as a few picoseconds [120]. As it is shown in this work, DSMC is capable of handling local data at small timesteps. It would be possible to test out hypotheses for reaction mechanisms and compare the experimental and simulation results to determine the correct hypothesis.

## 5.1 Future Work

Given the unique abilities of the presented DSMC surface model, it has many areas that can be worked on to suit particular research objectives in mind. One fundamental aspect that is neglected in implementation of the current setup is the thermodynamics. Heat transfer effects are neglected to keep the understanding only to fundamentals of mass transfer. It is the author's wish that the simulation model be now extended to include thermal conductivity and heat of reactions in the

surface reaction. Many boundary condition solutions have been proposed [121–123] to model adiabatic wall conditions. If such boundary conditions were enforced on the catalyst surfaces, it would open up possibilities to simulate bifurcation and oscillatory reactions (often observed with Pd, Pt and Ru catalysts), endothermic and exothermic reactions and heat (de)activated catalysts.

In the model, a new parameter is introduced that defines surface diffusion with a single number while neglecting the surface diffusion process itself. It would be interesting to integrate the diffusion process, as seen in Kinetic Monte Carlo simulations along with the gas phase simulations. Hori et al. have proposed a method of incorporating surface diffusion along side gas phase diffusion [124]. They assume an isotropic distribution of distance an adsorbed molecule can diffuse through depending on the surface residence time. They have concluded that the gas phase diffusion was enhanced due to surface diffusion in their ideal pore system. Thus, it may be worthwhile to show surface diffusion in gas flows in Knudsen regime where the diffusion coefficient is tentative.

With a method like DSMC, unlike any other molecular models, it is open to millions of possibilities. With a specific research objective in mind, DSMC can be modified in as many ways as possible. Here, one specific application of DSMC is shown related to surface reactions in mesoporous systems. Bearing in mind that DSMC was originally developed to simulate gas flows around huge spaceships, it certainly has a wide range of applications.



# Bibliography

- [1] Daya R Varma, Shree Mulay, and Sylvain Chemtob. “Carbon monoxide: from public health risk to painless killer”. In: *Handbook of toxicology of chemical warfare agents*. Elsevier, 2009, pp. 271–292 (cit. on p. 2).
- [2] T. Engel and G. Ertl. “A molecular beam investigation of the catalytic oxidation of CO on Pd (111)”. In: *The Journal of Chemical Physics* 69.3 (1978), pp. 1267–1281 (cit. on pp. 4, 6–9, 44, 48, 53, 91).
- [3] T. Engel and G. Ertl. “Elementary Steps in the Catalytic Oxidation of Carbon Monoxide on Platinum Metals”. In: *Advances in Catalysis*. Ed. by D. D. Eley, Herman Pines, and Paul B. Weez. Vol. 28. Academic Press, 1979, pp. 1–78 (cit. on pp. 4, 6, 8, 9, 44, 75).
- [4] H. Conrad, G. Ertl, and J. Küppers. “Interactions between oxygen and carbon monoxide on a Pd(111) surface”. In: *Surface Science* 76.2 (1978), pp. 323–342 (cit. on pp. 4, 6–8, 46, 47, 53, 75).
- [5] F. Gao, Y. Wang, Y. Cai, and D. W. Goodman. “CO Oxidation on Pt-Group Metals from Ultrahigh Vacuum to Near Atmospheric Pressures. 2. Palladium and Platinum”. In: *The Journal of Physical Chemistry C* 113.1 (2009), pp. 174–181 (cit. on pp. 4, 6, 8, 9).
- [6] You Zhou, Zongyuan Wang, and Changjun Liu. “Perspective on CO oxidation over Pd-based catalysts”. In: *Catalysis Science & Technology* 5.1 (2015), pp. 69–81 (cit. on p. 4).
- [7] V. Bratan, C. Munteanu, C. Hornoiu, et al. “CO oxidation over Pd supported catalysts —In situ study of the electric and catalytic properties”. In: *Applied Catalysis B: Environmental* 207 (2017), pp. 166–173 (cit. on p. 4).
- [8] Xuefei Weng, Xiang Yuan, Huan Li, et al. “The study of the active surface for CO oxidation over supported Pd catalysts”. In: *Science China Chemistry* 58.1 (2015), pp. 174–179 (cit. on p. 4).
- [9] M. S. Chen, Y. Cai, Z. Yan, et al. “Highly active surfaces for CO oxidation on Rh, Pd, and Pt”. In: *Surface Science* 601.23 (2007), pp. 5326–5331 (cit. on pp. 4, 6–8).
- [10] P. J. Berlowitz, C. H. F. Peden, and D. W. Goodman. “Kinetics of carbon monoxide oxidation on single-crystal palladium, platinum, and iridium”. In: *The Journal of Physical Chemistry* 92.18 (1988), pp. 5213–5221 (cit. on pp. 4, 6, 8, 9).
- [11] Janos Szanyi and D. Wayne Goodman. “CO oxidation on palladium. 1. A combined kinetic-infrared reflection absorption spectroscopic study of Pd (100)”. In: *The Journal of Physical Chemistry* 98.11 (1994), pp. 2972–2977 (cit. on pp. 4, 6–8).

- [12] S. Blomberg, J. Zetterberg, J. Gustafson, et al. “Comparison of AP-XPS and PLIF Measurements During CO Oxidation Over Pd Single Crystals”. In: *Topics in Catalysis* 59.5 (2016), pp. 478–486 (cit. on pp. 4, 6).
- [13] T. Matsushima, D. B. Almy, D. C. Foyt, J. S. Close, and J. M. White. “On the mechanism and kinetics of the CO-oxidation reaction on polycrystalline palladium: II. The kinetics”. In: *Journal of Catalysis* 39.2 (1975), pp. 277–285 (cit. on pp. 4, 6, 8, 9, 44).
- [14] T. Matsushima and J. M. White. “On the mechanism and kinetics of the CO-oxidation reaction on polycrystalline palladium: I. The reaction paths”. In: *Journal of Catalysis* 39.2 (1975), pp. 265–276 (cit. on pp. 4, 6, 8, 9, 44).
- [15] Xingcai Guo, Alon Hoffman, and John T. Yates. “Adsorption kinetics and isotopic equilibration of oxygen adsorbed on the Pd(111) surface”. In: *The Journal of Chemical Physics* 90.10 (1989), pp. 5787–5792 (cit. on pp. 4, 6, 9, 51–53, 76).
- [16] Mingshi Jin, Jung-Nam Park, Jeong Kuk Shon, et al. “Low temperature CO oxidation over Pd catalysts supported on highly ordered mesoporous metal oxides”. In: *Catalysis Today* 185.1 (2012), pp. 183–190 (cit. on p. 4).
- [17] Jutta Rogal, Karsten Reuter, and Matthias Scheffler. “First-principles statistical mechanics study of the stability of a subnanometer thin surface oxide in reactive environments: CO oxidation at Pd (100)”. In: *Physical review letters* 98.4 (2007), p. 046101 (cit. on pp. 5, 17, 19).
- [18] Jutta Rogal, Karsten Reuter, and Matthias Scheffler. “CO oxidation at Pd (100): A first-principles constrained thermodynamics study”. In: *Physical Review B* 75.20 (2007), p. 205433 (cit. on pp. 5, 17, 19).
- [19] Jutta Rogal, Karsten Reuter, and Matthias Scheffler. “CO oxidation on Pd(100) at technologically relevant pressure conditions: First-principles kinetic Monte Carlo study”. In: *Physical Review B* 77.15 (2008), p. 155410 (cit. on pp. 5, 17, 19, 20, 23).
- [20] P. Salo, K. Honkala, M. Alatalo, and K. Laasonen. “Catalytic oxidation of CO on Pd(111)”. In: *Surface Science* 516.3 (2002), pp. 247–253 (cit. on pp. 5, 8, 17, 19).
- [21] Mehdi D Esrafil and Soheila Asadollahi. “Exploring different reaction mechanisms for oxidation of CO over a single Pd atom incorporated nitrogen-doped graphene: a DFT study”. In: *Applied Surface Science* 463 (2019), pp. 526–534 (cit. on pp. 5, 18, 19).
- [22] Yingzhi Li, Yue Yu, Jian-Guo Wang, et al. “CO oxidation over graphene supported palladium catalyst”. In: *Applied Catalysis B: Environmental* 125 (2012), pp. 189–196 (cit. on pp. 5, 17, 19).
- [23] Da-Jiang Liu and JW Evans. “Atomistic and multiscale modeling of CO-oxidation on Pd (1 0 0) and Rh (1 0 0): From nanoscale fluctuations to mesoscale reaction fronts”. In: *Surface science* 603.10-12 (2009), pp. 1706–1716 (cit. on pp. 5, 21).

- [24] EI Latkin, VI Elokhin, AV Matveev, and VV Gorodetskii. “The role of subsurface oxygen in oscillatory behaviour of CO+ O<sub>2</sub> reaction over Pd metal catalysts: Monte Carlo model”. In: *Journal of Molecular Catalysis A: Chemical* 158.1 (2000), pp. 161–166 (cit. on pp. 5, 22).
- [25] S Ladas, R Imbihl, and G Ertl. “Kinetic oscillations during the catalytic CO oxidation on Pd (110): the role of subsurface oxygen”. In: *Surface science* 219.1-2 (1989), pp. 88–106 (cit. on pp. 5, 22).
- [26] CJ Zhang and P Hu. “CO oxidation on Pd (100) and Pd (111): A comparative study of reaction pathways and reactivity at low and medium coverages”. In: *Journal of the American Chemical Society* 123.6 (2001), pp. 1166–1172 (cit. on pp. 5, 16, 19).
- [27] G Zheng and EI Altman. “The reactivity of surface oxygen phases on Pd (100) toward reduction by CO”. In: *The Journal of Physical Chemistry B* 106.5 (2002), pp. 1048–1057 (cit. on pp. 5, 8).
- [28] Lothar Kunz, Frank M Kuhn, and Olaf Deutschmann. “Kinetic Monte Carlo simulations of surface reactions on supported nanoparticles: A novel approach and computer code”. In: *The Journal of Chemical Physics* 143.4 (2015), p. 044108 (cit. on pp. 5, 19, 23, 24).
- [29] Simone Piccinin and Michail Stamatakis. “CO oxidation on Pd (111): a first-principles-based kinetic Monte Carlo study”. In: *Acs Catalysis* 4.7 (2014), pp. 2143–2152 (cit. on pp. 5, 19, 21).
- [30] Zhiyao Duan and Graeme Henkelman. “CO oxidation on the Pd (111) surface”. In: *Acs Catalysis* 4.10 (2014), pp. 3435–3443 (cit. on pp. 5, 18).
- [31] AV Matveev, EI Latkin, VI Elokhin, and VV Gorodetskii. “Turbulent and stripes wave patterns caused by limited COads diffusion during CO oxidation over Pd (1 1 0) surface: kinetic Monte Carlo studies”. In: *Chemical Engineering Journal* 107.1-3 (2005), pp. 181–189 (cit. on pp. 5, 22).
- [32] Xingcai Guo and John T. Yates. “Dependence of effective desorption kinetic parameters on surface coverage and adsorption temperature: CO on Pd(111)”. In: *The Journal of Chemical Physics* 90.11 (1989), pp. 6761–6766 (cit. on pp. 6, 51–53).
- [33] E. M. Stuve, R. J. Madix, and C. R. Brundle. “CO oxidation on Pd(100): A study of the coadsorption of oxygen and carbon monoxide”. In: *Surface Science* 146.1 (1984), pp. 155–178 (cit. on pp. 6–8, 75).
- [34] R. J. Behm, K. Christmann, G. Ertl, and M. A. Van Hove. “Adsorption of CO on Pd(100)”. In: *The Journal of Chemical Physics* 73.6 (1980), pp. 2984–2995 (cit. on p. 6).
- [35] J. R. Creighton, F. H. Tseng, J. M. White, and J. S. Turner. “Numerical modeling of steady-state carbon monoxide oxidation on platinum and palladium”. In: *The Journal of Physical Chemistry* 85.6 (1981), pp. 703–708 (cit. on pp. 9, 44, 51, 185).
- [36] Hendrik Gossler, Lubow Maier, Sofia Angeli, Steffen Tischer, and Olaf Deutschmann. “CaRMEN: An Improved Computer-Aided Method for Developing Catalytic Reaction Mechanisms”. In: *Catalysts* 9.3 (2019), p. 227 (cit. on p. 10).

- [37] A. B. Bortz, M. H. Kalos, and J. L. Lebowitz. “A new algorithm for Monte Carlo simulation of Ising spin systems”. In: *Journal of Computational Physics* 17.1 (1975), pp. 10–18 (cit. on p. 11).
- [38] Frerich J. Keil. “Molecular Modelling for Reactor Design”. In: *Annual Review of Chemical and Biomolecular Engineering* 9.1 (2018), pp. 201–227 (cit. on p. 11).
- [39] Michail Stamatakis. “Kinetic modelling of heterogeneous catalytic systems”. In: *Journal of Physics: Condensed Matter* 27.1 (2014), p. 013001 (cit. on pp. 11, 20).
- [40] J. A. Elliot. “Introduction to Multiscale Modelling of Materials”. In: *Multiscale Modelling Methods for Applications in Materials Science* 19 (2013), pp. 1–20 (cit. on p. 11).
- [41] Nicholas Metropolis and S. Ulam. “The Monte Carlo Method”. In: *Journal of the American Statistical Association* 44.247 (1949), pp. 335–341 (cit. on p. 12).
- [42] B. J. Alder and T. E. Wainwright. “Studies in Molecular Dynamics. I. General Method”. In: *The Journal of Chemical Physics* 31.2 (1959), pp. 459–466 (cit. on p. 13).
- [43] William Lauchlin McMillan. “Ground state of liquid He 4”. In: *Physical Review* 138.2A (1965), A442 (cit. on p. 13).
- [44] Moti Lal. “Monte Carlo computer simulation of chain molecules. I”. In: *Molecular physics* 17.1 (1969), pp. 57–64 (cit. on p. 13).
- [45] Farouq Ahmed, Ryo Nagumo, Ryuji Miura, et al. “CO oxidation and NO reduction on a MgO (100) supported Pd cluster: A quantum chemical molecular dynamics study”. In: *The Journal of Physical Chemistry C* 115.49 (2011), pp. 24123–24132 (cit. on p. 14).
- [46] W. Kohn, A. D. Becke, and R. G. Parr. “Density Functional Theory of Electronic Structure”. In: *The Journal of Physical Chemistry* 100.31 (1996), pp. 12974–12980 (cit. on p. 16).
- [47] John P. Perdew, Kieron Burke, and Matthias Ernzerhof. “Generalized Gradient Approximation Made Simple”. In: *Physical Review Letters* 77.18 (1996), pp. 3865–3868 (cit. on p. 16).
- [48] A. D. Becke. “Density-functional thermochemistry. V. Systematic optimization of exchange-correlation functionals”. In: *The Journal of Chemical Physics* 107.20 (1997), pp. 8554–8560 (cit. on p. 16).
- [49] R. O. Jones and O. Gunnarsson. “The density functional formalism, its applications and prospects”. In: *Reviews of Modern Physics* 61.3 (1989), pp. 689–746 (cit. on p. 16).
- [50] Aron J. Cohen, Paula Mori-Sánchez, and Weitao Yang. “Insights into Current Limitations of Density Functional Theory”. In: *Science* 321.5890 (2008), p. 792 (cit. on p. 16).

- [51] Yoyo Hinuma, Hiroyuki Hayashi, Yu Kumagai, Isao Tanaka, and Fumiyasu Oba. “Comparison of approximations in density functional theory calculations: Energetics and structure of binary oxides”. In: *Physical Review B* 96.9 (2017). PRB, p. 094102 (cit. on pp. 16, 19).
- [52] Diana Vogel, Christian Spiel, Yuri Suchorski, et al. “Local Catalytic Ignition during CO Oxidation on Low-Index Pt and Pd Surfaces: A Combined PEEM, MS, and DFT Study”. In: *Angewandte Chemie International Edition* 51.40 (2012), pp. 10041–10044 (cit. on p. 18).
- [53] Simone Piccinin and Michail Stamatakis. “Steady-state co oxidation on pd (111): first-principles kinetic monte carlo simulations and microkinetic analysis”. In: *Topics in Catalysis* 60.1-2 (2017), pp. 141–151 (cit. on pp. 19, 21).
- [54] R. Car and M. Parrinello. “Unified Approach for Molecular Dynamics and Density-Functional Theory”. In: *Physical Review Letters* 55.22 (1985). PRL, pp. 2471–2474 (cit. on p. 19).
- [55] H Lee Woodcock III, Milan Hodošček, Andrew TB Gilbert, et al. “Interfacing Q-Chem and CHARMM to perform QM/MM reaction path calculations”. In: *Journal of computational chemistry* 28.9 (2007), pp. 1485–1502 (cit. on p. 19).
- [56] Feliu Maseras and Keiji Morokuma. “IMOMM: A new integrated ab initio + molecular mechanics geometry optimization scheme of equilibrium structures and transition states”. In: *Journal of Computational Chemistry* 16.9 (1995), pp. 1170–1179 (cit. on p. 19).
- [57] Thom Vreven, K. Suzie Byun, István Komáromi, et al. “Combining Quantum Mechanics Methods with Molecular Mechanics Methods in ONIOM”. In: *Journal of Chemical Theory and Computation* 2.3 (2006), pp. 815–826 (cit. on p. 19).
- [58] Sebastian Matera and Karsten Reuter. “First-Principles Approach to Heat and Mass Transfer Effects in Model Catalyst Studies”. In: *Catalysis Letters* 133.1 (2009), p. 156 (cit. on p. 23).
- [59] Sebastian Matera and Karsten Reuter. “Transport limitations and bistability for in situ CO oxidation at RuO<sub>2</sub>(110): First-principles based multiscale modeling”. In: *Physical Review B* 82.8 (2010), p. 085446 (cit. on p. 23).
- [60] Karsten Reuter. *Insight into a Pressure and Materials Gap: CO Oxidation at "Ruthenium" Catalysts*. Vol. 61. 2006, pp. 471–477 (cit. on p. 23).
- [61] Matthew Neurock and Eric W. Hansen. “First-principles-based molecular simulation of heterogeneous catalytic surface chemistry”. In: *Computers & Chemical Engineering* 22 (1998), S1045–S1060 (cit. on p. 23).
- [62] Eric W. Hansen and Matthew Neurock. “Modeling surface kinetics with first-principles-based molecular simulation”. In: *Chemical Engineering Science* 54.15 (1999), pp. 3411–3421 (cit. on p. 23).
- [63] Eric Hansen and Matthew Neurock. “Predicting lateral surface interactions through density functional theory: application to oxygen on Rh(100)”. In: *Surface Science* 441.2 (1999), pp. 410–424 (cit. on p. 23).

- [64] Graeme Henkelman and Hannes Jónsson. “Long time scale kinetic Monte Carlo simulations without lattice approximation and predefined event table”. In: *The Journal of Chemical Physics* 115.21 (2001), pp. 9657–9666 (cit. on p. 23).
- [65] C. Domain, C. S. Becquart, and L. Malerba. “Simulation of radiation damage in Fe alloys: an object kinetic Monte Carlo approach”. In: *Journal of Nuclear Materials* 335.1 (2004), pp. 121–145 (cit. on p. 23).
- [66] Arthur F. Voter. “INTRODUCTION TO THE KINETIC MONTE CARLO METHOD”. In: *Radiation Effects in Solids*. Ed. by Kurt E. Sickafus, Eugene A. Kotomin, and Blas P. Uberuaga. Springer Netherlands, pp. 1–23 (cit. on p. 24).
- [67] G. A. Bird. *Molecular Gas Dynamics and the Direct Simulation of Gas Flows*. New York: Clarendon Press, Oxford University Press Inc., 1994 (cit. on pp. 26, 27, 36, 39–43, 55, 57, 59, 183).
- [68] GA Bird. “Chemical reactions in DSMC”. In: *AIP Conference Proceedings*. Vol. 1333. 1. American Institute of Physics. 2011, pp. 1195–1202 (cit. on pp. 27–29).
- [69] Michael N Macrossan and Charles R Lilley. “Modified generalized hard sphere collision model for direct simulation Monte Carlo calculations”. In: *Journal of thermophysics and heat transfer* 17.2 (2003), pp. 289–291 (cit. on p. 27).
- [70] Sergey Gimelshein and Ingrid Wysong. “DSMC modeling of flows with recombination reactions”. In: *Physics of Fluids* 29.6 (2017), p. 067106 (cit. on p. 28).
- [71] SF Gimelshein, DA Levin, and RJ Collins. “Modeling of glow radiation in the rarefied flow about an orbiting spacecraft”. In: *Journal of Thermophysics and Heat transfer* 14.4 (2000), pp. 471–479 (cit. on p. 28).
- [72] S. Ivanov M and V. Rogasinsky S. *Analysis of numerical techniques of the direct simulation Monte Carlo method in the rarefied gas dynamics*. Generic. 1988 (cit. on p. 28).
- [73] Isabelle Choquet. “A new approach to model and simulate numerically surface chemistry in rarefied flows”. In: *Physics of Fluids* 11.6 (1999), pp. 1650–1661 (cit. on p. 28).
- [74] A. N. Molchanova, A. V. Kashkovsky, and Y. A. Bondar. “A detailed DSMC surface chemistry model”. In: *AIP Conference Proceedings*. Vol. 1628, pp. 131–138 (cit. on p. 28).
- [75] AN Molchanova, AV Kashkovsky, and Ye A Bondar. “A detailed DSMC surface chemistry model”. In: *AIP Conference Proceedings*. Vol. 1628. 1. American Institute of Physics. 2014, pp. 131–138 (cit. on p. 29).
- [76] Alexandra N Molchanova, Alexander V Kashkovsky, and Yevgeniy A Bondar. “Surface recombination in the direct simulation Monte Carlo method”. In: *Physics of Fluids* 30.10 (2018), p. 107105 (cit. on p. 29).
- [77] Jochen A. H. Dreyer, Norbert Riefler, Georg R. Pesch, et al. “Simulation of gas diffusion in highly porous nanostructures by direct simulation Monte Carlo”. In: *Chemical Engineering Science* 105 (2014), pp. 69–76 (cit. on pp. 29, 44, 55, 58, 89, 183).

- [78] Georg R. Pesch, Norbert Riefler, Udo Fritsching, Lucio Colombi Ciacchi, and Lutz Mädler. “Gas-solid catalytic reactions with an extended DSMC model”. In: *AIChE Journal* 61.7 (2015), pp. 2092–2103 (cit. on pp. 29, 30, 32, 44–46, 48, 50, 52, 55, 57, 71, 74, 76, 79, 183, 187).
- [79] G. A. Bird. “Recent advances and current challenges for DSMC”. In: *Computers & Mathematics with Applications* 35.1 (1998), pp. 1–14 (cit. on p. 55).
- [80] Zhi-Xin Sun, Zhen Tang, Ya-Ling He, and Wen-Quan Tao. “Proper cell dimension and number of particles per cell for DSMC”. In: *Computers & Fluids* 50.1 (2011), pp. 1–9 (cit. on p. 183).
- [81] G. A. Bird. “Sophisticated dsmc”. In:
- [82] C. Shu. “Particle number per cell and scaling factor effect on accuracy of DSMC simulation of micro flows”. In: *International Journal of Numerical Methods for Heat & Fluid Flow* 15.8 (2005), pp. 827–841 (cit. on p. 183).
- [83] F. J. Alexander, A. L. Garcia, and B. J. Alder. “The consistent Boltzmann algorithm for the van der Waals equation of state”. In: *Physica A: Statistical Mechanics and its Applications* 240.1 (1997), pp. 196–201.
- [84] F. J. Alexander, A. L. Garcia, and B. J. Alder. “A Consistent Boltzmann Algorithm”. In: *Physical Review Letters* 74.26 (1995). PRL, pp. 5212–5215.
- [85] Rui Chen, Ramesh Agarwal, Felix Cheremisin, and Y. Bondar. “A comparative study of Navier-Stokes, Burnett, DSMC, and Boltzmann solutions for hypersonic flow past 2-D bodies”. In: p. 205.
- [86] Joachim Fritzsche, David Albinsson, Michael Fritzsche, et al. “Single particle nanoplasmonic sensing in individual nanofluidic channels”. In: *Nano letters* 16.12 (2016), pp. 7857–7864 (cit. on p. 30).
- [87] Kosuke Sugawa, Hironobu Tahara, Ayane Yamashita, et al. “Refractive index susceptibility of the plasmonic palladium nanoparticle: potential as the third plasmonic sensing material”. In: *Acs Nano* 9.2 (2015), pp. 1895–1904 (cit. on p. 30).
- [88] David P. Schmidt and C. J. Rutland. “A New Droplet Collision Algorithm”. In: *Journal of Computational Physics* 164.1 (2000), pp. 62–80 (cit. on pp. 31, 59, 61).
- [89] K. Nanbu. “Probability theory of electron-molecule, ion-molecule, molecule-molecule, and Coulomb collisions for particle modeling of materials processing plasmas and cases”. In: *IEEE Transactions on Plasma Science* 28.3 (2000), pp. 971–990 (cit. on pp. 31, 60).
- [90] Katsuhisa Koura and Hiroaki Matsumoto. “Variable soft sphere molecular model for air species”. In: *Physics of Fluids A: Fluid Dynamics* 4.5 (1992), pp. 1083–1085 (cit. on pp. 39, 40, 179).
- [91] P. S. Prasanth and Jose K. Kakkassery. “Molecular models for simulation of rarefied gas flows using direct simulation Monte Carlo method”. In: *Fluid Dynamics Research* 40.4 (2008), pp. 233–252 (cit. on pp. 40, 179).

- [92] Thomas Scanlon, Ehsan Roohi, Craig White, Masoud Darbandi, and Jason Reese. “An open source, parallel DSMC code for rarefied gas flows in arbitrary geometries”. In: *Computers & Fluids* 39 (2010), pp. 2078–2089 (cit. on pp. 44, 55, 58).
- [93] Rodrigo C. Palharini, Craig White, Thomas J. Scanlon, et al. “Benchmark numerical simulations of rarefied non-reacting gas flows using an open-source DSMC code”. In: *Computers & Fluids* 120 (2015), pp. 140–157 (cit. on pp. 44, 55, 58).
- [94] P. Kisliuk. “The sticking probabilities of gases chemisorbed on the surfaces of solids”. In: *Journal of Physics and Chemistry of Solids* 3.1 (1957), pp. 95–101 (cit. on pp. 44, 47, 55, 186).
- [95] P. Kisliuk. “The sticking probabilities of gases chemisorbed on the surfaces of solids—II”. In: *Journal of Physics and Chemistry of Solids* 5.1 (1958), pp. 78–84 (cit. on pp. 44, 47, 55, 186).
- [96] K. W. Kolasinski. *Surface Science: Fundamentals of catalysis and nanoscience*. 3rd. United Kingdom: John Wiley & Sons Ltd, 2012 (cit. on pp. 44, 49, 51, 53, 55).
- [97] Irving Langmuir. “The mechanism of the catalytic action of platinum in the reactions  $2\text{CO} + \text{O}_2 = 2\text{CO}_2$  and  $2\text{H}_2 + \text{O}_2 = 2\text{H}_2\text{O}$ ”. In: *Transactions of the Faraday Society* 17 (1922), pp. 621–654 (cit. on p. 49).
- [98] Isabel Z. Jones, Roger A. Bennett, and Michael Bowker. “CO oxidation on Pd(110): a high-resolution XPS and molecular beam study”. In: *Surface Science* 439.1 (1999), pp. 235–248 (cit. on pp. 51, 185).
- [99] Cyril Norman Hinshelwood and John William Nicholson. “The kinetics of the interaction of nitrous oxide and hydrogen”. In: *Proceedings of the Royal Society of London. Series A, Containing Papers of a Mathematical and Physical Character* 106.737 (1924), pp. 292–298 (cit. on p. 55).
- [100] L. Mädler, H. K. Kammler, R. Mueller, and S. E. Pratsinis. “Controlled synthesis of nanostructured particles by flame spray pyrolysis”. In: *Journal of Aerosol Science* 33.2 (2002), pp. 369–389 (cit. on p. 58).
- [101] Woosuck Hong, Donald H House, and John Keyser. “Adaptive particles for incompressible fluid simulation”. In: *The Visual Computer* 24.7-9 (2008), pp. 535–543 (cit. on p. 63).
- [102] Bart Adams, Mark Pauly, Richard Keiser, and Leonidas J Guibas. “Adaptively sampled particle fluids”. In: *ACM SIGGRAPH 2007 papers*. 2007, 48–es (cit. on p. 63).
- [103] Marcel Pfeiffer and M Hossein Gorji. “Adaptive particle–cell algorithm for Fokker–Planck based rarefied gas flow simulations”. In: *Computer Physics Communications* 213 (2017), pp. 1–8 (cit. on p. 63).
- [104] Robert Scott Martin and Jean-Luc Cambier. “Octree particle management for DSMC and PIC simulations”. In: *Journal of Computational Physics* 327 (2016), pp. 943–966 (cit. on p. 63).
- [105] David Albinsson, Stephan Bartling, Sara Nilsson, et al. “Operando detection of single nanoparticle activity dynamics inside a model pore catalyst material”. In: *Science Advances* 6.25 (2020), eaba7678 (cit. on pp. 71, 73, 130, 140, 150).

- [106] Christoph Langhammer, Zhe Yuan, Igor Zorić, and Bengt Kasemo. “Plasmonic Properties of Supported Pt and Pd Nanostructures”. In: *Nano Letters* 6.4 (2006), pp. 833–838 (cit. on p. 72).
- [107] Christoph Langhammer, Bengt Kasemo, and Igor Zorić. “Absorption and scattering of light by Pt, Pd, Ag, and Au nanodisks: Absolute cross sections and branching ratios”. In: *The Journal of Chemical Physics* 126.19 (2007), p. 194702 (cit. on p. 72).
- [108] Su Liu, Arturo Susarrey Arce, Sara Nilsson, et al. “In Situ Plasmonic Nanospectroscopy of the CO Oxidation Reaction over Single Pt Nanoparticles”. In: *ACS Nano* 13.5 (2019), pp. 6090–6100 (cit. on p. 72).
- [109] Svetlana Alekseeva, Alice Bastos da Silva Fanta, Beniamino Iandolo, et al. “Grain boundary mediated hydriding phase transformations in individual polycrystalline metal nanoparticles”. In: *Nature communications* 8.1 (2017), pp. 1–10 (cit. on p. 72).
- [110] Yi Zhou, Jianguo Liu, Jilei Ye, et al. “Poisoning and regeneration of Pd catalyst in direct formic acid fuel cell”. In: *Electrochimica Acta* 55.17 (2010), pp. 5024–5027 (cit. on p. 91).
- [111] Ryo Toyoshima, Masaaki Yoshida, Yuji Monya, et al. “Active surface oxygen for catalytic CO oxidation on Pd (100) proceeding under near ambient pressure conditions”. In: *The Journal of Physical Chemistry Letters* 3.21 (2012), pp. 3182–3187 (cit. on p. 91).
- [112] M Šnábl, O Borusik, VVCB Cháb, et al. “Surface diffusion of CO molecules on Pd {111} studied with photoelectron emission microscopy”. In: *Surface science* 385.2-3 (1997), pp. L1016–L1022 (cit. on p. 140).
- [113] H-P Kaukonen and Risto M Nieminen. “Computer simulations studies of the catalytic oxidation of carbon monoxide on platinum metals”. In: *The Journal of chemical physics* 91.7 (1989), pp. 4380–4386 (cit. on p. 140).
- [114] James H Carter and Graham J Hutchings. “Recent advances in the gold-catalysed low-temperature water–gas shift reaction”. In: *Catalysts* 8.12 (2018), p. 627 (cit. on p. 149).
- [115] Vasko Idakiev, Z-Y Yuan, T Tabakova, and B-L Su. “Titanium oxide nanotubes as supports of nano-sized gold catalysts for low temperature water-gas shift reaction”. In: *Applied Catalysis A: General* 281.1-2 (2005), pp. 149–155 (cit. on p. 149).
- [116] Sahriah Basri, SK Kamarudin, WRW Daud, and Z Yaakub. “Nanocatalyst for direct methanol fuel cell (DMFC)”. In: *International Journal of Hydrogen Energy* 35.15 (2010), pp. 7957–7970 (cit. on p. 149).
- [117] Jin Qu, Xiwen Zhou, Feng Xu, Xue-Qing Gong, and Shik Chi Edman Tsang. “Shape effect of Pd-promoted Ga<sub>2</sub>O<sub>3</sub> nanocatalysts for methanol synthesis by CO<sub>2</sub> hydrogenation”. In: *The Journal of Physical Chemistry C* 118.42 (2014), pp. 24452–24466 (cit. on p. 149).

- [118] Xiaoyong Lai, Jonathan E Halpert, and Dan Wang. “Recent advances in micro-/nano-structured hollow spheres for energy applications: From simple to complex systems”. In: *Energy & Environmental Science* 5.2 (2012), pp. 5604–5618 (cit. on p. 149).
- [119] Yibo Yan, Jianwei Miao, Zhihong Yang, et al. “Carbon nanotube catalysts: recent advances in synthesis, characterization and applications”. In: *Chemical Society Reviews* 44.10 (2015), pp. 3295–3346 (cit. on p. 149).
- [120] Lenka Hannevold, Ola Nilsen, Arne Kjekshus, and Helmer Fjellvåg. “Reconstruction of platinum–rhodium catalysts during oxidation of ammonia”. In: *Applied Catalysis A: General* 284.1-2 (2005), pp. 163–176 (cit. on p. 152).
- [121] Alireza Mohammadzadeh, Anirudh Rana, and Henning Struchtrup. “DSMC and R13 modeling of the adiabatic surface”. In: *International Journal of Thermal Sciences* 101 (2016), pp. 9–23 (cit. on p. 152).
- [122] Qiuwang Wang, Xiaohong Yan, and Qunwu He. “Heat-flux-specified boundary treatment for gas flow and heat transfer in microchannel using direct simulation Monte Carlo method”. In: *International journal for numerical methods in engineering* 74.7 (2008), pp. 1109–1127 (cit. on p. 152).
- [123] Hassan Akhlaghi, Ehsan Roohi, and Stefan Stefanov. “A new iterative wall heat flux specifying technique in DSMC for heating/cooling simulations of MEMS/NEMS”. In: *International Journal of Thermal Sciences* 59 (2012), pp. 111–125 (cit. on p. 152).
- [124] Takuma Hori, Takafumi Kamino, Yuta Yoshimoto, Shu Takagi, and Ikuya Kinefuchi. “Mutual influence of molecular diffusion in gas and surface phases”. In: *Physical Review E* 97.1 (2018), p. 013101 (cit. on p. 153).
- [125] H. A. Hassan and David B. Hash. “A generalized hard-sphere model for Monte Carlo simulation”. In: *Physics of Fluids A: Fluid Dynamics* 5.3 (1993), pp. 738–744.
- [126] Didier F. G. Rault. “Aerodynamic characteristics of the Magellan spacecraft in the Venus upper atmosphere”. In: *Journal of Spacecraft and Rockets* 31.4 (1994), pp. 537–542.
- [127] J Drakes, D Swann, G Karabadzhak, and Yu Plastinin. “DSMC computations of the Progress-M spacecraft retrofiring exhaust plume”. In: *37th Aerospace Sciences Meeting and Exhibit*. 1999, p. 975.
- [128] Kyun Ho Lee and Seok Weon Choi. “Interaction effect analysis of thruster plume on LEO satellite surface using parallel DSMC method”. In: *Computers & Fluids* 80 (2013), pp. 333–341.
- [129] Georg Dettleff and Martin Grabe. *Basics of plume impingement analysis for small chemical and cold gas thrusters*. Report. Deutsches Zentrum Fur Luft-Und Raumfahrt (DLR) Göttingen, (Germany) Institut für Aerodynamik and Strömungstechnik, 2011.
- [130] I. D. Boyd, Y. Jafry, and J. V. Beukel. “Particle simulations of helium microthruster flows”. In: *Journal of Spacecraft and Rockets* 31.2 (1994), pp. 271–277.
- [131] Naoya Enoki, Yusuke Takahashi, Nobuyuki Oshima, Kazuhiko Yamada, and Kojiro Suzuki. “Aerodynamics of inflatable nano-satellite “EGG” in low earth orbit and reentry duration”. In: *AIP Conference Proceedings* 2132.1 (2019), p. 100002.

- [132] Ayyaswamy Venkatraman and Alina A. Alexeenko. “Direct simulation Monte Carlo modeling of metal vapor flows in application to thin film deposition”. In: *Vacuum* 86.11 (2012), pp. 1748–1758.
- [133] E. S. Oran, C. K. Oh, and B. Z. Cybyk. “DIRECT SIMULATION MONTE CARLO: Recent Advances and Applications”. In: *Annual Review of Fluid Mechanics* 30.1 (1998), pp. 403–441.
- [134] MS Ivanov, AV Kashkovsky, SF Gimelshein, et al. “SMILE system for 2D/3D DSMC computations”. In: *Proceedings of 25th International Symposium on Rarefied Gas Dynamics, St. Petersburg, Russia*, pp. 21–28.
- [135] Timothy D. Holman and Iain D. Boyd. “Effects of continuum breakdown on hypersonic aerothermodynamics for reacting flow”. In: *Physics of Fluids* 23.2 (2011), p. 027101.
- [136] A. G. Klothakis, I. K. Nikolos, T. P. Koehler, M. A. Gallis, and S. J. Plimpton. “Validation simulations of the DSMC code SPARTA”. In: *AIP Conference Proceedings* 1786.1 (2016), p. 050016.
- [137] Rakesh Kumar and Arun Kumar Chinnappan. “Development of a multi-species, parallel, 3D Direct Simulation Monte-Carlo solver for rarefied gas flows”. In: *Computers & Fluids* 159 (2017), pp. 204–216.
- [138] Stefan Dietrich and Iain D. Boyd. “Scalar and Parallel Optimized Implementation of the Direct Simulation Monte Carlo Method”. In: *Journal of Computational Physics* 126.2 (1996), pp. 328–342.
- [139] M. Ivanov, G. Markelov, S. Taylor, and J. Watts. “- Parallel DSMC strategies for 3D computations”. In: *Parallel Computational Fluid Dynamics 1996*. Ed. by P. Schiano, A. Ecer, J. Periaux, and N. Satofuka. Amsterdam: North-Holland, 1997, pp. 485–492.
- [140] J. S. Wu and K. C. Tseng. “Parallel DSMC method using dynamic domain decomposition”. In: *International Journal for Numerical Methods in Engineering* 63.1 (2005), pp. 37–76.
- [141] D. M. Nicol and J. H. Saltz. “Dynamic remapping of parallel computations with varying resource demands”. In: *IEEE Transactions on Computers* 37.9 (1988), pp. 1073–1087.
- [142] J. S. Wu, K. C. Tseng, and C. H. Kuo. “Application of local mesh refinement in the DSMC method”. In: *AIP Conference Proceedings* 585.1 (2001), pp. 417–425.
- [143] Jong-Shinn Wu, Kun-Chang Tseng, and Fu-Yuan Wu. “Parallel three-dimensional DSMC method using mesh refinement and variable time-step scheme”. In: *Computer Physics Communications* 162.3 (2004), pp. 166–187.
- [144] C. C. Su, K. C. Tseng, H. M. Cave, et al. “Implementation of a transient adaptive sub-cell module for the parallel-DSMC code using unstructured grids”. In: *Computers & Fluids* 39.7 (2010), pp. 1136–1145.

- [145] R. Arslanbekov, V. Kolobov, J. Burt, and E. Josyula. “Direct Simulation Monte Carlo with Octree Cartesian Mesh”. In: *43rd AIAA Thermophysics Conference*. Fluid Dynamics and Co-located Conferences. American Institute of Aeronautics and Astronautics, 2012.
- [146] Michael N. Macrossan. “Restricted Collision List method for faster Direct Simulation Monte-Carlo (DSMC) collisions”. In: *Journal of Computational Physics* 319 (2016), pp. 1–8.
- [147] M. A. Gallis, J. R. Torczynski, D. J. Rader, and G. A. Bird. “Convergence behavior of a new DSMC algorithm”. In: *Journal of Computational Physics* 228.12 (2009), pp. 4532–4548.
- [148] Sydney Chapman, Thomas George Cowling, and David Burnett. *The mathematical theory of non-uniform gases: an account of the kinetic theory of viscosity, thermal conduction and diffusion in gases*. Cambridge university press, 1990 (cit. on p. 183).

## Appendix

### A.1 Variable Soft Sphere (VSS)

The VSS model gives a realistic description of the ratio of the diffusion and viscosity cross-section consistent with the inverse power law. Scattering law was relevant to collisions but gas flows are more deeply affected by the collision cross-section. Thus, Koura and Matsumoto [90] formulated this model wherein the diameter was given by

$$d = d_{\text{ref}} \left( \frac{u_{r,\text{ref}}}{u_r} \right)^\eta, \quad (\text{A.1})$$

and the angle of deflection ([91], equation 2.36, page 41) is given by

$$\chi = 2 \cos \left( \frac{d_{\text{app}}}{d} \right)^{1/\alpha} \quad (\text{A.2})$$

The value of  $\alpha$  generally lies in between 1 and 2. In addition to correct viscosity coefficient, the VSS model also produces correct diffusion coefficients. VSS is preferred if molecular diffusion is important to the gas flow and has been used in this thesis.

### A.2 Sensitivity Analysis

In figure A.1, the time evolution of the reaction rate is seen as the activation energy is varied. As the activation energy is reduced from 83.68 kJ/mol to 40 kJ/mol, the reaction rate increases as it follows an Arrhenius type reaction mechanism. However, decreasing the activation energy further up to 10 kJ/mol again reduces the reaction rate as there is transport limitation.

At the base value of activation energy, i.e., 83.68 kJ/mol, there is hardly any change in the CO and O coverage as steady state is reached. Thus, there is no influence of  $\text{CO}_{\text{inlet}}$  at that activation energy, as seen in figure 4.24. Among all combinations of fitting parameters used, it was found that lowering the inhibition effect of  $\theta_{\text{CO}}$  on the available sites for  $\text{O}_2$  adsorption provided the most accuracy.

Figure A.3 shows all the combinations of input simulation parameters that were tried and the adsorption models used.

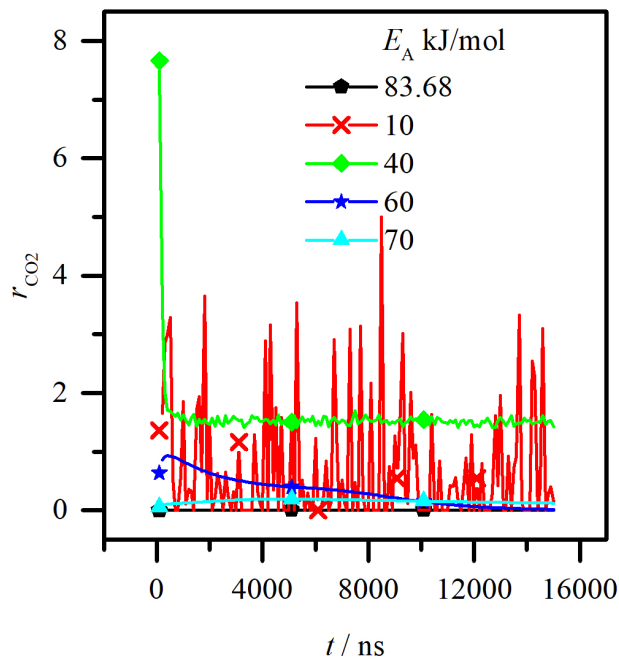


Fig. A.1.:  $r_{CO_2}$  versus time as a function of  $E_A$ . Parameters re given in table 4.15.

## A.3 Input parameters

### A.3.0.1. *dsmcProperties*

It contains the parcel size in case parcels are considered in the DSMC simulation. This text file also specifies the models used for collision, wall interaction, inflow and reaction. It also contains the molecule properties of all the participating molecules.

#### *nEquivalentParticles*

Each simulated molecule in DSMC represents n number of real molecules. The simulated molecule is termed 'parcel'. DSMC was originally developed for aerospace applications and the parcel concept was introduced to keep the tracking time low. This property is user-defined and very relevant to the correct description of the flow. Various works has been done to find the adequate number of molecules per cell to represent the flow accurately [80, 82].

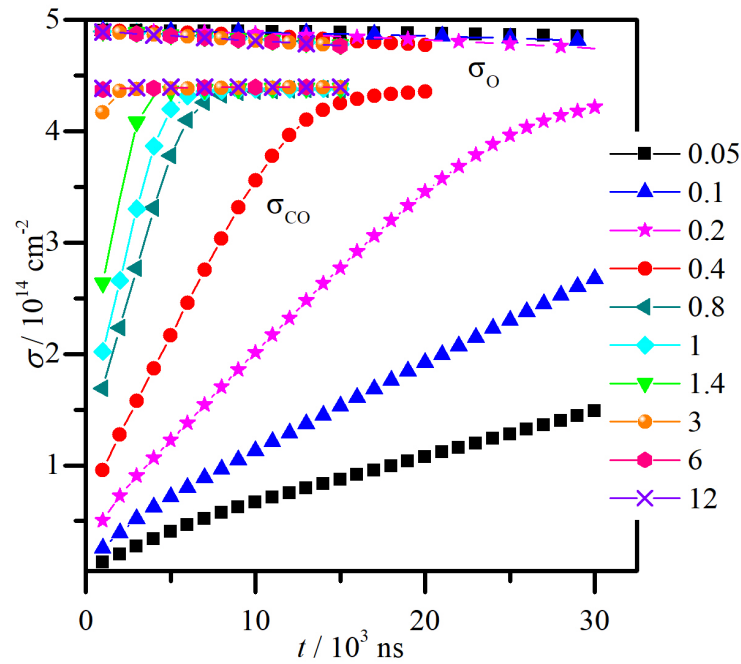


**Fig. A.2.:** Coverage,  $\sigma$  versus time as a function of  $CO_{inlet}$  at activation energy,  $E_A = 83.68$  kJ/mol. Parameters are given in table 4.16.

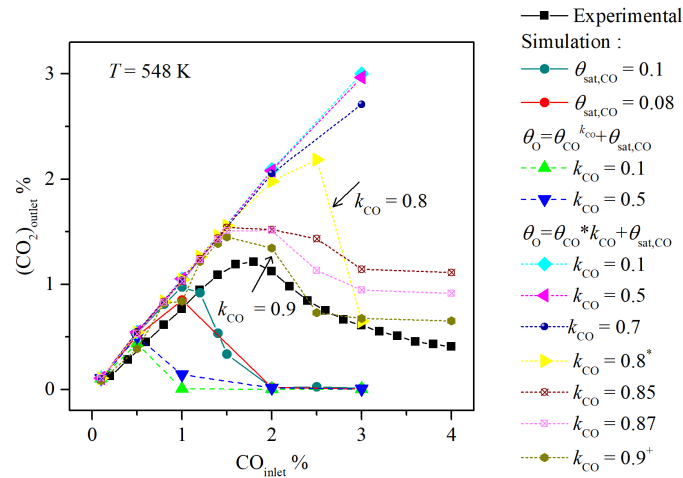


**Fig. A.3.:** Coverage models and fitting parameters used to validate the simulation  $CO_2$  output results with experimental values.

### Models

Models are specified that are to be used for wall and binary collision, inflow and reactions. These are the four sub-models used from the DSMC source files in OpenFOAM. The reaction submodule that is the base of the work in this thesis is

written by Pesch and Dreyer [77, 78]. The reaction routines have been modified to add the VP scheme. Under each model, the required constants are specified for each model. All the models are described separately elsewhere.

**Binary Collision model:** Variable Soft Sphere model

$\alpha$ : This is the VSS scattering parameter for simple gas or gas mixtures. The value is suggested by Chapman and Cowling [148] based on various diffusion experiments at very restricted temperatures. For gas pairs, they have calculated values for diffusion coefficient,  $D_{12}$  and the temperature exponent,  $\omega_{12}$ . The resulting  $\alpha$  values calculated by (Bird [67], equation A3) are according to

$$\alpha_{12} = \frac{8(5 - 2\omega_{12})n(D_{12})_{\text{ref}}\pi(d_{12})_{\text{ref}}^2}{3(2\pi kT_{\text{ref}}/m_r)^{0.5}} - 1 \quad (\text{A.3})$$

The reference temperature,  $T_{\text{ref}}$  is 723 K. The pair diameter,  $(d_{12})_{\text{ref}}$  is defined as the mean of the diameter of the two gases involved. The gases, in consideration in this thesis, are CO, O<sub>2</sub> and CO<sub>2</sub>. The  $\alpha$  values are given in the table below:

**Tab. A.1.:**  $\alpha_{12}$  and  $\omega_{12}$  values for the gas mixtures used in this work

| Pair                            | $\alpha_{12}$ | $\omega_{12}$ |
|---------------------------------|---------------|---------------|
| CO-CO <sub>2</sub>              | 1.61          | 0.71          |
| CO-O <sub>2</sub>               | 1.54          | 0.71          |
| CO <sub>2</sub> -O <sub>2</sub> | 1.72          | 0.75          |
| O <sub>2</sub> -Ar              | 1.33          | 0.75          |
| CO-Ar                           | 1.41          | -             |
| CO <sub>2</sub> -Ar             | 1.63          | 0.805         |

**Inflow model:** Free Stream model

All the simulated molecules are added to the simulation domain at the inlet with *nEquivalentParticles* and a velocity drawn from the Gaussian distribution. The only values to specify here are the number densities. The number densities are calculated according to ideal gas law assuming atmospheric pressure and an isothermal temperature.

$$\rho_{\text{inflow}} = y_i \times \frac{pN_A}{R_g T} \quad (\text{A.4})$$

where the mole fraction of the gas is  $y_i$ ,  $R_g$  is the universal gas constant and  $N_A$  is the Avogardo's constant.

**Reaction Model:** Langmuir Hinshelwood mechanism

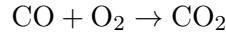
*Lattice Constant*

The lattice constant for Pd(111) crystal structure, The crystal has a fcc structure with edge length 3.88 Å. The lattice constant is then given by

$$\sqrt{2}/2a = 2.74\text{Å} \quad (\text{A.5})$$

Activation energy,  $E_{\text{LH}}$  and pre-exponential factor for the mechanism  $\nu_{\text{LH}}$

The activation energy and pre-exponential factor of the reaction



are 83.68 kJ/mol and  $2.5 \times 10^{-3}\text{cm}^2\text{s}^{-1}$  [35, 98] respectively.

The starting temperature,  $T_{\text{start}}$

The DSMC surface reaction algorithm can also be used to track the evolution of temperature in the catalyst. Generally, the assumption is that the surface environment is isothermal, which is not ideal. Next assumption is completely adiabatic conditions. In this assumption, the heat of the exothermic reaction is completely stored in the catalyst structure and the surface is allowed to heat up.

**Tab. A.2.:** Parameters used for the reaction model

| Parameter         | Value  |
|-------------------|--|
| Lattice constant  | 2.74 Å                                       |
| $E_{\text{LH}}$   | 83.68 kJ/mol                                 |
| $\nu_{\text{LH}}$ | $2.5 \times 10^{-3}\text{cm}^2\text{s}^{-1}$ |

### Adsorption Parameters

Adsorbatesperadsorbens

The gases CO and O<sub>2</sub> show complex co-adsorption behavior on Pd surface. While CO adsorbs molecularly on the surface, O<sub>2</sub> dissociatively adsorbs on the surface. If CO adsorbs first, beyond a coverage of 0.33, the adsorption of O<sub>2</sub> is completely inhibited. If O<sub>2</sub> adsorbs first, even if the coverage is saturation level, i.e.,  $\theta_{\text{sat},\text{O}} = 0.25$ , CO is able to adsorb on such surfaces. CO<sub>2</sub> is weakly bound to the catalyst surface and CO<sub>2</sub> surface lifetime is quite short above 100 K, thus, the coverage is taken to be zero at all times.

participateInAdsorption

This binary value explains if the gas molecule participates in adsorption. (0 = no, 1 = yes)

Initial Sticking Coefficient,  $S_0$

According to Kisliuk precursor model, the initial sticking coefficient is the probability of the molecule to stick to a clean surface [94, 95]. The value for  $S_0$  for CO is 1, independent of temperature. The values for O<sub>2</sub> are dependent on temperature and can be found in the Ref. [78].

Prefactor,  $K$

This adsorption parameter depends on the probability of molecule to be chemisorbed or desorbed on an empty or a filled site. The value for  $K$  for CO is 0.60 independent of temperature. The values for O<sub>2</sub> at different temperatures can be found in the Ref. [78].

Dissociativeads

This binary value represents if the molecule dissociates upon adsorption. For CO, CO<sub>2</sub> and Ar, it is 0 and for diatomic gas like O<sub>2</sub>, it is 1.

### ***Molecule Properties***

typeIdList

This is the list of all the molecules in the simulation. The order of this list is important to distinguish between different types of reactant and product molecules at various stages of the simulation. For instance, when 1 molecule of CO and 1 molecule of O react to form 1 molecule of CO<sub>2</sub>, proper care has to be taken to remove two type, one of CO and O each and to add one type of CO<sub>2</sub> to the gas phase.

The following section also notes all the well-known properties of the gas molecules like mass (kg), diameter (m), internal degrees of freedom, viscosity index ( $\omega$ ), VSS scattering parameter ( $\alpha$ ), viscosity coefficient ( $\mu, \text{Nsm}^{-2}$ ).

#### **A.3.0.2. adsorbedParcels**

This is a list of the number of adsorbed molecules at a patch any given time. At time  $t = 0$ , a value of 0 denotes a clean surface. This can be modified to suggest a fully saturated surface or any combination of coverage as per the user wish.

#### **A.3.0.3. boundaryT**

The isothermal temperature that is assumed inside the simulation domain. All the heat of reaction is thrown out instantaneously. This temperature is used in calculating sticking coefficient, reaction rate and desorption rate.

#### A.3.0.4. boundaryU

There are two types of boundary conditions (BC) imposed: fixed value (Dirichlet BC) and zero gradient (Neumann BC). Fixed value is generally applied to walls, in our case, the catalyst surface and reflecting wall. The value is set to zero. The molecules that contact such boundaries will reflect from the surface, if they are unable to adsorb. The latter condition, zero gradient simply translates the velocity of the molecule to the nearest volume cell. This boundary condition is imposed on inlets and outlets. The molecules approaching such boundaries simply pass through preserving their properties.

Other parameters are defined in the initial time period: Degree of freedom (iDoF), density (rhoM), volumetric flow rate (rhoN), change in internal energy (q), change in momentum (fD), internal energy (internalE), momentum and kinetic energy (linearKE).

#### A.3.0.5. dsmcInitialiseDict

Here, three important parameters are defined,  
Number Density

Calculated from Ideal gas law, this represents the number density of gas molecules present at  $t = 0$ .

$$\rho_{t=0} = \frac{p}{R_g T} \quad (\text{A.6})$$

Temperature

Initial temperature of the domain Velocity

The velocity of the system. Outside the domain's frame of reference, the system is at a constant zero velocity.

#### A.3.0.6. controlDict

The main parameters defined here are  
deltaT

The time step for the simulation. The time step is chosen based on the cell size and the most probable velocity such that a molecule does not move across cells in a single time step and has sufficient retention time in each cell.

$$\Delta t = x_C / v_{MPS} \quad (\text{A.7})$$

writeTime

The time intervals chosen for milestones within the simulation. All data can be collected at these data points and these data can be processed to show time evolution of different properties.

outputTime

This is the final time in real time for the simulation. Note: This is not equivalent to the computational time.

# List of Symbols

Roman symbols

| Symbol                | Description   | Unit                                     |
|-----------------------|---|--|
| $a$                   | Crystal Edge length, desorption constant (Chapter 2)          | m  |
| $A_{\text{coll}}$     | Total collision cross-section                                 | $\text{m}^2$                             |
| $A_f$                 | Area of the face  | $\text{m}^2$                             |
| $A_\mu$               | Viscosity cross-section                                       | $\text{m}^2$                             |
| $A_M$                 | Momentum cross-section  | $\text{m}^2$                             |
| $c(x,t)$              | Concentration at distance $x$ of the reactor and time $t$     | -  |
| $c_0$                 | Concentration at time $t = 0$                                 | -  |
| $CO_{\text{inlet}}$   | Inlet $CO$ concentration                                      | -  |
| $CO_{2\text{outlet}}$ | Outlet $CO_2$ concentration                                   | -  |
| $d$                   | Diameter of molecule; desorption order                        | m  |
| $d_{\text{app}}$      | Impact factor: distance of approach of colliding parcels      | m  |
| $D_a$                 | Diffusion coefficient   | $\text{m}^2\text{s}^{-1}$                |
| erfc                  | Complementary error function                                  | -  |
| $E_i$                 | Internal energy   | $\text{kgm}^2\text{s}^{-1}$              |
| $E_{\text{kinetic}}$  | Linear kinetic energy   | $\text{kgm}^2\text{s}^{-1}$              |
| $E_A$                 | Activation energy of reaction                                 | $\text{kJmol}^{-1}$                      |
| $E_{\text{des}}$      | Desorption activation energy                                  | $\text{kJmol}^{-1}$                      |
| $E_{\text{el}}$       | Electron-electron repulsion energy                            | $\text{kgm}^2\text{s}^{-1}$              |
| $E_{\text{ne}}$       | Nucleus-electron attraction energy                            | $\text{kgm}^2\text{s}^{-1}$              |
| $E_{\text{tot}}$      | Total energy in the configuration                             | $\text{kgm}^2\text{s}^{-1}$              |
| $E_{\text{xc}}$       | Pauli exclusion exchange correlation energy                   | $\text{kgm}^2\text{s}^{-1}$              |
| $f$                   | Probability density function                                  | -  |
| $F$                   | External force  | $\text{kgms}^{-2}$                       |
| $F_{ij}$              | Force between particle $i$ and $j$                            | $\text{kgms}^{-2}$                       |
| $F_{\text{coul}}$     | Coulombic force   | $\text{kgms}^{-2}$                       |
| $F_{\text{vdW}}$      | van der Waals force   | $\text{kgms}^{-2}$                       |
| $F_{\text{el}}$       | Electron-electron repulsion force                             | $\text{kgms}^{-2}$                       |
| $i$                   | variable, Number of adsorbed molecules from one parcel        | -  |
| $k$                   | Thermal conductivity  | W/mK                                     |
| $k_B$                 | Boltzmann constant  | $\text{kgm}^2\text{s}^{-1}\text{K}^{-1}$ |
| $k_{CO}$              | Fitting parameter   | -  |
| $k_i$                 | Rate constants used in KMC                                    | -  |
| $K$                   | Prefactor of adsorption                                       | -  |
| $Kn$                  | Knudsen number  | -  |
| $l$                   | Length of the reactor in $x$ direction, Characteristic length | m  |
| $m$                   | Mass of the gas species of parcel                             | kg                                       |
| $n_i$                 | Size of parcel $i$  | -  |

Roman symbols

| Symbol        | Description   | Unit                              |
|---------------|---|-----------------------------------|
| $n$           | Parcel size   | -                                 |
| $n_{max}$     | Maximum parcel size in VP scheme  | -                                 |
| $N$           | Avogadro's number   | -                                 |
| N.A.          | Not applicable  | -                                 |
| $N_{ads}$     | Number of adsorbed molecules  | -                                 |
| $N_C$         | Number of parcels in the cell   | -                                 |
| $N_{nn}$      | Number of nearest neighbours  | -                                 |
| $N_{sel}$     | Number of selected collision pairs in a cell                                      | -                                 |
| $N_{SS}$      | Number of samples for Pearson Correlation study                                   | -                                 |
| $N_{ads,p,f}$ | Number of adsorbed molecules of species p on face f                               | -                                 |
| $p$           | Momentum (Only in equation 4.2); pressure   | $\text{kgms}^{-1}, atm$           |
| $p_{coll}$    | Probability of collision  | -                                 |
| $p_{des}$     | Probability of desorption   | -                                 |
| $p_{reac}$    | Probability of reaction   | -                                 |
| $r$           | Position; radius of molecule  | <b>m</b>                          |
| $r_{CO_2}$    | Rate of $CO_2$ formation  | $\text{cm}^{-2}\text{s}^{-1}$     |
| $r_{des}$     | Rate of desorption  | $\text{cm}^{-2}\text{s}^{-1}$     |
| $r^2$         | Pearson correlation coefficient   | -                                 |
| $R$           | Random number   | -                                 |
| $R_g$         | Universal gas constant  | $\text{J.mol}^{-1}.\text{K}^{-1}$ |
| $R_G$         | Random number from Gaussian distribution  | -                                 |
| $S$           | Sticking coefficient  | -                                 |
| $t$           | time  | <b>s</b>                          |
| $t_d$         | Time step   | <b>s</b>                          |
| $T$           | Temperature   | <b>K</b>                          |
| $u$           | Initial velocity  | $\text{m.s}^{-1}$                 |
| $u_i$         | Initial velocity of parcel i  | $\text{m.s}^{-1}$                 |
| $u_{inlet}$   | Inlet velocity of parcels   | $\text{m.s}^{-1}$                 |
| $u_r$         | Relative velocity of colliding parcels  | -                                 |
| $v$           | Post-collision velocity   | $\text{m.s}^{-1}$                 |
| $V_C$         | Volume of the cell  | $\text{m}^3$                      |
| $V_{total}$   | Total volume of the simulation domain $\text{m}^3$                                | -                                 |
| $W$           | Lateral molecular interaction energy,<br>number of transitions in KMC (chapter 1) | <b>KJ/mol</b><br>-                |
| $x$           | Cartesian co-ordinate; value of input parameter                                   | -                                 |
| $\hat{x}$     | Unit vector (Chapter 2), Mean of all samples (Chapter 3)                          | -                                 |
| $y$           | Cartesian co-ordinate; value of quantity of interest                              | -                                 |
| $\hat{y}$     | Mean of all output variables (Chapter 3)  | -                                 |
| *             | vacant site   | -                                 |

## Greek symbols

| Symbol           | Description   | Unit               |
|------------------|---|--------------------|
| $\alpha$         | VSS scattering parameter  |                    |
| $\epsilon$       | Impact factor   |                    |
| $\eta$           | Exponent of inverse power law model   |                    |
| $\theta$         | coverage  | $\text{cm}^{-2}$   |
| $\lambda$        | Mean free path  | m                  |
| $\mu$            | Viscosity   | N.s                |
| $\nu_{des}$      | Pre-exponential factor for desorption kinetics                                    | $\text{s}^{-1}$    |
| $\nu_{LH}$       | Pre-exponential factor for reaction kinetics                                      | $\text{s}^{-1}$    |
| $\rho$           | Number density  | $\text{m}^{-3}$    |
| $\rho_m$         | Mass density  |                    |
| $\rho_{inflow}$  | Inflow number density   | $\text{kg.m}^{-3}$ |
| $\chi$           | Deflection angle of relative velocities   |                    |
| $\omega$         | Collision parameter   |                    |
| $\omega_{pair}$  | Lateral interaction energy between nearest neighbours                             | KJ/mol             |
| $\sigma$         | Cross-section (chapter 2),<br>Number of adsorbed molecules per area (Chapter 3,4) | $\text{m}^2$<br>-  |
| $\theta_{req}$   | Required number of vacant spots   | -                  |
| $\theta_{p,f_j}$ | Surface coverage of species p at face f   | $\text{m}^{-2}$    |
| $\theta_{sat}$   | Saturation coverage   | -                  |

## Subscripts

| Symbol | Description             |
|--------|-------------------------|
| ads    | adsorption              |
| coll   | collision               |
| des    | desorption              |
| LJ     | Lennard-Jones           |
| LH     | Langmuir Hinshelwood    |
| max    | maximum                 |
| normal | in the normal direction |
| r      | Relative                |
| ref    | reference               |
| req    | required                |
| x      | Cartesian x-coordinate  |
| y      | Cartesian y-coordinate  |
| z      | Cartesian z-coordinate  |
| 0      | at time $t = 0$         |

## Abbreviations

| Symbol   | Description   |
|----------|---|
| AES      | Auger Electron Spectroscopy   |
| BC       | Boundary condition  |
| CaRMEN   | Catalytic reaction mechanism network                                |
| CFD      | Computational fluid dynamics  |
| DEM      | Discrete element method   |
| DFT      | Density functional theory   |
| DSMC     | Direct simulation monte carlo                                       |
| EELS     | Electron energy loss spectroscopy                                   |
| EP       | Equivalent Parcel   |
| ER       | Eley Rideal   |
| FM       | Free molecules  |
| FSP      | Flame spray pyrolysis   |
| IP       | Input parameter   |
| KMC      | Kinetic monte carlo   |
| LB       | Load balancing  |
| LEED     | Low energy electron diffraction                                     |
| LH       | Langmuir Hinshelwood  |
| LSPR     | Localised Surface Plasmonic Resonance                               |
| MC       | Monte Carlo   |
| MD       | Molecular dynamics  |
| MFS      | Majorant frequency scheme   |
| MoCKa    | Monte Carlo Karlsruhe   |
| MvK      | Mars and van Krevelen   |
| NFS      | Non-equilibrium flow solver   |
| NP       | Nanoparticle  |
| OKMC     | Object kinetic monte carlo  |
| OpenFOAM | Open-source field operation and manipulation                        |
| PLIF     | Planar laser-induced fluorescence                                   |
| PM-IRAS  | Polarisation modulation infrared reflection absorption spectroscopy |
| PPC      | Parcel per cell   |
| QM/MM    | Quantum Mechanics/Molecular Mechanics                               |
| QMS      | Quadrupole mass spectrophotometer                                   |
| QoI      | Quantity of interest  |
| SAR      | Stop-at-rise  |
| SMILE    | Statistical modeling in low-density environment                     |
| SPARTA   | Stochastic parallel rarefied-gas time-accurate analyzer             |
| TCE      | Total collision energy  |
| TST      | Transition State Theory   |
| UHV      | Ultra high vacuum   |
| VP       | Variable Parcel   |
| VSS      | Variable soft sphere  |
| XPS      | X-ray photoelectron spectroscopy                                    |

# List of Figures

|     |   |    |
|-----|---|----|
| 1.1 | CO oxidation is one of the many reactions that is the focus of understanding heterogeneous catalysis. It has been and still is relevant to modern society and industry. CO sources from human beings, nature and man-made objects and finds uses in industry in varying capacity. . . . .   | 4  |
| 1.2 | Different reaction mechanisms proposed for CO oxidation on metal oxides. Red and Yellow: Reactant gas molecules, Green: Product, Blue: Catalyst atoms. . . . .  | 7  |
| 1.3 | Hierarchy of available multiscale models. . . . .   | 12 |
| 1.4 | Steps involved in available molecular simulation models. (a) Molecular MC depends on finding molecular configurations with lowest internal energy through random displacements of one molecule at a time. For this, the difference between initial and final state energy is compared to a random number. Several states are then sampled to find average molecular properties. (b) In MD, atoms/molecules are moved according to the cumulative force experienced by them (coulombic force $F_{\text{coul}}$ , van der Waals force $F_{\text{vdW}}$ and electron-electron repulsion $F_{\text{el}}$ ). With an exact description of forces, the trajectory of the system is established via Newton's laws of motion. (c) The main goal of DFT is to find the ground state for atoms/molecules/systems. Since a multi body problem still remain an unsolvable problem, DFT approximates that the ground state can be established by knowing the energy density functional constructed from kinetic energy $E_{\text{kinetic}}$ (green), nucleus-electron attraction $E_{\text{ne}}$ (blue), electron-electron repulsion $E_{\text{el}}$ (red) and Pauli-Exclusion Exchange Correlation energy $E_{\text{xc}}$ . (d) The first step of KMC involves making a list of all transitions( $W$ ) and its corresponding rate constants. A random transition step is chosen and the time step is forwarded by a random time step. $R$ is a random number between 0 and 1. . . . . | 15 |
| 1.5 | Basic schematic of the Direct Simulation Monte Carlo (DSMC) method.   | 27 |

|     |   |    |
|-----|---|----|
| 2.1 | Equations of fluid mechanics. The Euler equation and Navier-Stokes equation are derived from the three conservation laws where viscosity is denoted by $\mu$ and thermal conductivity by $k$ . Mean free path is calculated by averaging the maximum distance travelled between collisions. . . . .   | 37 |
| 2.2 | Binary collision in the center of mass frame of reference. The closest distance of approach between two molecules is $d_{app}$ , the angle of deflection between the two colliding molecules is $\chi$ and $u_r$ is the relative velocity of the colliding partners. The angle between the colliding plane and the reference plane is $\epsilon$ . The three collision models are derived based on inverse power law. The diameters of the colliding spheres are given by $d_1$ and $d_2$ , subscript <sub>ref</sub> refers to reference values, $\nu$ is a simple inverse law exponent, $\alpha$ is the temperature exponent of viscosity coefficient. The value of $\alpha$ generally lies in between 1 and 2. The three collision cross-sections are: $A_T$ , total collision cross-section area, $A_\mu$ , viscosity cross-section and $A_M$ , momentum cross-section. [67, 90, 91] | 40 |
| 2.3 | Collision algorithm followed in a typical DSMC simulation. . . . .  | 42 |
| 2.4 | Schematic of the DSMC algorithm used to simulate surface reaction [78].   | 46 |
| 2.5 | Adsorption algorithm developed by Pesch et al. [78]. . . . .  | 50 |
| 2.6 | Parameters initialised in the DSMC algorithm. The dotted boxes refer to folders and the solid boxes refer to the files within the case file. Further details about each individual parameters are given in the appendix. . .  | 54 |
| 3.1 | (a) Simulation domain showing the computer-generated porous structure [100]. There is one inlet, one outlet and periodic boundary conditions on the other four sides. Further details on the simulation of the mesoporous layers are given in ref. [77, 100]. (b) A 2D-view of the computational cell consisting of the gas phase and the solid catalyst surface. The catalyst surface is made up of several patches. (c) 2D-view of a patch. The patch is further divided into faces. All steps in the molecule-surface interaction are performed on the faces. A dynamic list of molecules adsorbed, desorbed and formed of each gas species is maintained on each face of each patch of the catalyst surface. . . . .  | 58 |
| 3.2 | Workflow in a DSMC code. Collision and surface steps are decoupled from one another. Separate lists of data are maintained for the molecules in the gas phase and on the surface. . . . .   | 59 |

|      |  |    |
|------|--|----|
| 3.3  | The working of variable parcel method. A simulated molecule is representing a group of molecules. This variable can be fixed by the user during initialisation. The larger the parcel size, lower the number of molecules that are to be tracked which reduces the computational time. Here, the gaseous phase is represented by parcels of variable sizes (parcel size mentioned inside the parcels). For a total of 180 molecules (for example) per computational cell, the distribution of parcels can be seen. The parcel size is limited by the maximum size specified by user. In general, with a larger $n_{\max}$ , the number of parcels will be lower. . . | 60 |
| 3.4  | Collision scheme in VP method. The modifications from Pesch et al.'s code are shown in light blue. . . . .   | 66 |
| 3.5  | Modified adsorption algorithm accommodating parcels. Each parcel can represent varying number of real molecules. The modification is showed in light blue. . . . .   | 67 |
| 3.6  | Available pathways for an adsorbed molecule . . . . .  | 68 |
| 3.7  | Desorption and Reaction mechanism following adsorption of molecules. When a molecule desorbs from the surface, under the condition that it has sufficient energy to overcome desorption barrier (in case of CO and O <sub>2</sub> ) or a product molecule is formed (in this case, CO <sub>2</sub> desorbs instantaneously from the surface). Blue: CO; Yellow: O <sub>2</sub> ; Green: CO <sub>2</sub> . $R$ is a newly generated number uniformly distributed between 0 and 1. . . . .   | 68 |
| 3.8  | Parcel re-introduction process of gas molecules to parcels in gaseous phase under VP method. All the molecules are packed as efficiently as possible into parcels, regardless of the number of available molecules. . . . .  | 70 |
| 3.9  | Schematic of the chip manufactured by Physics group at Chalmers [105]. (a) The uniformly heated chip which is a support of the 40 parallel nano-channels. The inlet gas flow is controlled by a (b) flow controller and the outgoing gas is collected and analysed by a (c) spectrophotometer. The (d) nano-channel comprises of 18 Pd cylinders spaced 5 $\mu\text{m}$ apart. (e) Each cylinder is purely Pd of 100 nm diameter and 40 nm height and the complete surface is active. . . . .  | 73 |
| 3.10 | Computational mesh of the setup. Each cell has 8nm cubic dimensions. (a) This shows the yz cross-section of the domain. (b) The cylindrical Pd particle. . . . .   | 74 |

|      |  |     |
|------|--|-----|
| 3.11 | Hypothetical parameter space showing the dependence of the desired output, CO <sub>2</sub> concentration on an input variable. Graphs like this help in determining the degree of dependence for different variables. This particular example shows a positive linear dependence of the output on this particular input variable. However, there are many outliers also. Thus, while the Pearson coefficient method is good for linear dependencies, it may miss out on non-linear ones. . . . .   | 78  |
| 4.1  | Diffusion in an empty cuboid. Gas composed of 10 % CO and 90 % O <sub>2</sub> is flowed through the inlet of the cuboid at $T = 323$ K, $p = 1$ atm. Computational time required to simulate 300 ns of diffusion in the cuboid is plotted here. The solid line represents the simulation volume divided into cells of different sizes at $n = 1$ (upper $x$ -axis). The dashed line represents the computational time for various parcel sizes when the volume is divided into 8 nm cell sizes (lower $x$ -axis). Parameters are given in table 4.1. . . . . | 88  |
| 4.2  | Simulation of diffusion using DSMC-VP method in a semi-infinite box. The analytical result is shown by the solid line and the simulated results are plotted as data points. Parameters are given in table 4.2. . . . .   | 90  |
| 4.3  | Surface coverage as a result of different CO:O <sub>2</sub> ratio starting from zero coverage. Parameters are given in table 4.3. . . . .  | 93  |
| 4.4  | Surface coverage as a result of different CO:O <sub>2</sub> ratio starting from full coverage. Parameters are given in table 4.3. . . . .  | 94  |
| 4.5  | (a) Local CO <sub>2</sub> concentration and (b) Cumulative CO <sub>2</sub> versus time. The parcel size is kept fixed at 1. Parameters are given in table 4.4. . . . .   | 96  |
| 4.6  | Local surface coverage (blue, solid) for $T = 723$ K and corresponding local reaction rate $r_{\text{CO}_2}$ (orange, dashed) as a function of $x$ at steady state $t = 8000$ ns using parcel size of 1. Parameters are given in table 4.5. . . . .  | 98  |
| 4.7  | Arrhenius plot: Dependence of reaction rate on temperature at $n = 1$ . Parameters are given in table 4.6 . . . . .  | 100 |
| 4.8  | Local CO <sub>2</sub> concentration at $t =$ (a) 2000 ns, (b) 4000 ns, (c) 6000 ns and (d) 8000 ns. CO and O <sub>2</sub> react on Pd porous structure to form CO <sub>2</sub> following Langmuir Hinshelwood mechanism. . . . .   | 101 |
| 4.9  | Cumulative CO <sub>2</sub> versus time simulating diffusion, adsorption and reaction in a cuboid with a mesoporous structure. Parameters are given in table 4.8. . . . .   | 104 |
| 4.10 | (a) Local surface coverage for $T = 723$ K at steady state $t = 8000$ ns for different $n_{\text{max}}$ . (b) Corresponding local reaction rate $r_{\text{CO}_2}$ as a function of $x$ using different parcel sizes. . . . .   | 105 |

|      |  |     |
|------|--|-----|
| 4.11 | Arrhenius plot corresponding to CO oxidation on Pd representing different maximum parcel sizes in the VP scheme. . . . .   | 107 |
| 4.12 | Computational time required reach steady state for CO oxidation on Pd using VP scheme. The coloured points represent simulations where agglomeration was neglected. The hollow black squares represent simulations where particle merging is achieved during collisions. . . .   | 108 |
| 4.13 | Local surface coverage (a) CO and (b) O for $T = 723$ K at different $t$ for $n_{\max} = 100$ . Parameters are given in table 4.11. . . . .  | 111 |
| 4.14 | Local surface coverage (a) CO and (b) O for $T = 523$ K at different $t$ for $n_{\max} = 100$ . Parameters are given in table 4.11. . . . .  | 112 |
| 4.15 | Local CO coverage near the inlet of the structure. The simulation is pre-covered with maximum CO coverage. Hence, the reaction rate is high initially and the coverage drops quickly. With time, the CO reacts off and the CO coverage drops. However, the CO coverage increases again with time due to the influx of CO molecules near the inlet and it gets covered with CO. Parameters are given in table 4.11. . . . . | 113 |
| 4.16 | Local reaction rate with increasing time for $T =$ (a) 523 K, (b) 623 K, (c) 723 K and (d) 823 K computed at $n_{\max} = 100$ . Parameters are stated in table 4.12. . . . .   | 115 |
| 4.17 | (a) CO (line + symbol) and O coverage (symbol) and (b) average reaction rate versus time. Input Parameters: $\theta_{\text{sat,CO}}, \theta_{\text{sat,O}}$ . Parameters are given in table 4.14. . . . .  | 123 |
| 4.18 | Sensitivity plot for % change in QoI vs IP: (a) $\sigma_{\text{CO}}$ vs $\theta_{\text{sat,CO}}$ (solid, square), $\theta_{\text{sat,O}}$ (dashed, square), $\sigma_{\text{O}}$ vs $\theta_{\text{sat,CO}}$ (solid, circle), $\theta_{\text{sat,O}}$ (dashed, circle), (b) $r_{\text{CO}_2}$ vs $\theta_{\text{sat,CO}}$ (solid), $\theta_{\text{sat,O}}$ (dashed). Parameters are given in table 4.14. . . . .            | 124 |
| 4.19 | (a) QoI: $\text{CO}_{2\text{outlet}}$ at time $t = 15000$ ns; IP: $\theta_{\text{sat,CO}}, \theta_{\text{sat,O}}$ (b) % change in $\text{CO}_{2\text{outlet}}$ vs $\theta_{\text{sat,CO}}, \theta_{\text{sat,O}}$ . Parameters are given in table 4.14. . . . .  | 125 |
| 4.20 | (a) QoI: CO (black), $\sigma_{\text{CO}}$ and O (red) coverage, $\sigma_{\text{O}}$ ; IP: $E_{\text{A}}$ (b) % change in steady state coverage of CO and O vs % decrease in $E_{\text{A}}$ . Parameters re given in table 4.15. . . . .  | 127 |
| 4.21 | (a) QoI: $r_{\text{CO}_2}$ at time $t = 15000$ ns; IP: $E_{\text{A}}$ (b) % change in $r_{\text{CO}_2}$ vs % decrease in $E_{\text{A}}$ . Parameters re given in table 4.15. . . . .   | 128 |
| 4.22 | (a) QoI: $\text{CO}_{2\text{outlet}}$ at time $t = 15000$ ns; IP: $E_{\text{A}}$ (b) Sensitivity plot. Parameters re given in table 4.15. . . . .  | 129 |
| 4.23 | QoI: (a) CO and O coverage $\sigma_{\text{CO}}, \sigma_{\text{O}}$ and (b) average reaction rate versus time. IP: $\text{CO}_{\text{inlet}}$ . Parameters are given in table 4.16. . . . .   | 131 |
| 4.24 | QoI: (a) Predicted (black) $\text{CO}_{2\text{outlet}}$ at two different activation energy. IP: $\text{CO}_{\text{inlet}}$ at $T = 498$ K. Parameters are given in table 4.16. . . . .   | 132 |

|      |  |     |
|------|--|-----|
| 4.25 | (a) $\text{CO}_{2\text{outlet}}$ concentration as sticking coefficients, $S_{\text{CO}}$ and $S_{\text{O}}$ and exponent of the coverage term to calculate $S$ , $\text{expCO}$ and $\text{expO}$ are modified. (b) % change in $\text{CO}_{2\text{outlet}}$ versus % change in the adsorption parameters. Parameters are given in table 4.18. . . . .   | 137 |
| 4.26 | $\text{CO}_{2\text{outlet}}$ as a function of $k_{\text{CO}}$ at $T = 498$ K. It is combined with a lower $\theta_{\text{sat,CO}}$ and a lower activation energy. This also shows that a change of 30 % increases the $\text{CO}_{2\text{outlet}}$ by three orders of magnitude. Parameters are given in table 4.19. . . . .   | 139 |
| 4.27 | $\text{CO}_{2\text{outlet}}$ predicted (dashed) and experimental (solid) concentration as $\text{CO}_{\text{inlet}}$ concentration is increased. Three temperatures are included. The $k_{\text{CO}}$ values are the best fits obtained for that temperature. . . . .  | 141 |
| 4.28 | (a) Local average reaction rate and (b) local average CO coverage across the channel at $T = 548$ K as $\text{CO}_{\text{inlet}}$ is increased from 0.1 to 3.0 %. The particle with the maximum reaction rate at any particular $\text{CO}_{\text{inlet}}$ is encircled in red. The maximum reaction rate observed on an individual Pd particle shifts towards the centre of the channel ( $\text{CO}_{\text{inlet}} = 1.0$ %) as the $\text{CO}_2$ peak is crossed and moves towards the outlet as the concentration is further increased. Below $\text{CO}_{\text{inlet}} = 1.0$ %, the Pd particles near the outlet have zero reactivity owing to a lack of adsorbed reactants. Higher concentration white particles indicates poisoning of the Pd surface by CO leading to very low reaction rate. $\theta_{\text{CO}} = 0.1, k_{\text{CO}} = 1.0$ . . . . . | 145 |
| 4.29 | (a) Local average reaction rate and (b) local average CO coverage for $\text{CO}_{\text{inlet}} = 1.0$ % at different temperatures. The Pd particles at 498 K are CO poisoned and the reaction rate is very low. For 498 K, the entire channel is poisoned whereas the nanochannel is active at 523 K and 548 K due to reduced CO coverage because of higher reaction rate. . . . .  | 146 |
| 4.30 | Local CO coverage on a single Pd particle at different time steps. The background shows the mean reaction rate across the entire particle. Here, the 6 <sup>th</sup> particle from the inlet is shown at $T = 523$ K from $t = 1000$ to 15000 ns. As the CO coverage increases with time, the reaction rate increases and then reduces as CO adsorption dominates. $\theta_{\text{CO}} = 0.1, k_{\text{CO}} = 0.95$ . . . . .  | 147 |
| A.1  | $r_{\text{CO}_2}$ versus time as a function of $E_A$ . Parameters re given in table 4.15.  | 181 |
| A.2  | Coverage, $\sigma$ versus time as a function of $\text{CO}_{\text{inlet}}$ at activation energy, $E_A = 83.68$ kJ/mol. Parameters are given in table 4.16. . . . .   | 182 |
| A.3  | Coverage models and fitting parameters used to validate the simulation $\text{CO}_2$ output results with experimental values. . . . .  | 182 |

# List of Tables

|      |   |     |
|------|---|-----|
| 1.1  | Activation energies calculated from DFT and KMC calculations of CO oxidation on different Pd structures. . . . .                                | 19  |
| 2.1  | Desorption parameters for CO and O <sub>2</sub> taken from Ref. [15] and [32]. .  | 53  |
| 3.1  | Differences between the DSMC surface algorithm used by Pesch et al. [78] and the Variable Parcel method proposed in this thesis. . . . .        | 79  |
| 4.1  | Simulation parameters for study of diffusion in an empty cuboid only using fixed size parcels, given in figure 4.1. . . . .                     | 87  |
| 4.2  | Simulation parameters for study of diffusion only using variably sized parcels shown in figure 4.2. . . . .                                     | 89  |
| 4.3  | Simulation parameters for study of CO poisoning using VP scheme, used in figure 4.3 and 4.4. . . . .  | 92  |
| 4.4  | Simulation parameters for study of local CO <sub>2</sub> and cumulative CO <sub>2</sub> using VP scheme, shown in figure 4.5. . . . .           | 95  |
| 4.5  | Simulation parameters for study of steady state local surface coverage and reaction rate of CO and O at 723 K. . . . .                          | 97  |
| 4.6  | Simulation parameters for study of Arrhenius plots using VP scheme for figure 4.7. . . . .  | 99  |
| 4.7  | Simulation parameters for study of local CO <sub>2</sub> and cumulative CO <sub>2</sub> using VP scheme. . . . .                                | 102 |
| 4.8  | Simulation parameters for study of cumulative CO <sub>2</sub> using VP scheme, given in figure 4.9. . . . .                                     | 103 |
| 4.9  | Simulation parameters for study of steady state local surface coverage and reaction rate of CO and O at 723 K, used in figure 4.10. . . . .     | 105 |
| 4.10 | Simulation parameters for study of Arrhenius plots using VP scheme, used in figure 4.11. . . . .  | 106 |
| 4.11 | Simulation parameters for study of local surface coverage of CO and O using VP scheme. Used for figure 4.13, 4.14 and 4.15. . . . .             | 110 |
| 4.12 | Simulation parameters for study of local surface coverage and reaction rate with increasing time at different temperatures used in figure 4.16. | 114 |

|      |  |     |
|------|--|-----|
| 4.13 | The input parameters ( $\downarrow$ ) and their expected influence on the quantities of interest ( $\rightarrow$ ) when increased in value. When the input parameter is increased, if the output parameter also increases, it is represented by a '+' and vice-versa is represented by '-'. A '+-' refers to an initial increase followed by a decrease in the output as the input parameter is increased. | 120 |
| 4.14 | Simulation parameters for sensitivity study of $\text{CO}_{2\text{outlet}}$ , $r_{\text{CO}_2}$ , $\sigma_{\text{CO}}$ and $\sigma_{\text{O}}$ for each of the input variables: $\theta_{\text{sat,CO}}$ , $\theta_{\text{sat,O}}$ . The parameters are used in figures 4.17, 4.18 and 4.19.   | 122 |
| 4.15 | Simulation parameters for sensitivity study of $\text{CO}_{2\text{outlet}}$ , $r_{\text{CO}_2}$ , $\sigma_{\text{CO}}$ and $\sigma_{\text{O}}$ for the input variable: $E_A$ shown in figures 4.20, 4.21 and 4.22.   | 126 |
| 4.16 | Simulation parameters for sensitivity study of $\text{CO}_{2\text{outlet}}$ , $r_{\text{CO}_2}$ , $\sigma_{\text{CO}}$ and $\sigma_{\text{O}}$ for the input variable: $\text{CO}_{\text{inlet}}$ shown in figures 4.23 and 4.24.  | 130 |
| 4.17 | Summary of the Pearson correlation coefficient for different QoI at varying IP.  | 134 |
| 4.18 | Simulation parameters for sensitivity study of adsorption parameters $S_{\text{CO}}$ , $S_{\text{O}}$ , $\text{expCO}$ and $\text{expO}$ used in figure 4.25.  | 136 |
| 4.19 | Simulation parameters for sensitivity study of a new adsorption parameter $k_{\text{CO}}$ shown in figure 4.26.  | 138 |
| A.1  | $\alpha_{12}$ and $\omega_{12}$ values for the gas mixtures used in this work  | 184 |
| A.2  | Parameters used for the reaction model   | 186 |

## Colophon

This thesis was typeset with  $\text{\LaTeX}2_{\epsilon}$ . It uses the *Clean Thesis* style developed by Ricardo Langner. The design of the *Clean Thesis* style is inspired by user guide documents from Apple Inc.

Download the *Clean Thesis* style at <http://cleanthesis.der-ric.de/>.



# Declaration

I, hereby, declare that I have completed the work presented in this solely and all references and collaborators have been cited dutifully.

---

Sangita Swapnasrita

